Summer 8-15-2016

Development of a Long-Period Torsion Balance for Tests of Einstein's Equivalence Principle and a Search for Normal Mode Torsional Oscillations of the Earth

Michael David Abercrombie
Washington University in St. Louis

WASHINGTON UNIVERSITY IN ST. LOUIS

Department of Physics

Dissertation Examination Committee:
Ramanath Cowsik, Chair
Francesc Ferrer
Martin H. Israel
Sándor J. Kovács
Henric Krawczynski
Douglas A. Wiens

Development of a Long-Period Torsion Balance for Tests of Einstein's Equivalence Principle and a Search for Normal Mode Torsional Oscillations of the Earth

by

Michael D. Abercrombie

A dissertation presented to the
Graduate School of Arts and Sciences
of Washington University in
partial fulfillment of the
requirements for the degree
of Doctor of Philosophy

August 2016

Saint Louis, Missouri

Contents

List of Figures

List of Tables

Acknowledgements

First and foremost I would like to thank Professor Ramanath Cowsik for giving me the opportunity to work on such exciting research as the experiment which is detailed in this thesis. I consider myself quite fortunate to have worked with an advisor with such a wealth of knowledge and insight, not only in the realm of physics, but in life in general. I have truly learned a great deal from Professor Cowsik. In addition to Professor Cowsik, I would like to thank the other members of my committee for their feedback on this thesis as well.

Another person who helped me immensely throughout this process is Dr. Kasey Wagoner. As someone who laid much of the foundation for the instrument I worked on, he was an invaluable resource whenever problems would arise. On top of always being eager to help with the experiment, Kasey has always been willing to offer advice which has had a significant impact on my professional development as a scientist.

In the GEE Lab, Tsitsi and Adam have been a pleasure to work alongside. Often offering help with my research, either through physically helping with the experiment, or through discussion of some issue, I have learned a great deal from each of them and have enjoyed their company over the better part of the past five years.

I would not have gotten to this point without the support and friendship from numerous individuals, both since I've lived in St. Louis and elsewhere. I have met a number of exception people, for which I am much better off. While there are too many of you to name here, I hope you all know who you are, and know that you are appreciated.

One particular individual who was a very influential figure to me, was my high school biology teacher and baseball coach, Coach Grove. Of the many lessons that he worked so hard to impress upon his students and players, I feel that one rings particularly true in terms of my graduate research: "If it were easy, everyone would do it." Laboratory tests of gravity are a particularly challenging set of experiments as indicated by the incremental progress in the field with experiments spanning over 300 years as well as the length of time required for each individual experiment. This does not make the research not worth doing, on the contrary, I believe it is absolutely worth doing!

My brothers Luke and Danny, and my sister Sarah, have always been encouraging and a source of motivation for me. I thank you all for being such wonderful siblings and such impressive people.

I would also like to thank my wife, Lacey, and her family, who have always provided me a "family away from home." Lacey has been so wonderful and incredibly patient throughout my graduate studies. I have always found her excitement about learning new things inspirational; whether it is some detail of my work, or some other question about physics. I eagerly look forward to continuing our adventures, and exploring new questions about the universe with you. I love you so much, Lacey, $\lim_{t\to\infty}$.

And finally, I want to thank my parents, who have always put me and my brothers and sister before everything else. You have given the four of us such tremendous opportunities to be successful and to accomplish great things (I mean, we did all become scientists!). Mom and Dad, thank you for everything! I love you.

Michael D. Abercrombie

Washington University in St. Louis

August 2016

Dedication

To my parents, who instilled in me a joy for learning at a young age, and taught by example that the easy way of doing something is usually not the right way.

ABSTRACT OF THE DISSERTATION

Development of a Long-Period Torsion Balance for Tests of Einstein's Equivalence Principle and a Search for Normal Mode Torsional Oscillations of the Earth

by

Michael D. Abercrombie

Doctor of Philosophy in Physics

Washington University in St. Louis, 2016

Professor Ramanath Cowsik, Chairperson

This thesis describes the development of a torsion balance experiment designed to test Einstein's equivalence principle with unprecedented sensitivity, while also taking a novel approach to directly observe the normal mode torsional oscillations of the Earth. Accordingly, a model of the signal expected from a potential equivalence principle violation has been developed, as well as a multi-slit auto-collimating optical lever which possesses a resolution on the order of a nanoradian and a range of observation of 10 milliradians and is used to monitor the torsion balance. A torsion balance with a natural torsional frequency of $\sim 10^{-4}$ Hz, significantly below the frequency of the longest of the Earth's normal modes, was designed, built, and operated in a remote laboratory at Washington University's Tyson Research Center. More than 1800 hours of data was collected and used to evaluate the performance of this prototype instrument and characterize the conditions in the Tyson laboratory.

Chapter 1

Synopsis

The recent detection of gravitational waves with a waveform propagating at the speed of light has confirmed another prediction of Einstein's Theory of General Relativity. Along with other successes of the theory, this measurement gives impetus to testing the foundations of General Relativity, amongst which the equivalence principle occupies a fundamental position. This thesis describes efforts to design, construct, and characterize the prototype of a torsion balance experiment designed to search for violations of Einstein's equivalence principle with unprecedented sensitivity while also taking a completely novel approach to study the lowest frequency torsion normal modes of the Earth. To this end, a complete model of the signal expected for a hypothesized violation of the equivalence principle has been developed for an experiment located in Saint Louis, Missouri, using solar position data and the characteristics of the balance described in this dissertation. A multi-slit auto-collimating optical lever with a large dynamic range and high sensitivity has been developed to monitor

the angular displacement of the torsion balance. And finally, a balance with a natural torsional frequency of $\sim 10^{-4}$ Hz, significantly below the longest of the Earth's normal modes, has been designed, built, and characterized, with many months of preliminary data collected from the instrument. As a result of the knowledge gained from this work, the next steps for an experiment operating for approximately a year are laid out in detail so that future progress may be made in a straightforward manner. The layout for the body of this thesis is now described.

In Chapter 2 the equivalence principle is introduced by describing the historical context in which it was developed before arriving at a formal definition as followed today. The motivations for testing this fundamental aspect of modern physics are provided as well, ranging from theoretical work to astronomical observations, before closing with an overview of past and current experimental tests of the equivalence principle.

In Chapter 3 the motivations for the particular innovations targeted by this effort are presented, as well as the steps taken to accomplish these goals, and the end results. This chapter begins with the model of the signal expected for a violation of the equivalence principle. Here the general concept of the experiment is described as well. Next, the development of an instrument with high dynamic range, capable of monitoring the balance with a precision of $\sim 10^{-9}$ rad is described, and the performance of the instrument while operating in the experiment's setting is presented. Finally the design and operation of a torsion balance with a period nearly 10 times longer than those performing similar experiments elsewhere is described. An overview of the torsion balance as an instrument of experimental gravitation is

given, followed by a discussion of the sensitivity of the balance to the signals that would arise from an equivalence principle violation and its insensitivity to local gravitational gradients, a potentially harmful systematic effect.

Chapter 4 describes the major components of the torsion balance. First, the balance itself is described, as well as its fabrication. Next, the suspension system and the torsion fiber from with the balance hangs from are discussed. Another key aspect of this work was the development and implementation of a mechanical damping scheme which allows for the remote damping of the torsional oscillations of the balance to only a few μrad within a short period of time. To reduce energy lost to collisions with air molecules and noise in the angular orientation of the balance, the balance is enclosed in a vacuum chamber maintained at a pressure below 10^{-7} Torr. This system is described, as are efforts to passively shield the experiment from thermal variations and ambient magnetic fields; both potential sources of a false signal. Finally, the remote underground laboratory which offers favorable conditions for a sensitive torsion balance experiment is described.

In Chapter 5 data are presented which have been obtained from many months of operating the experiment at the Tyson Research Center bunker. At all times, the balance position, vacuum chamber pressure, and air temperature at various locations surrounding the experiment were recorded. Based on the relevant characteristics of the balance as measured at Tyson the sensitivity of the current balance is evaluated. Analysis of this preliminary data is given in both the time and frequency domains in terms of bounds on a possible violation of the equivalence principle. Data evaluating the quality of this laboratory as a site for such

experiments in the future are also discussed.

Chapter 6 is devoted to the rotational seismology aspect of these efforts. First, an overview of the normal modes of the Earth is presented. These global free oscillations are characterized by discrete frequencies; calculations of these frequencies and the expected response of the instrument are described as well. Finally, a discussion of the interpreted results of data obtained during large earthquakes occurring in South America is given. The study of these data lends itself well to the evaluation of this approach for studying these rotational motions.

Chapter 7 summarizes the progress made by these efforts while describing the specific improvements from which a future instrument might receive the most benefit. In particular, the addition of a stationary "reference" image for the optical readout system which has already been tested outside of the torsion balance setup offers significant improvement of low-frequency measurements. Noise in the system arising from pressure bursts will be discussed in Chapter 4, and improvements to the vacuum chamber which would remedy this problem are discussed here as well. Another modification that a future version of the experiment might benefit from is the replacement of the circular cross section torsion fiber described in Chapter 4, with a rectangular cross section torsion strip. A separate experiment under development in the GEE Lab has shown conclusively a significant reduction in drift by using a torsion strip; this would reduce a major concern voiced during the presentation of data obtained, in Chapter 5, while also improving the likelihood of obtaining a yearlong data set with minimal (or no) human disturbances inside the bunker. Plans to include improved

magnetic shielding, a redesigned balance, and a backup power generator are discussed as well.

The appendices to this dissertation contain additional material, not deemed suitable for the body of the thesis. Appendix A discusses a Lagrangian model of the balance which was developed to describe coupled modes that were observed during an early version of the balance which did not properly damp pendular oscillations. Appendix B includes a few of the most used MATLAB scripts for data analysis and modeling the expected signal for an equivalence principle violation. Appendix C shows the LabVIEW program that has been developed as the interface between the experimenter and the experiment. Balance position from the optical lever, chamber pressure from the ion pump, and temperature from thermistors set up around the experiment was all collected through this program.

Chapter 2

The Equivalence Principle

Galileo is generally credited with making the first observations supporting the concept that, regardless of their composition, any two objects will fall at the same rate in the Earth's gravitational field, provided that air resistance is negligible. When Newton published his laws of motion and the law of universal gravitation in 1787, a mathematical framework to explain Galileo's realization became available. The second law of motion says that the sum of all forces acting on an object is equal to the mass of the object times the acceleration of the object. In this context, the mass that gives a measure of an object's resistance to acceleration when being acted on by some force is referred to as the object's inertial mass, m_I. The law of universal gravitation states that the force due to gravitational attraction between two objects is proportional to the product of the masses of each object. The mass that appears in this context quantifies an object's ability to generate gravitational fields and its response to an external gravitational field, and is called gravitational mass, m_G.

Accordingly, the following expression for the acceleration, $\mathbf{a}$, of an object under the influence of a gravitational field is obtained.

$$\mathbf{F} = m_I \mathbf{a} = -G\frac{M m_G}{r^2}\hat{\mathbf{r}} \tag{2.1}$$

$$\mathbf{a} = -\frac{GM}{r^2}\left(\frac{m_G}{m_I}\right)\hat{\mathbf{r}} \tag{2.2}$$

If m_I and m_G are equal to each other, the acceleration of the object is independent of the mass, composition, or any other characteristics of that object. While there is no known physical reason why this must be the case, to date no measurements have been made that refute the equivalence of inertial and gravitational mass. The condition that all objects experience the same acceleration due to gravity in a given gravitational field is known as the *universality of free fall*.

Einstein described the equivalence principle in the following manner, "we [...] assume the complete physical equivalence of a gravitational field and a corresponding acceleration of the reference system" [11]. That is, an experiment performed in a laboratory under the influence of gravity and an experiment performed in a laboratory free of gravity but being accelerated should produce identical results. In fact, along with the principle of general covariance, the equivalence principle is one of the underlying assumptions made by Einstein when developing his theory of general relativity. As stated by Einstein, the equivalence principle includes the universality of free fall [12].

2.1 Defining the Equivalence Principle

The equivalence principle can be described in multiple forms: the weak equivalence principle, the Einstein equivalence principle, and the strong equivalence principle. Following Will [13], the conditions satisfied by each of these forms are defined below.

Weak Equivalence Principle

The weak equivalence principle, described previously as the universality of free fall, states that any uncharged test mass with negligible influence on the local spacetime metric which is in free fall with some initial position and velocity in spacetime will follow a trajectory influenced in no part by its internal structure or composition. In order for the weak equivalence principle to be valid, all interactions, with the exception of gravity, must contribute equally to inertial and gravitational mass.

Einstein Equivalence Principle

The Einstein equivalence principle requires (i) that the weak equivalence principle is true, (ii) that Local Lorentz Invariance is true, and (iii) that Local Position Invariance is true. Local Lorentz Invariance is the requirement that the outcome of a local non-gravitational experiment be independent of the freely-falling reference frame in which it is performed, while Local Position Invariance requires that the outcome of such an experiment be independent of where and when in the universe it is performed.

Strong Equivalence Principle

While the weak and Einstein forms of the equivalence principle deal with non-gravitational

experiments, the strong equivalence principle extends equivalence to cases where the self mass of the test body affects the local metric of spacetime. This form has all the same requirements as the Einstein equivalence principle for massive objects at the scale of planetary bodies or beyond, which have significant gravitational binding energy. Thus the validity of the strong equivalence principle depends on all interactions, including gravity, contributing equally to inertial and gravitational mass.

In 1960, Schiff conjectured that the validity of the weak form of the equivalence principle guarantees the validity of both Local Lorentz and Position Invariance, thus guaranteeing the validity of the Einstein equivalence principle [14]. According to this conjecture, experiments testing the universality of free fall offer direct empirical evidence for Einstein's equivalence principle. A number of arguments supporting this conjecture have been formulated taking various approaches.

One such argument, based on the assumption of conservation of energy, was originally formulated by Dicke [15], and later developed by Nordtvedt [16] and Haugan [17]. The general thrust of this thought experiment involves considering the total energy of an isolated system of free particles originally at rest at some height in an external gravitational field. The energy required to bind the particles, changes in kinetic and potential energy as the particles fall under the influence of the gravitational field, and the energy required to return the particles back to the initial conditions are accounted for, before comparing the energy of the system at the beginning and end of this cycle. If energy is conserved, this comparison illustrates certain interconnections between the weak equivalence principle and Local Lorentz and Position

Invariance. This idea is discussed in a more concrete, albeit qualitative, summary below.

Considering a body of test particles which are bound together via nongravitational interactions and are moving sufficiently slowly in a weak, static, gravitational field, the laws of motion can be expressed in quasi-Newtonian form. The conserved energy function E_c can be written as

$$E_c = M_R c^2 - M_R U(\mathbf{X}) + \frac{1}{2} M_R V^2 + \mathcal{O}\left(M_R U^2, M_R V^4, M_R U V^2\right) \tag{2.3}$$

where $\mathbf{X}$ and $\mathbf{V}$ are quasi-Newtonian coordinates for the position and velocity of the center of mass of the body, respectively, $M_R c^2$ is the rest energy of the body, and U is the external gravitational potential. The sum of the rest masses of the test particles making up the body, M_0, and the energy required to bind these particles together, E_B, contribute to this rest energy by

$$M_R c^2 = M_0 c^2 - E_B\left(\mathbf{X}, \mathbf{V}\right). \tag{2.4}$$

It is the position and velocity dependence of the binding energy E_B that leads to a violation of the Einstein equivalence principle. Expanding E_B in powers of U and V^2 gives

$$E_B\left(\mathbf{X}, \mathbf{Y}\right) = E_B^0 + \delta m_G^{ij} U^{ij}\left(\mathbf{X}\right) - \frac{1}{2} \delta m_I^{ij} V^i V^j + \mathcal{O}\left(E_B^0 U^2, ...\right) \tag{2.5}$$

where U^{ij} is the external gravitational potential tensor, and δm_G^{ij} and δm_I^{ij} are the anoma-

lous gravitational and inertial mass tensors, respectively. The values of δm_G^{ij} and δm_I^{ij} depend on the internal structure of the body. As discussed by Will [13], δm_G^{ij} is responsible for violations of Local Position Invariance, while δm_I^{ij} is responsible for violations of Local Lorentz Invariance. Dicke used the argument summarized below to show that δm_G^{ij} and δm_I^{ij} also produce violations of the weak equivalence principle, thus showing that the weak equivalence principle implies the Einstein equivalence principle [15].

For n free particles, each with mass m_0, at rest at a location $\mathbf{X} = \mathbf{h}$, the conserved energy as given by Equation (2.3) is

$$E_c = nm_0c^2 \left[1 - U\left(\mathbf{h}\right)/c^2\right]. \tag{2.6}$$

If the binding energy required to form a composite body from the free particles, $E_B\left(\mathbf{h}, \mathbf{0}\right)$ is released in the form of free particles of rest mass m_0 and stored in a massless container, the conserved energy for the composite body becomes

$$E_c = \left[nm_0c^2 - E_B\left(\mathbf{h}, \mathbf{0}\right)\right]\left[1 - U\left(\mathbf{h}\right)/c^2\right] \tag{2.7}$$

while the conserved energy for the free particles in the massless container is

$$E_c = E_B\left(\mathbf{h}, \mathbf{0}\right)\left[1 - U\left(\mathbf{h}\right)/c^2\right]. \tag{2.8}$$

If the composite body falls freely to $\mathbf{X} = 0$, it will experience an acceleration $\mathbf{A}$ given by

$\mathbf{A} = \mathbf{g} + \delta\mathbf{A}$. By definition, the test particles will fall with acceleration $\mathbf{g} = \nabla U$. At $\mathbf{X} = 0$, with both systems at rest, the energies gained are given as

$$E_K = -\left[nm_0 - E_B\left(\mathbf{0}, \mathbf{V}\right)/c^2\right]\mathbf{A}\cdot\mathbf{h} - \delta m_I^{ij} g^i h^j \tag{2.9}$$

and

$$E_K = -E_B\left(\mathbf{h}, \mathbf{0}\right)\mathbf{g}\cdot\mathbf{h}/c^2. \tag{2.10}$$

Keeping terms below order $\left(\mathbf{g}\cdot\mathbf{h}\right)^2$, the conserved energy of the total system is now given by

$$E_c = E_B\left(\mathbf{h}, \mathbf{0}\right)\left[1 - U\left(\mathbf{0}\right)/c^2\right] - E_B^0\mathbf{g}\cdot\mathbf{h}/c^2 - \left(nm_0 - E_B^0/c^2\right)\mathbf{A}\cdot\mathbf{h} - \delta m_I^{ij} g^i h^j. \tag{2.11}$$

After extracting the energy to break the body into its n free particles $E_B(\mathbf{0},\mathbf{0})[1 - U(\mathbf{0})/c^2]$, and the kinetic energy to return the particles to their initial positions at $\mathbf{X} = \mathbf{h}$, $-nm_0\mathbf{g}\cdot\mathbf{h}$, if the energy has been conserved, the remaining terms of Equation (2.11) must equal 0.

Thus

$$E_B\left(\mathbf{h}, \mathbf{0}\right) - E_B\left(\mathbf{0}, \mathbf{0}\right) - \left(nm_0 - E_B^0/c^2\right)\delta\mathbf{A}\cdot\mathbf{h} - \delta m_I^{ij} g^i h^j = 0. \tag{2.12}$$

Using $E_B(\mathbf{h},\mathbf{0}) - E_B(\mathbf{0},\mathbf{0}) = \delta m_G^{ij} \nabla U^{ij} \cdot \mathbf{h}$, Equation (2.12) can then be used to find an expression for acceleration A^i

$$A^i = g^i + \left(\delta m_G^{jk}/M_R\right) U^{jk} - \left(\delta m_I^{ij}/M_R\right) g^j \tag{2.13}$$

where $M_R \equiv nm_0 - E_B^0/c^2$. The first term to the right of the equal sign is the gravitational acceleration as expected, thus if the weak equivalence principle is true, $\delta m_G^{jk} \equiv \delta m_I^{jk} \equiv 0$. But, for a violation of Lorentz Location or Position Invariance the anomalous mass tensors δm_G^{jk} and δm_I^{jk} are non-zero, showing that not only is the weak equivalence principle violated in this case, but so is the Einstein equivalence principle.

In general, tests of the equivalence principle seek to compare the accelerations, a, of two different test masses, say A and B. The sensitivity of such a test is given in terms of the Eötvös parameter, η, defined by

$$\eta_{A,B} = \frac{a_A - a_B}{[a_A + a_B]/2} = \frac{(m_g/m_i)_A - (m_g/m_i)_B}{\left[(m_g/m_i)_A + (m_g/m_i)_B\right]/2}. \tag{2.14}$$

Given that different interactions may contribution differently to the inertial and gravitational mass of an object, the materials chosen for tests of the equivalence principle generally have different internal structures. Special interest is paid to proton-to-neutron ratios, and contributions due to the binding energies from strong, weak, electromagnetic and gravitational interactions. Further discussion of potential causes of an equivalence principle violation, or what such a violation might look like takes place in § 2.2.

2.2 Motivations for Testing the Equivalence Principle

An overview of some of the theoretical and observational motivations for testing the equivalence principle is presented. The length scales of these motivations range from the possibility of yet undetectable compactified dimensions to observations on the cosmological scale, offering some insight into the overarching scope of this subject.

2.2.1 Test of General Relativity

The general theory of relativity (GR) is the classical relativistic theory of gravity formulated by Einstein which has passed every experimental test of its validity since its inception in 1915. Along with the classic tests of GR: the successful explanation of the perihelion precession of Mercury's orbit around the Sun, the observation of gravitational lensing (e.g. the deflection of starlight as it passes near the Sun, first observed by Eddington during a solar eclipse in 1919), and the gravitational redshift of light which was proven in 1959 by the Pound-Rebka experiment, Einstein's theory has stood up to modern tests conducted with greater precision [18–20]. These tests include observations of gravitational lensing and redshift to high precision, Shapiro delay during the propogation of signals through varying gravitational potentials, frame dragging, strong field tests, the recent direct detection of gravitational waves, cosmological tests, and tests of the equivalence principle (see, for example, [21–27]). In fact, it is the tests of the equivalence principle that offer the most precise tests of GR to date [28].

Along with general covariance, GR is founded on the complete validity of the equivalence principle, thus any observation violating the equivalence principle is an indication that GR is not a complete description of gravitational interactions. Theorists such as Damour have argued that the essential role that GR plays in the current description of the universe necessitates further testing of the theory to the highest precision possible [8, 28].

2.2.2 Theoretical Attempts at a Unified Theory

Just as Einstein's theory of GR has passed every experimental test to date, the Standard Model of particle physics, which governs the electromagnetic, weak, and strong nuclear interactions, has been tested extensively without the discovery of a single contradiction. However, the two theories are incompatible. Efforts to unify GR and the Standard Model with a single unifying theory have long been ongoing in theoretical physics, and in fact, nearly every attempt to extend physics beyond the present framework (Kaluza-Klein, String Theory, etc.) predicts a violation of the equivalence principle [28].

In General Relativity, the equivalence principle is a consequence of the universal coupling between matter and gravity which is obtained by considering a curved spacetime metric $g_{\mu\nu}$. The total action S of the matter-gravity system is given by the sum

$$S\left[\psi, A, \Phi, g_{\mu\nu}\right] = S_{SM}\left[\psi, A, \Phi; g_{\mu\nu}; g_a, Y, \lambda, \mu\right] + S_g\left[g_{\mu\nu}; G\right] \tag{2.15}$$

where ψ, A, and Φ denote the fields of the Standard Model: Fermions, gauge fields,

and Brout-Englert-Higgs scalar field respectively, g_a gives the $U(1) \times SU(2) \times SU(3)$ gauge couplings, Y gives the Yukawa couplings, and λ and μ are the quartic coupling and mass parameter of Φ. In the current framework, the masses and various couplings involved in Equation (2.15) are absolute with the exception of the dynamical field $g_{\mu\nu}$, which replaces the absolute structure of the Poincarè-Minkowski metric $\eta_{\mu\nu}$ [8].

This asymmetry has long been questioned [29–32], and with the musings of theories with addition dynamical coupling constants came the realization that these theories would entail a violation of the equivalence principle. In particular, Dicke pointed out that the acceleration during free-fall deduced from the action of an object subject to spatially dependent coupling constants will differ for objects with different compositions [15].

Dilaton models suggested by string theory introduce a scalar field $\varphi(t, \mathbf{x})$ which monitors the spacetime variability of the gauge, Yukawa, and gravitational coupling constants. Studies of equivalence principle violations induced by dilaton models suggest that contributions to this violation might arise from factors like Coulomb effects in proton and neutron mass, and in the binding energy of the nucleus, and quark-mass dependence of surface nuclear binding energies. Such a violation is expected to take the general form

$$\eta_{A,B} = Q_A - Q_B \tag{2.16}$$

where $\eta_{A,B}$ is the Eötvös parameter, defined in terms of a comparison of differential accelerations in Equation (2.14), and Q_i is defined for some material (labeled here as i) by

$$Q_i = \left(c_1 \frac{Z(Z-1)}{A^{4/3}} + \frac{c_2}{A^{1/3}} + c_3 \frac{A-2Z}{A} + c_4 \frac{(A-2Z)^2}{A^2} \right). \tag{2.17}$$

Here $A \equiv N + Z$ gives the nucleon number of the material, Z is the atomic number, and c_j are some constants which are expected to depend on the dilaton φ [8, 33, 34].

In [35, 36], Damour and Donoghue argue that the dominant effects contributing to an equivalence principle violation are contained in the first two terms on the right-hand side of Equation (2.17). The first term, which involves Coulomb nuclear effects, is estimated as

$$Q'_e = +7.7 \times 10^{-4} \frac{Z(Z-1)}{A^{4/3}}. \tag{2.18}$$

The second term considers the effects of surface nuclear binding energies,

$$Q'_{\hat{m}} = -\frac{0.036}{A^{1/3}} - 1.4 \times 10^{-4} \frac{Z(Z-1)}{A^{4/3}}. \tag{2.19}$$

Combining these dominant terms with dilaton coefficients D_e and $D_{\hat{m}}$, which have been limited by experimental results to magnitudes on the order of 10^{-9}, Equation (2.16) takes the form [8]

$$\eta_{A,B} \approx \left(D_e Q'_e + D_{\hat{m}} Q'_{\hat{m}}\right)_A - \left(D_e Q'_e + D_{\hat{m}} Q'_{\hat{m}}\right)_B . \tag{2.20}$$

Such a model may be used as a guideline for selecting materials to compare in experiments searching for a violation of the equivalence principle. Table 2.1 lists these dominant charges

Material	A	Z	$Q'_e(\times 10^{-3})$	$-Q'_{\hat{m}}(\times 10^{-3})$
Li	7	3	0.345	18.88
Be	9	4	0.494	17.40
Al	27	13	1.48	12.27
Si	28.1	14	1.64	12.1
SiO_2	-	-	1.34	13.39
Ti	47.9	22	2.04	10.28
Fe	56	26	2.34	9.83
Cu	63.6	29	2.46	9.47
Cs	133	55	3.37	7.7
Pt	195.1	78	4.09	6.95

Table 2.1: Dilaton "charges" for sample materials averaged over the isotopic or chemical composition [8].

Q'_e and $Q'_{\hat{m}}$ for some sample materials.

In terms of Newtonian dynamics, the introduction of a dilaton φ leads to an interaction potential of the form

$$V(r) = -G\frac{m_A m_B}{r}\left(1 + \alpha_A \alpha_B e^{-m_\varphi r}\right) \tag{2.21}$$

where α_A and α_B are dimensionless factors that describe the scalar coupling to matter. This coupling is given by

$$\alpha_A = \frac{1}{\kappa m_A}\frac{\partial[\kappa m_A(\varphi)]}{\partial[\kappa\varphi]} \tag{2.22}$$

where $\kappa \equiv \sqrt{4\pi G}$ is the inverse of the Planck mass [35].

2.2.3 Dark Matter and Dark Energy

Astronomical observations of dark matter and dark energy provide further motivation for studying gravitation, specifically through tests of the equivalence principle. Dark matter is the name given to nonluminous matter that interacts gravitationally with ordinary, baryonic matter, but is transparent to electromagnetic radiation. Its presence has been inferred via measurements of the rotation rates of spiral galaxies, as well as its influence on distant starlight (through gravitational lensing) passing by clusters of galaxies, studies of large scale structure formation in the universe, and the anisotropies of the cosmic microwave background [37–42]. Current measurements predict that dark matter makes up 23% of the mass of the universe [43]. Models that propose dark matter candidates, such as WIMPs (weakly interacting massive particles) and axions, provide the possibility that these particles may be subject to non-gravitational interactions with ordinary matter [44, 45]. Laboratory tests of the equivalence principle are able to constrain these interactions while testing free fall towards the significant amount of dark matter located in the central regions of the Milky Way Galaxy [3, 46, 47].

Dark energy is the phenomenon responsible for the accelerated expansion of the universe, discovered through observations of the redshift of Type Ia supernovae during the 1990s [48,49]. An additional indication of physics at work beyond the current framework, proposed theories explaining dark energy include the cosmological constant or Lambda-CDM model, and quintessence. Quintessence involves a dynamical scalar field that has been proposed to

account for most of the energy density of the Universe; such a field would lead to a violation of the equivalence principle [50, 51]. In contrast to quintessence, the Lambda-CDM model depends on an absolute cosmological constant; thus tests of the equivalence principle can help distinguish between such theories.

2.3 Survey of the Field

Formal tests of the equivalence principle span parts of four centuries. A brief review of past and ongoing experiments that used pendulums or torsion balances to place limits on a violation of the equivalence principle is presented, as well as planned spaceborne tests that would be able to supersede current limits. In the historical context, experiments that made significant advances in technology or technique are highlighted, with the limits achieved in these experiments presented in Figure 2.1.

2.3.1 The Classical Tests

The earliest high precision experimental tests of the equivalence principle were conducted by Newton, and later others, using a simple pendulum. The period T of a pendulum with length l in a gravitational field g is given by

$$T = 2\pi \left(\frac{m_i}{m_g}\right)^{1/2} \left(\frac{l}{g}\right)^{1/2}. \tag{2.23}$$

By comparing multiple pendulums with the same lengths but made of different materials,

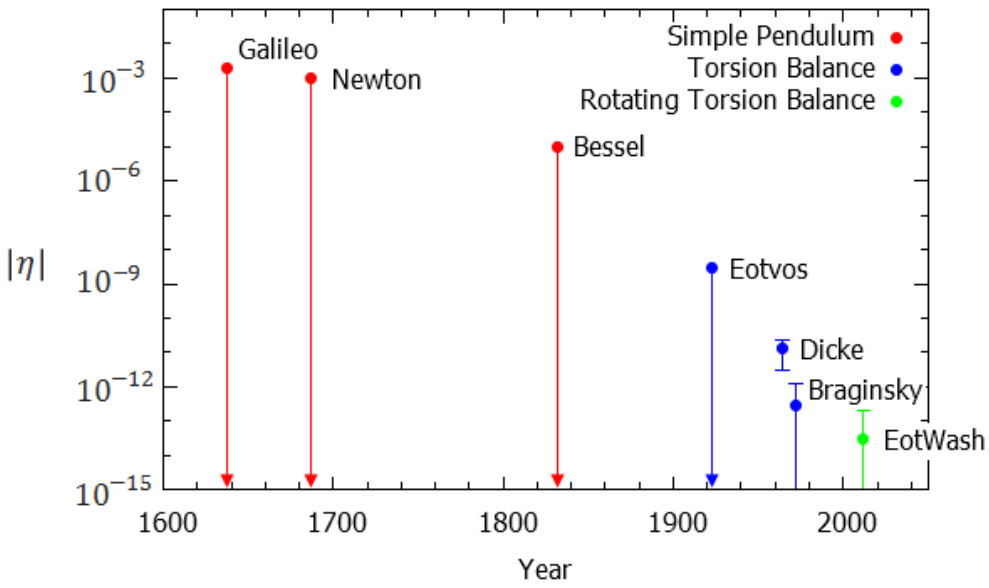

Figure 2.1: Limits on an equivalence principle violation obtained via notable laboratory experiments using simple pendulums, torsion balances, or rotating torsion balances.

a limit on the Eotvos parameter can be deduced

$$\eta_{A,B} = \frac{\Delta T^2}{T^2}. \tag{2.24}$$

Newton tested the equivalence of materials such as gold, silver, lead, glass, salt, wood, water, and wheat using a simple pendulum obtaining limits that can interpreted as $\eta < 10^{-3}$. Bessel (1889), Thomson (1909), and Potter (1923) conducted subsequent pendulum tests of the equivalence principle, reaching progressively improved sensitivities as shown in Table 2.2.

A monumental step forward in tests of the equivalence principle occurred with the introduction of the torsion balance for such tests by Eötvös starting in the 1890s. Eötvös' instrument, which is shown in Figure 2.2, obtained it's best results using the so called terres-

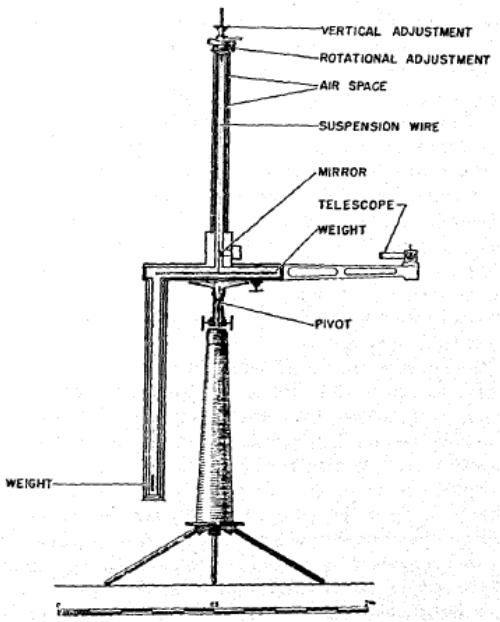

Figure 2.2: A drawing of the torsion balance used by Eötvös to test the equivalence principle [1].

trial attractor scheme. In this approach, a torsion balance with different materials at each end is subject to centrifugal forces due to the earth's rotation, as well as the force due to the earth's gravitational field. If the inertial and gravitational masses of the materials at each end of the balance differ, a torque will act on the balance which will tend to twist the balance. By turning the balance by 180°, the direction of this deflection is switched. Eötvös' balance

	Year	*Materials Tested*	η
Galileo	1638	Pb, cork	$< 2 \times 10^{-3}$
Newton	1687	Au, Ag, Pb, glass, salt, wood, water, wheat	$< 10^{-3}$
Bessel	1832	Fe, Zn, Pb, Ag, Au, Fe_3O_4, marble, clay, quartz	$< 10^{-5}$
Thomson	1909	UO_2 and PbO	5×10^{-6}
Potter	1923	brass, Pb, NH_4F, duralumin	$< 8 \times 10^{-6}$

Table 2.2: Simple pendulum tests of the equivalence principle [9].

operated at normal pressure and room temperature, but within an enclosure of three metal walls which reduced temperature variations and convection current around the balance. His experiment, which compared a wide range of materials to test masses made from platinum and copper, obtaining a limit on the parameter later named for his work of $\eta = 3 \times 10^{-9}$.

The experiment conducted at Princeton during the early 1960s by a group led by Dicke [1] made the next significant leap in equivalence principle test design by instead monitoring the balance's response to the gravitational field produced by the sun, and using the natural rotation of the Earth to smoothly modulate any signal caused by a violation. While the acceleration due to the Sun $g_\odot \approx 0.59$ cm s^{-2} tends to be less than acceleration due to centrifugal acceleration used for the terrestrial scheme ($a_\oplus \approx 1.6$ cm s^{-2} in Eötvös' experiment), the ability to leave the experiment undisturbed for long integration times as the Earth's rotation modulates the signal offers a significant advantage. Using a balance with threefold symmetry and test masses of 30 g hanging from a fused silica frame, suspended from a fused silica torsion fiber inside of a stainless steel vacuum chamber Dicke placed a limit on an equivalence principle violation at $\eta_{Al,Au} = 3 \times 10^{-11}$ with 95% statistical confidence. Dicke's experiment operated in an underground pit to reduce thermal variation and other noise sources, and the position of the balance was monitored using an optical lever and electrostatic feedback system. Though the Dicke experiment was well thought out and employed a number of ingenious techniques, nearby construction limited the final sensitivity of this experiment. While data were collected for a few years, no uninterrupted stretches longer than a few days were obtained.

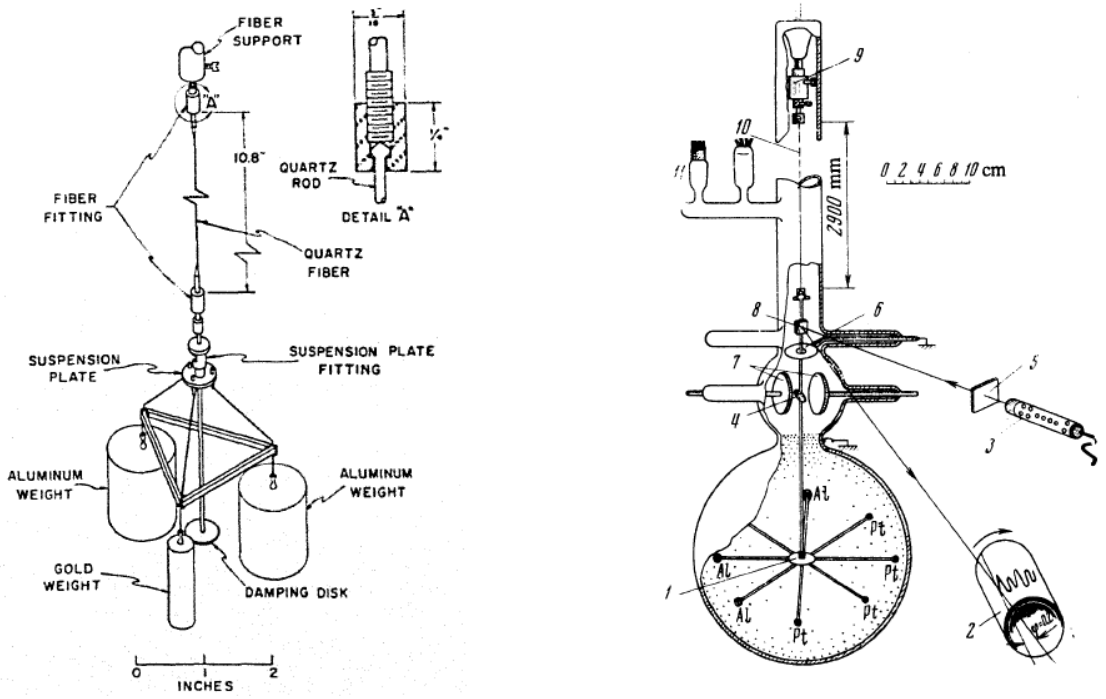

Figure 2.3: Left: A drawing of the balance used in Dicke's test of the equivalence principle with key components labeled [1]. Right: A drawing of Braginsky's experiment, taken from [2].

Several years later, during the early 1970s, Braginsky used the solar attractor approach taken by Dicke to improve the limits on an equivalence principle violation in at test conducted in Moscow [2]. Using a torsion balance with four aluminum masses and four platinum masses with a total mass of only 4.4 g, suspended from a 5 µm diameter, 2.90 m long tungsten fiber, and operating at a pressure of less than 10^{-8} torr in a glass vacuum chamber, Braginsky achieved a limit of $\eta_{Al,Pt} = 9 \times 10^{-13}$. Data collection for this experiment spanned only 3 weeks in February of 1971, with frequent interruptions during this time.

The experiments of Dicke and Braginsky suffered from disturbances which limited them from achieving their theoretical sensitivities. By taking advantage of technological advances since these experiments, as well as obtaining longer data sets, improvements stand to be

made using the solar attractor approach.

2.3.2 Rotating Torsion Balance Experiments

Over the past 25 years, the Eöt-Wash group at the University of Washington has developed a torsion balance test of the equivalence principle mounted on a turntable rotating at a controlled uniform rate [3,47,52–55]. This approach allows them to use a local gravitational source with an acceleration larger than $g_\odot$ while both increasing the frequency of a potential violation signal and avoiding sources of noise also occurring with a daily frequency, such as the diurnal temperature swing. In contrast to experiments using the gravitational field of the Sun to search for an equivalence principle violation, the experiments by the Eöt-Wash group also offer a means to search for a violation arising over length scales of less than 1 AU, such as those that might arise from a "fifth force" acting at intermediate-ranges. However, operating a rotating torsion balance offers additional challenges; the rotation rate must be kept incredibly uniform to avoid introducing a false signal. In addition, tilt of the fiber suspension point and gravitational gradients which would potentially simulate a signal at the balance rotation frequency need to be monitored and accounted for to high precision, and avoided whenever possible.

The most recent version of the Eöt-Wash experiment, illustrated schematically in Figure 2.4, placed a limit on an equivalence principle violation of $\eta_{Be,Ti} = (0.3 \pm 1.8) \times 10^{-13}$. Considering a violation due to acceleration towards the sun, this experiment has obtained a limit of $\eta_{Be,Ti} = (-3.1 \pm 4.7) \times 10^{-13}$ [3].

2.3.3 Lunar Laser Ranging

The Apache Point Observatory Lunar Laser-ranging Operation (APOLLO) has measured the Earth-Moon separation to a level of about a millimeter by measuring the amount of time it takes for short laser pulses to travel from the observatory in southern New Mexico to retroreflectors placed on the Moon by American astronauts and Soviet rovers, and back to Earth [56]. The gravitational binding energies of the Earth and Moon contribute to their total mass at the 10^{-10} level [57], thus the effects from a violation of the strong equivalence principle can be looked for by mapping the shape of the lunar orbit, as it is in free fall around

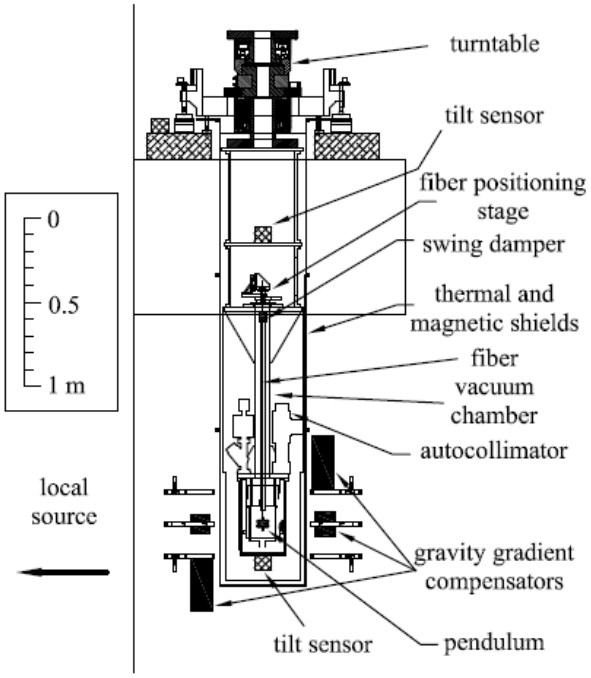

Figure 2.4: A schematic drawing of the Eöt-Wash rotating torsion balance test of the equivalence principle. The most sensitive limits placed by in this experiment involve comparing the acceleration of test masses towards a hillside located just beyond the wall of the laboratory [3].

the Earth. The motion of the Earth-Moon system towards the sun and the galactic center can also be studied. A violation of the strong equivalence principle can be parameterized as

$$\frac{m_g}{m_i} = 1 + \eta_{SEP}\frac{U}{mc^2} \tag{2.25}$$

where η_{SEP} is a dimensionless parameter constraining a violation of the strong equivalence principle, U is the body's gravitational self-energy, and mc^2 is the total mass-energy of the body [58]. As the most sensitive test of the strong equivalence principle to date, APOLLO has used the acceleration of the Earth and Moon by the Sun's gravitational field to place bounds at the level of $\eta_{SEP} = (3.0 \pm 3.6) \times 10^{-4}$ [58, 59]. Bounds of the weak equivalence principle obtained via lunar laser ranging are comparable to limits achieved in the laboratory, with $\eta = (-0.8 \pm 1.3) \times 10^{-13}$ [58].

2.3.4 Space-Based Tests

Satellite experiments offer certain advantages in terms of tests of the equivalence principle, namely they can study the true "free fall" acceleration of different test masses, while torsion balance tests are looking only at the horizontal component of this acceleration. In addition, space-based experiments avoid seismic noise sources that can be troublesome for torsion balance experiments. MicroSCOPE (Micro-Satellite à traînèe Compensèe pour l'Observation du Principe d'Equivalence) is a minisatellite mission that will test the universality of free fall for test masses made from two different materials. Each test mass is an ultrasensitive differ-

ential accelerometer which is electrostatically constrained; an equivalence principle violation would be indicated by a non-zero difference of the electric potentials applied to keep the masses in equilibrium [60]. This experiment is expected to obtain a resolution of $\eta \approx 10^{-15}$, and is on schedule to launch on board a Soyuz in April 2016 [61].

A still more ambitious satellite experiment, STEP (Satellite Test of the Equivalence Principle) is a proposed test of the equivalence principle that has a similar design to Micro-SCOPE, but involves a complex cyrogenic cooling system that reduces thermal noise allowing a projected sensitivity of $\eta \approx 10^{-18}$ [62]. Benefiting from the technological innovations of the Gravity Probe-B mission, STEP would compare the motions of four pairs of test masses, using SQUID sensors to measure accelerations. The experiment has been in development since the late 1970s, but has yet to secure the funding that will be required to get the project into orbit.

Another proposed test of the equivalence principle is SR-POEM (Sounding-Rocket based Principle Of Equivalence Measurement), which would be conducted during the free fall portion of a sounding rocket flight. The experiment would involve eight separate drops, each with a duration of approximately 120 seconds, with the difference in acceleration of a pair of test masses monitored using a set of four subpicometer tracking frequency laser gauges. The expected sensitivity of this experiment is at the level of $\eta < 2 \times 10^{-17}$ [63].

Chapter 3

Technical Challenges

Specific key aspects of a torsion balance experiment capable of searching for a violation of the equivalence principle at unprecedented levels while also studying the torsional normal modes of the Earth have been identified and were implemented as part of the prototype instrument described here. A detailed model of the signal expected from this instrument for a hypothetical violation of the equivalence principle was developed. Significant effort was put into the design and development of a multi-slit auto-collimating optical lever with a large dynamic range and high resolution to passively monitor the position of the torsion balance, as well as a sensitive torsion balance with an extremely long period which was characterized and operated in a remote underground laboratory. Each of these objectives will be motivated and described in detail below.

3.1 Model of Expected Signal

One major element of this work has been the development of a thorough model of the signal expected for a violation of the equivalence principle. The experiment follows the solar attractor scheme as implemented by Dicke [1] and Braginsky [2], comparing the gravitational attraction between the Sun and the torsion balance test masses and the centrifugal forces acting on the test masses produced by the motion of the Earth in its orbit. A difference in the ratios of the gravitational and inertial masses of the balance test masses, which are made of two different materials, would produce a deflection of the balance as one material "falls" towards the Sun more quickly than the other. The balance used in this experiment is comprised of four test masses secured at the ends of a lightweight cross. The masses are made of two different materials, arranged to create a composition dipole as illustrated in Figure 3.1. To model the signal produced by a violation of the equivalence principle, consider the magnitude of the torque acting on each of the four test masses of the torsion balance in Figure 3.1, when the Sun is at the horizon

$$\begin{aligned} \tau &= \sum |\mathbf{r} \times \mathbf{F}| \\ &= mr \left[\sin\left(\phi - \phi_b - \frac{\pi}{4}\right) + \sin\left(\phi - \phi_b + \frac{\pi}{4}\right) \right] (a_A - a_B) \end{aligned} \tag{3.1}$$

where $m \approx m_A \approx m_B$ is the mass of each of the balance test masses, a_A and a_B are the accelerations due to gravity towards the Sun of the test masses made of materials A and B

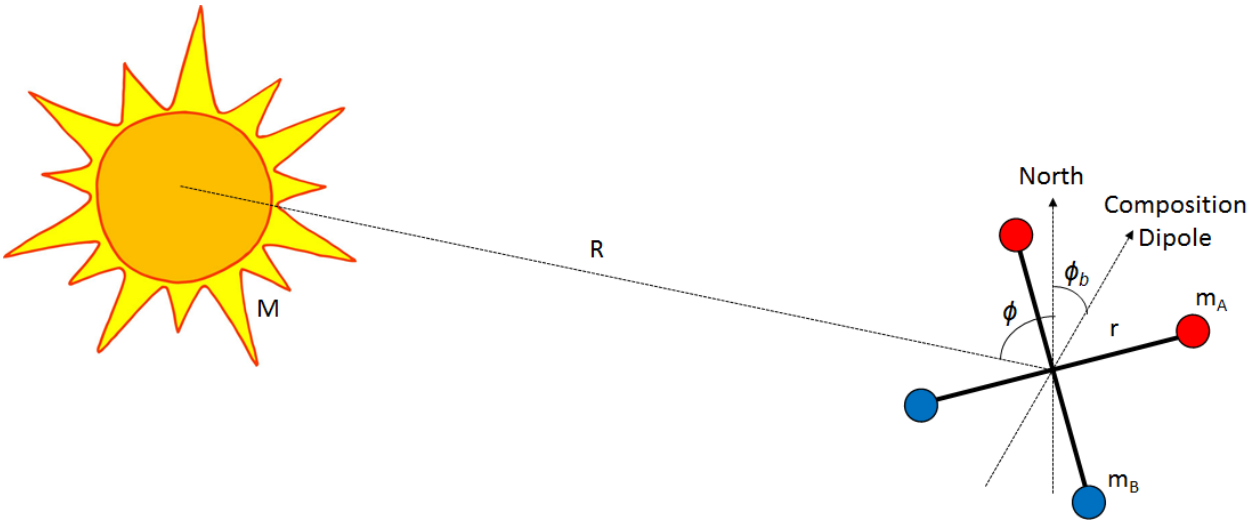

Figure 3.1: Illustration of the general concept of the experiment, viewed top down. Two of the test masses are made of 'material A' (shown in red) and two are made of 'material B' (shown in blue). Illustration not drawn to scale.

respectively, r is the distance between the center of the balance and a test mass, and ϕ_b is the direction of the composition dipole with respect to astronomical true north as illustrated in Figure 3.1.

A strength of the solar attractor approach is that the rotation of the Earth provides a naturally smooth and well characterized modulation of the signal for an EP violation. Taking $a_\odot = (a_A + a_B)/2 = GM/R^2$ and using the definition of η given in Equation (2.14), a final expression for the torque acting on the balance due to an EP violation is given by

$$\tau = \eta GMmrp \sin(\phi - \phi_b) \sin\zeta / R^2. \tag{3.2}$$

Here G is the Newton's gravitational constant, M is the mass of the Sun, p is a parameter that depends on the geometry of the balance, $\phi - \phi_b$ is the difference between the azimuthal

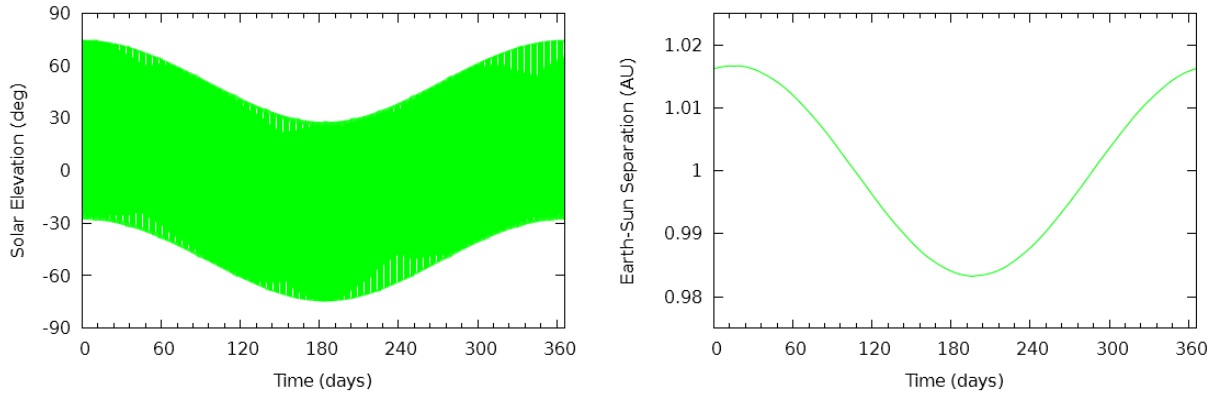

Figure 3.2: Left: The solar elevation (in degrees above the horizon) which is equal to $90° - \zeta$ where ζ is the zenith angle. Right: The distance between the Earth and Sun in astronomical units throughout the year, $t = 0$ at 00:00:00 UTC on 21 June 2015.

angle of the Sun and the composition dipole of the balance, ζ is the zenith angle of the Sun, R is the Sun-Earth separation, and m and r are the magnitudes of balance parameters defined for Equation (3.1). The true values of ϕ, ζ, and R over the course of the year that the experiment ran are available from the JPL Horizons website [64].

To model the balance response to this torque, consider the well known equation of motion for a damped harmonic oscillator driven by a sinusoidal torque with amplitude τ_s and driving frequency ω_s

$$\ddot{\theta} + 2\beta\dot{\theta} + \omega_0^2\theta = \frac{\tau_s}{I}\cos\omega_s t. \tag{3.3}$$

As usual, θ gives the angular displacement of the balance, β is a damping parameter, ω_0 is the natural torsional frequency of the balance, and I is moment of inertia of the balance about the vertical axis. The particular solution to this equation is given by

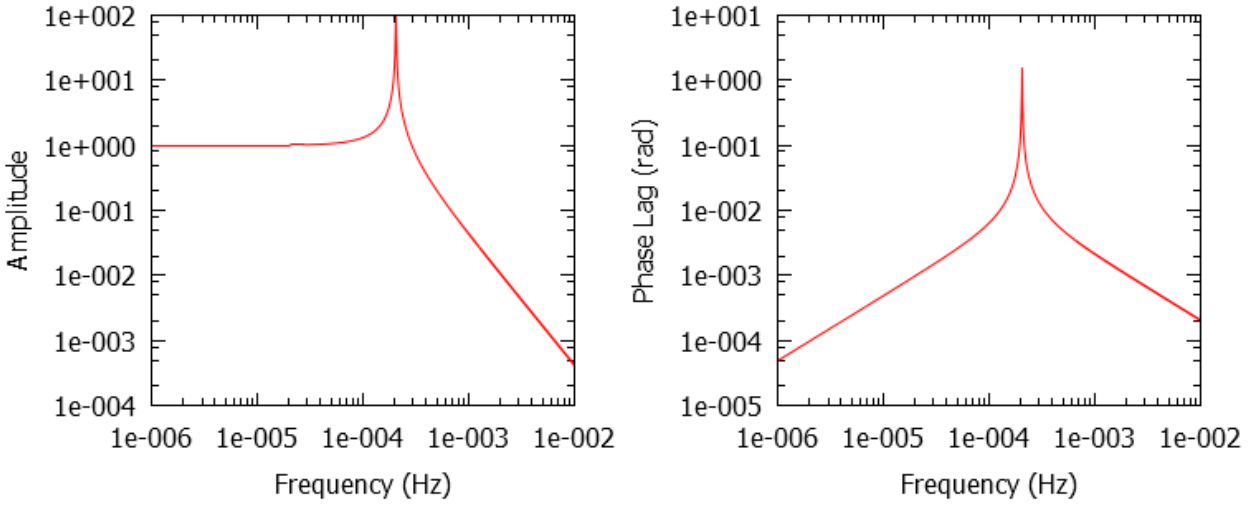

Figure 3.3: Left: The coefficient $A(\omega) \equiv \omega_0^2/\sqrt{(\omega_0^2-\omega^2)^2+\omega^2\omega_0^2/Q^2}$ from Equation (3.4); $A(\omega_s) = 1.0025$ for the balance parameters described in this thesis with a natural frequency $f_0 = 2 \times 10^{-4}$ and $Q = 100$; $\omega_s = 2\pi f_s$, where f_s is the signal frequency for a potential equivalence principle violation. Right: The phase lag of the balance response; $\delta(\omega_S) = 5 \times 10^{-4}$ which corresponds to a shift of 7 seconds. What is actually plotted is the absolute value of the phase lag; for $\omega > \omega_0, \delta < 0$.

$$\theta_p = \frac{\omega_0^2}{\sqrt{\left(\omega_0^2-\omega^2\right)^2+\omega^2\omega_0^2/Q^2}}\frac{\tau_s}{\kappa_f}\cos\left(\omega_s t-\delta\right) \tag{3.4}$$

where the relationships $I = \kappa_f/\omega_0^2$ and $Q = \sqrt{\omega_0^2-2\beta^2}/2\beta \approx \omega_0/2\beta$ have been used. The quality factor Q is large for a balance with minimal damping, and the rigidity of the torsion fiber, given by κ_f, is a measure of the fiber's restoring torque. The phase lag of the balance response δ is given by

$$\delta = \tan^{-1}\left(\frac{\omega\omega_0/Q}{(\omega_0^2-\omega^2)}\right). \tag{3.5}$$

For details of these derivations see, for example, Thornton and Marion [65]. The mag-

nitude of the coefficient $A(\omega) \equiv \omega_0^2/\sqrt{(\omega_0^2-\omega^2)^2+\omega^2\omega_0^2/Q^2}$ from Equation (3.4) and the phase lag of the balance response δ to the driving torque are plotted in Figure 3.3. Using $f_0 \equiv \omega_0/(2\pi) = 2\times10^{-4}$ and $Q = 100$, approximate values for the balance described in Chapter 4, it is shown that for a driving signal at frequency $f_s = 1.157 \times 10^{-5}$ Hz Equation (3.4) approaches

$$\theta = \tau/k_f. \tag{3.6}$$

Taking m, r, p, and the fiber torsion constant k_f, for the balance and fiber described in § 4.1 and § 4.2, plots of the expected deflection of the balance for an EP violation at the level of $\eta = 10^{-12}$ are shown in Figure 3.4 for North-South and East-West balance orientations. The larger signal is obtained for a North-South orientation of the composition dipole, $\phi_b = 0$.

3.2 Development of a High Dynamic Range, High Resolution Angular Readout System

A crucial challenge to conducting a thorough torsion balance test of the equivalence principle is the ability to precisely monitor the position of the torsion balance over an extended period of time. Thus, a significant effort has been placed on the development and characterization of an instrument with a large dynamic range that is able to monitor the position of the torsion balance with adequate precision. The ability to operate over a large range is a critical aspect

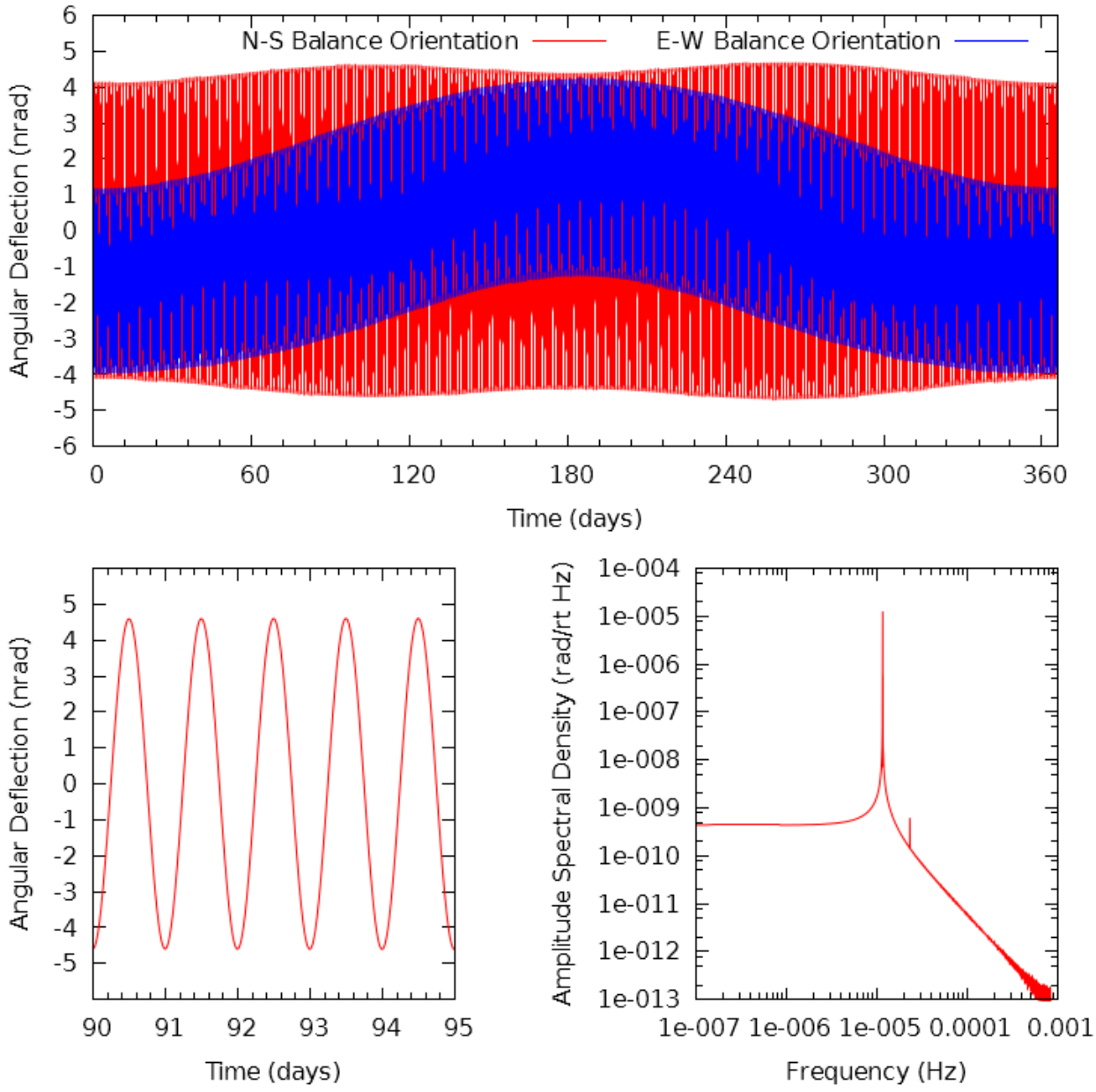

Figure 3.4: Top: Expected deflection of the balance for a violation at the $\eta = 10^{-12}$ level with the balance composition dipole in the North-South direction (in red) and in the East-West direction (in blue). Bottom Left: An enlarged portion, shown for the balance oriented with its composition dipole in the North-South direction. Bottom Right: The amplitude spectral density of the expected balance deflection for a equivalence principle violation at the $\eta = 10^{-12}$ level with the balance oriented with its composition dipole in the North-South direction. The signal frequency occurs at $f_s = 1.157 \times 10^{-5}$ Hz, and it has a bandwidth of approximately 10^{-7} Hz. For all of the solar data taken from the JPL Horizons website shown here, $t = 0$ is 00:00:00 UTC on 21 June 2015 (19:00:00 on 20 June 2015 local time).

of an experiment designed to collect data continuously for periods months or years. Torsion fibers tend to have some intrinsic drift that gradually shifts the equilibrium position of the balance over time. For experiments with a readout range of only a few µrad, this drift places a stringent limit on the length of a continuous data run.

Furthermore, in order to detect the effects of extremely small accelerations due to an equivalence principle violation or rotational ground motion corresponding to the Earth's normal modes, the ability to resolve tiny angular displacements of the balance is crucial. For instance, for the balance described in this thesis, a violation of the equivalence principle at the $\eta \approx 10^{-12}$ level would lead to a torque of $\sim 3 \times 10^{-17}$ Nm and a corresponding angular deflection of the balance of $\sim 5 \times 10^{-9}$ rad.

The forces acting on the torsion balance can be measured by one of three approaches [66]:

(1) The balance is permitted to oscillate freely while its position is measured passively. The forces acting on the balance are then deduced from the motion of the balance.

(2) The balance can be held by means of a feedback system, where the voltage applied to electrodes near the balance required to maintain the balance's position is used to indicate the forces acting on the balance.

(3) The change in the precisely measured period of a balance oscillating with a relatively large amplitude can be used to deduce the forces acting on the balance [67].

Taking the first approach, a multi-slit auto-collimating optical lever with ∼nanoradian resolution, built in-house, is used monitor the balance. Several modifications have been made

to the design reported in Cowsik et al. [4] which are presented along with a general overview of the instrument. In its present state, this instrument has a range of ∼10 mrad and a resolution on the order of a nanoradian. In fact, key concepts from this design have already been put to use by other efforts in experimental gravitation [68, 69].

3.2.1 The Auto-collimating Optical Lever

The optical lever is well suited for sensitive experiments where angular measurements are needed; in addition to its high angular resolution and large dynamic range, it applies negligible torques on the object of interest. Furthermore, the auto-collimating arrangement eliminates sensitivity to small translations of the target mirror along the beam path. A diagram of the optical lever used in this experiment is shown in Figure 3.5. An array of slits, S, is illuminated by a light source. The light is reflected off of a flat mirror, M_1, which is used to locate the virtual image on the focal plane close the the optic axis. The reflected light then passes through an achromatic field lens, L, and emerges as a set of collimated beams, one for each slit. The collimated light beams are then reflected off of a flat mirror, M_2, attached to the object of interest, then pass back through the field lens and form a well focused image, I, on a linescan CCD detector located in the focal plane of L.

The illuminated array of slits produces an image of multiple peaks, the center of adjacent peaks are spaced 182 µm apart. The image is captured by a PerkinElmer linescan CCD camera consisting of 2048 pixels, each 14 µm by 14 µm. The camera's optimal operation occurs when the number of electrons captured in its CCD wells is about 70% of the well

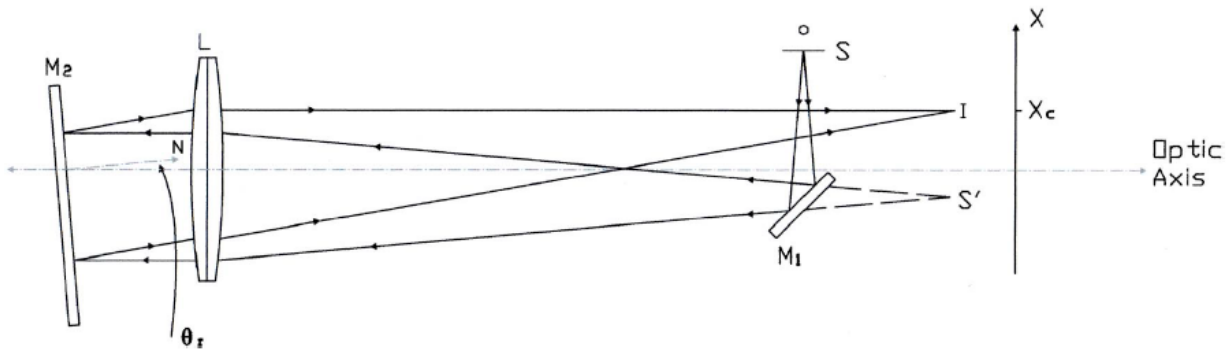

Figure 3.5: Diagram illustrating the principles of the multi-slit optical lever in an autocollimating arrangement. Figure taken from Cowsik et al. [4]

depth, thus the camera is triggered externally at a rate chosen such that the peak maxima are near this magnitude. The size and quality of the target mirror, optical port, and to some extent the length of the total beam path affects the intensity of the image that returns to the CCD camera. For the data collected during the experiment, an acquisition rate of $\sim$500 Hz was used, and 500 individual frames are summed to make an image giving $\sim$1 image per second. This image is digitized using an 8-bit National Instruments PCI-1428 image aquisition device and is passed through a centroiding routine which determines the central value of each peak of the image, then finds the center of the image from the positions of each peak. The change in this centroid value, denoted as Δx_c, is related to the change in the angular position of the object of interest by

$$\Delta\theta = \frac{\Delta x_c}{2f} \tag{3.7}$$

where $f = 100\,\text{cm}$ is the focal length of the collimating lens. Thus, a shift of the image position by 1 pixel corresponds to an angular displacement of $\Delta\theta = 7\,\mu\text{rad}$. Data acquisition and centroid determination is executed using LabVIEW (see Appendix C).

While the original version of the instrument involved evacuating the optical path between the light source and the focal lens to $\sim$1 Torr, subsequent tests revealed little difference in performance when this volume was left at atmospheric pressure as long as turbulence along the path was minimized. The decision to operate at atmospheric pressure alleviated the need to turn on a roughing pump every few days to maintain vacuum, while also allowing a spring-loaded adjustment system for the focal lens. This adjustment system replaced a cumbersome scheme for adjusting the focus of the autocollimator, making it much easier to obtain a well-focused image once the autocollimator was mounted to the experiment support frame.

The version of the autocollimator reported on in Cowsik et al. [5] used a cold-cathode flourescent lamp (CCFL) as the light source. The CCFL bulb provided a uniform illumination of the array of slits while maintaining a relatively stable temperature — desirable to minimize the possibility of thermal expansion of the optics plate of the instrument. A problem with the CCFL light source, however, was that the image returned to the autocollimator CCD camera was faint and thus determination of the image centroid position suffered from poor statistics after reflecting off of the 5.08 cm diameter mirrored test mass, and passing through the optical port and reflecting off the gimbal mirror twice (see Figure 4.1). Cowsik [5] showed that the angular resolution $\Delta\theta_{AC}$ of an autocollimator is set

by

$$\Delta\theta_{AC} = \frac{3\lambda/D}{N_0^{1/2}} \text{ rad Hz}^{-1/2} \tag{3.8}$$

where D is the diameter of the target mirror, λ is the wavelength of the light, and N_0 is the number of photons in the image collected per second. Thus the angular resolution improves as the square root of the number of photons detected.

Switching to a LED bulb allowed for a drastic improvement in light intensity, improving the performance of the instrument when installed on the experiment. A new optics plate, shown in Figure 3.6, was designed to illuminate the array of slits with a beam of light having the same f-number as the rest of the autocollimating optics. It was constructed to fit onto the existing autocollimator tube. To produce an image of approximately uniform intensity, a 3.4 V, 10 mm diameter LED bulb with an intensity of 100000 mcd illuminates a 25.4 mm diameter, 25.4 mm focal length condenser lens, then a 12.5 mm by 25 mm cylindrical collimating lens, before passing through an array of 50 slits and then the rest of the system as shown in Figure 3.5.

As shown in Figure 4.1, the auto-collimating optical lever (or autocollimator) is orientated vertically and a flat mirror held in a gimbal mount, oriented at a 45° angle with respect to the incoming autocollimator beam, redirects the light from the autocollimator through the chamber optical port where it reflects off the balance mirror, passes back through the optical port, off the gimbal mirror, and back into the autocollimator. The autocollimator and gimbal

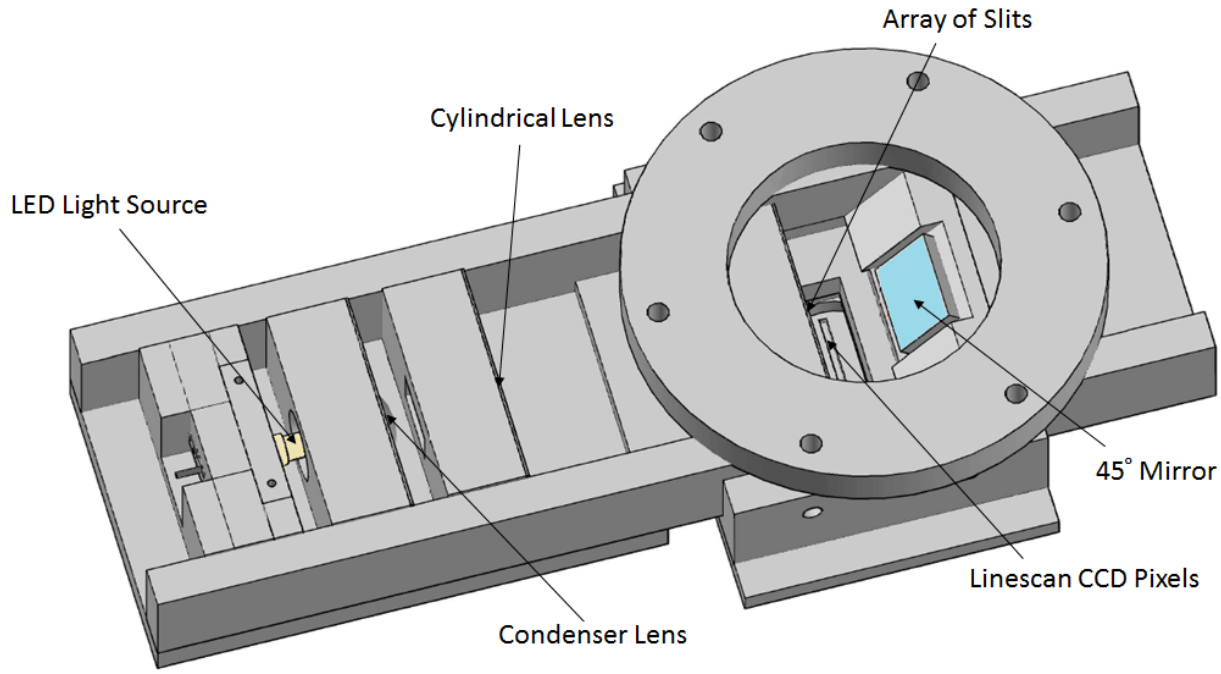

Figure 3.6: AutoCAD drawing of the autocollimator optics plate. The positions of the condenser lens and cylindrical are adjustable, as is the location of the 45° mirror which redirects the projected image down the autocollimtor tube (not shown). The camera, which is not visible other than the labeled CCD pixels, attaches to the underside of this plate. The array of slits is housed in the section between the cylindrical lens and the 45° mirror.

mirror are secured rigidly to the aluminum structure that supports the vacuum chamber. This arrangement reduces the footprint of the experiment, making it easier to thermally shield the apparatus (see § 4.4), and makes alignment of the optics a simple process, achieved by making adjustments to the gimbal mount.

3.2.2 Evaluating Low-Frequency Performance

The resolution of the autocollimator was evaluated by tracking the centroid position of the image produced by the instrument while viewing a stationary mirror. To reproduce experi-

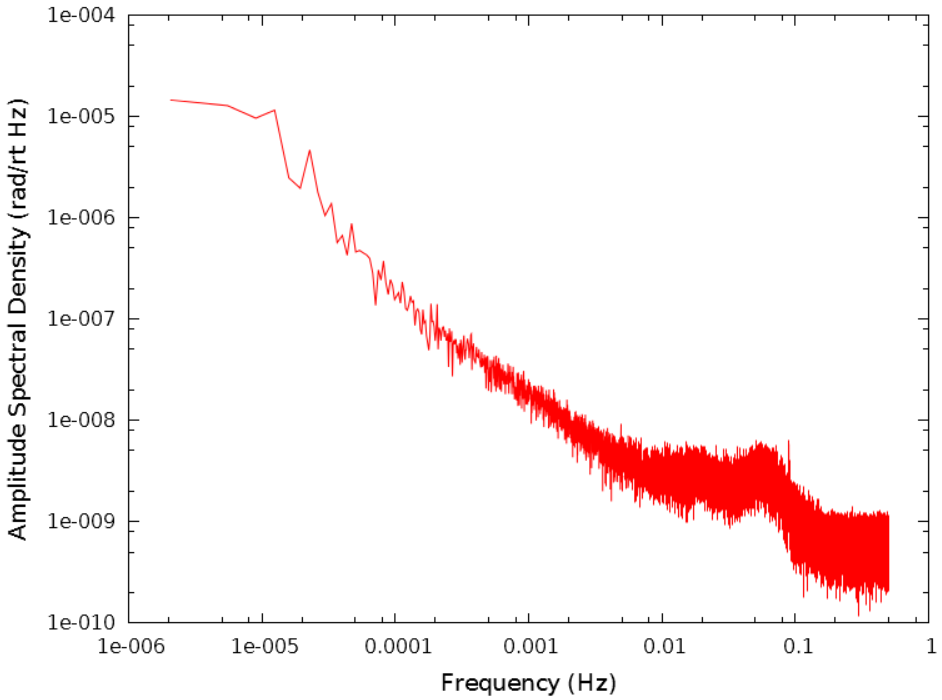

Figure 3.7: The angular spectral density of the signal obtained from observing a stationary mirror with the autocollimator on the floor of the Tyson bunker. An amplitude of $\sim 10^{-5}$ rad $\mathrm{Hz}^{-1/2}$ at the diurnal signal frequency $f_s = 1.157 \times 10^{-5}$ sets the limiting resolution of the instrument in terms of a measurement of an equivalence principle violation.

mental conditions, the autocollimator tests were performed at the remote laboratory at the Tyson Research Center where the torsion balance experiment is located. The autocollimator and mirror were covered with two insulating Styrofoam boxes which reduced noise due to thermal fluctuations and air currents along the exposed beam path. Multiple tests lasting several weeks were conducted, with the results evaluated using the spectral density of the autocollimator signal. The results of one such test are shown in Figure 3.7.

The amplitude of a periodic signal at frequency f with a quality factor of Q that can be detected with the instrument is given by

$$\theta_s \approx \Delta\theta_{AC} \left(\frac{f}{Q}\right)^{1/2} \tag{3.9}$$

where $\Delta\theta_{AC}$ denotes the amplitude of the spectral density of the autocollimator signal at frequency f. The diurnal signal expected from a violation of the equivalence principle has a very narrow bandwidth of $f_s/Q_s \approx 10^{-7}$ Hz, thus the autocollimator can measure such a signal with an amplitude of about a nanoradian.

3.3 Design and Operation of a Long-Period Torsion Balance

The majority of the work that went into these efforts has been the design and implementation of a torsion balance with an exceptionally low natural torsional frequency. The advantages gained by operating a balance with a long period include a reduction in $(f_0/f_s)^{1/2}$ in the Saulson noise at low frequencies, specifically the diurnal signal frequency for a equivalence principle violation. Furthermore, in order to be sensitive to the lowest of Earth's normal modes, at $\gtrsim 0.35\,\mathrm{mHz}$, the natural torsional frequency of the balance has to be significantly below these frequencies. In addition to designing such a balance, significant effort was put into characterizing its behavior and developing means to damp oscillations of the balance, from an amplitude of about a radian to a few µrad in a reasonably short amount of time.

While a detailed description of the torsion balance and related components is provided in Chapter 4, the thermal limits set for various models of damping are presented here, along with some considerations pertaining to the sensitivity of the balance to signals of interest as well as in regards to the geometric layout of the balance.

3.3.1 Torsion Balances

The torsion balance has been an invaluable tool for measuring minuscule forces for more than 200 years, and has found applications in a wide range of disciplines. Within the subfield of experimental gravitation, torsion balances are the instrument of choice for most experiments aiming to measure the gravitational constant, test the inverse square law, or search for violations of the equivalence principle. There are several key points worth noting as reasons why the torsion balance is particularly well suited for such applications.

- The torsion fiber from which the balance is suspended always hangs along the local vertical direction, thus naturally negating the effects of the Earth's gravitational field, $g_\oplus$. Modern laboratory tests of gravitation aim to measure accelerations that are more than 15 orders of magnitude smaller than $g_\oplus$, including the variations in the value of $g_\oplus$ itself due to tidal forces and other effects which can be as large as 0.0001% of $g_\oplus$ [70]. The extraordinary sensitivity of torsion balances may be attributed to the fact that they are sensitive only to forces acting in the plane perpendicular to the torsion fiber.

- In addition, a dipole torsion balance is only sensitive to forces that act on each of its

test masses differently. If each end of the balance is acted on by an identical force, the balance will exhibit no response. This offers a natural way to compare the forces acting on different materials far superior to making separate measurements of forces acting on each material.

- Another key characteristic of a torsion balance, is the extremely weak spring constant that the torsion fiber provides, allowing for the detection of even the weakest of forces. The fiber also provides a nearly frictionless system; the only losses coming from damping due to eddy currents, gas pressure, and internal friction in the fiber. By careful design of the experiment, and operating the balance in a vacuum chamber with a pressure maintained below $\sim 10^{-7}$ torr, losses due to the first two effects can be made negligible.

- And finally, the torsion balance is an instrument for which the sensitivity arises from its design rather than the machining tolerances in the mass and dimensions of the balance which can be much wider than the differential forces that the balance is capable of measuring. For these reasons, the torsion balance is the instrument of choice for many laboratory tests of gravity.

3.3.2 Thermal Noise Spectrum

The fundamental limit of any mechanical oscillator is set by thermal noise in the system. Any linear system in thermodynamic equilibrium can be modeled by the fluctuation-dissipation

theorem which was originally formulated by Nyquist in 1928 [71], with later work done by Callen and others [72, 73]. Saulson's derivation [74] of the thermal limit for low-dissipation oscillators is based on the fluctuation-dissipation theorem and is used widely for describing pendulum and torsion balance systems [3, 55, 75, 76]. Following his treatment, a torsion balance with moment of inertia I about the fiber which is acted on by thermal torque τ_{th}, is described by

$$\tau_{th} = I\ddot{\theta} + 2\beta\dot{\theta} + \kappa_f(1 + i\phi)\theta \tag{3.10}$$

where β is a coefficient accounting for velocity damping, and ϕ accounts for dissipation due to internal friction in the fiber.

By the fluctuation-dissipation theorem, the power spectrum of the minimal fluctuating torque acting on the balance is given by

$$\tau_{th}^2(\omega) = 4k_B T \Re(Z(\omega)) \tag{3.11}$$

where k_B is Boltzmann's constant, T is the absolute temperature, and $\Re(Z(\omega))$ is the real part of the mechanical impedance, given in the frequency domain by $Z(\omega) = \tau(\omega)/\dot{\theta}(\omega)$ as a measure of resistance to motion when subject to a harmonic force. The admittance $Y(\omega) \equiv Z^{-1}(\omega)$ can be used to give the power spectrum of the fluctuating motion in the system,

$$\theta_{th}^2(\omega) = \frac{k_B T}{\pi^2 \omega^2} \Re(Y(\omega)). \tag{3.12}$$

By applying Equation (3.12) to a torsion balance described by Equation (3.10) the fundamental limit of the balance can be obtained. Considering first the case where the balance is subject only to velocity damping, $\beta > 0$ and $\phi = 0$, the spectral density of the torque noise amplitude is given in terms of torque per root Hz as

$$\tau_{th}(\omega) = \sqrt{4 k_b T \frac{I \omega_0}{Q}} \tag{3.13}$$

where ω_0 is the natural frequency of torsional oscillations of the balance, and $Q_v = \omega_0 I / \beta$ is a measure of the dissipation at the resonant frequency. The amplitude spectral density is simply the square root of the power spectral density. Similarly, the amplitude spectral density of the thermal noise in the angular deflection for a velocity damped balance in terms of radians per root Hz is given by

$$\theta_{th,v}(\omega) = \left[\frac{4 k_b T}{Q_v I} \frac{\omega_0}{(\omega_0^2 - \omega^2)^2 + (\omega_0 \omega / Q)^2} \right]^{1/2}. \tag{3.14}$$

As Saulson notes, velocity damping of a torsion balance can be significantly reduced by operating the balance in high vacuum and by making use of magnetic shielding. Saulson and others have found that internal damping caused by losses due to internal friction in the fiber tends to dominate in a well designed torsion balance experiment. In the frequency domain, this damping is represented by $\phi(f)$, the degree of anelasticity in the fiber, or the angle by

which the balance response lags behind a sinusoidal driving torque (in radians). Based on past empirical studies of many materials, Saulson treats $\phi(f)$ as a frequency independent quantity.

Then, for pure internal damping, with $\beta = 0$ and $\phi > 0$, the impedance $Z(\omega)$ is found by replacing $\phi(t)$ with $\phi(\omega)e^{i\omega t}$ to give the equation of motion of the system in the frequency domain, and dividing by $\dot{\phi}(t) = i\omega\phi(\omega)e^{i\omega t}$. The mechanical admittance is found by taking the inverse of the impedance

$$Y(f) = \frac{\kappa_f\phi/2\pi f + i2\pi f I - i\kappa_f/2\pi f}{(\kappa_f\phi/2\pi f) + (\kappa_f/2\pi f - 2\pi f I)^2}. \tag{3.15}$$

The amplitude spectral density of thermal noise in the angular deflection of the balance with this admittance is then given by taking the square root of Equation (3.12)

$$\theta_{th,i}(\omega) = \left[\frac{4k_bT}{Q_i\omega I}\frac{\omega_0^2}{(\omega_0^2-\omega^2)^2 + (\omega_0^2/Q_i)^2}\right]^{1/2} \tag{3.16}$$

where $Q_i = \phi^{-1}$ for an internally damped oscillator. Thus when considering a signal $\omega_s << \omega$ with Q_s, the deflection (in radians) resulting from the thermal torque acting on the balance which limits the instrument's sensitivity to an equivalence principle violation can be estimated as

$$\theta_{min} = \theta_{th,i}\left(\frac{f_s}{Q_s}\right)^{1/2} \approx \left(\frac{4k_BT}{Q_i\omega I\omega_0^2}\right)^{1/2}\left(\frac{f_s}{Q_s}\right)^{1/2} \tag{3.17}$$

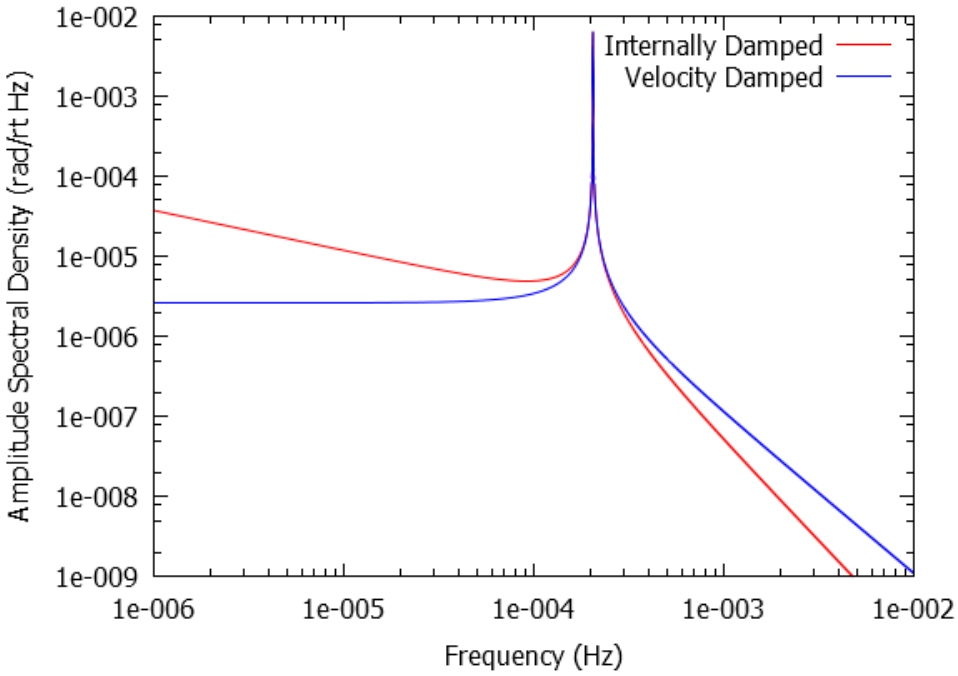

Figure 3.8: The amplitude spectral density of the thermal limits for the balance described in Chapter 4 in the case of damping due to internal dissipation of the fiber $\theta_{th,i}$ (in red) and velocity damping $\theta_{th,v}$ (in blue).

in the case of pure internal damping. For a balance measuring a signal $\omega_s << \omega$ subject to velocity damping, from Equation (3.14) this limit is given by

$$\theta_{min} = \theta_{th,v}\left(\frac{f_s}{Q_s}\right)^{1/2} \approx \left(\frac{4k_BT}{Q_v\omega_0^3 I}\right)^{1/2}\left(\frac{f_s}{Q_s}\right)^{1/2} \tag{3.18}$$

.

Thus $\theta_{th,v} \approx \sqrt{\omega_0/\omega}\theta_{th,p}$ indicating that for a balance with a longer period the thermal limit due to position damping will begin to approach the limit set by velocity damping.

Motivated in large part by the construction of suspension systems in large laser inter-

ferometers as well as attempts to explain discrepancies in experiments designed to measure the gravitational constant G, studies of the damping mechanisms for fibers in torsion balances and pendulums have been conducted with renewed interest within the past few decades [77–81]. Speake et al. have performed experimental and theoretical work to explain the low frequency losses for long-period pendulums. They note that their observations agree with an imaginary, frequency independent component of Young's modulus for Cu-Be fibers which could also be described by frequency dependent viscous damping, where the magnitude varies inversely with frequency. They conclude that "stick-slip" processes in the suspension systems and fibers of long-period pendulums can give rise to the losses they observed [80]. They also suggest that these processes are best modeled by considering a series of dashpots. DeSalvo proposes that low frequency noise in torsion balances is best explained via entanglement and disentanglement of dislocations in the fiber itself which result in a stochastic shift of equilibrium position of the balance. While the other models closely match the resulting $1/f$ noise spectrum at low frequencies, he suggests that a complete model of this behavior might be obtained using dislocation Self Organized Criticality statistics [81].

3.3.3 Scaling of Experiment Parameters

By considering expressions for the maximum deflection of the balance expected for an equivalence principle violation $\theta_s = \eta GMmrp/R^2$ from Equation (3.2), and the thermal noise floor at the signal frequency $\theta_{min} = [(4k_BTf_s)/(Q_i\omega I\omega_0^2 Q_s)]^{1/2}$, given by Equation (3.17) for a balance where the primary loses are due to internal damping in the fiber, the fundamental

level at which the experiment can search for violation of the equivalence principle is found by simply setting $\theta_s = \theta_{min}$ and solving for η.

$$\eta = \frac{\theta_{min}}{\theta_s} = \left(\frac{2k_BT}{\pi Q_i Q_s}\right)^{1/2} \left(\frac{R^2}{GM}\right) \left(\frac{1}{p}\right) \left(\frac{\kappa_f^{1/2}}{mr}\right) \tag{3.19}$$

.

Thus for a certain choice of fiber material and balance shape, the parameters that may be adjusted to reduce η are the torsion fiber constant κ_f, which scales as r_f^4/l_f, where r_f is the radius of the fiber and l_f is the fiber's length, and the mass m and radius r of the balance. This relationship goes as

$$\eta \propto \frac{r_f^2}{mrl_f^{1/2}} \tag{3.20}$$

.

This expression illustrates that a more massive balance improves the sensitivity of the experiment, however for a torsion fiber to support a larger mass, the radius of the fiber must be larger: a concession that reduces sensitivity. The relationship between the minimum radius r_{min} that a fiber can have while supporting some mass m_b is given by

$$r_{min}^2 = \frac{m_b g_\oplus}{\pi S} \tag{3.21}$$

.

where S is the tensile strength of the fiber. In practice, r_f is chosen to be larger than r_{min} to reduce the risk of breaking the fiber during the setup of the instrument.

The sensitivity of the experiment can be improved by increasing the radius of the balance, however, as explored in the following section, this may lead to increased systematic efforts due to local gravitational gradients. The length of the fiber may also be increased; while this provides addition experimental challenges, it does offer a promising way to reduce κ_f thus improving the sensitivity of the balance.

3.3.4 Insensitivity to Gravitational Gradients

Local gravitational gradients occurring at the diurnal signal frequency could potentially produce a false signal. The balance used in the experiment is cross-shaped, with cylindrical symmetry about the fiber axis and complete top-bottom symmetry about the horizontal plane through the suspended balance. Such a design significantly reduces sensitivity to non-uniform gravitational fields.

The torque detected by the balance, with density ρ_b, due to some source of a local gravitational gradient, with density ρ_s, can be modeled using multipole expansion. The gravitational potential V between the balance and the source is given by

$$V = -4\pi G \sum_{l=0}^{\infty} \frac{1}{2l+1} \sum_{m=-l}^{l} q_{lm} Q_{lm} \tag{3.22}$$

where the inner moments q_{lm} and outer fields Q_{lm} are given in terms of spherical har-

monics Y_l^m

$$Q_{lm} = \int \rho_s(\mathbf{r}') r'^{-(l+1)} Y_l^m(\hat{\mathbf{r}}') d^3 r' \tag{3.23}$$

$$q_{lm} = \int \rho_b(\mathbf{r}) r^l Y_l^{m*}(\hat{\mathbf{r}}) d^3 r. \tag{3.24}$$

As mentioned in § 3.3.3, it is clear that gravitational gradients are potentially more troublesome for a balance with large r. The resulting balance deflection is given by

$$\theta_g = \frac{\tau_g}{\kappa_f} = -\frac{1}{\kappa_f}\frac{\partial V}{\partial \phi} \tag{3.25}$$

where ϕ gives the angular orientation between the balance and source. Considering a ideal balance, only q_{00}, q_{40}, and q_{44} are non-zero. While $m = 0$ moments do not produce gravitational torques, if the suspended balance is tilted by some amount, these may become $m = 1$ moments. For a detailed discussion of the multipole formalism as it relates to torsion balance experiments see [53, 54].

The laboratory housing the experiment is completely undisturbed during data collection, thus barring some unforeseen phenomenon occurring outside the laboratory with significant gravitational influence and a diurnal frequency, the balance layout and specificity of the expected signal ensures that gravitational gradients are not a significant concern for the experiment.

Chapter 4

The Apparatus

A description of the major components of the prototype torsion balance instrument is presented in this chapter. In some instances, time and financial restrictions, or accessibility to superior engineering capabilities have limited the degree to which an ideal instrument could be built during the present effort. Where applicable, areas in which a future version of the experiment might be improved are noted.

A cross-shaped torsion balance is used, with the majority of the mass of the balance located in the four test masses at the ends of the cross. Comprised of two aluminum masses and two quartz glass masses, the balance forms a composition dipole. The balance is suspended from a fine torsion fiber inside of a vacuum chamber which rests on a rigid aluminum framework. The motion of the torsion balance is monitored through an optical port on the side of the chamber using the auto-collimating optical lever described in § 3.2. After an initial data run, the entire apparatus was surrounded by two layers of thermal shielding

to maintain thermal stability. The experiment is located in an underground bunker at the Tyson Research Center near Eureka, Missouri.

4.1 The Balance

Factors considered in the design of a balance searching for a violation of the equivalence principle as well as the normal mode oscillations of the Earth were discussed in the preceding chapters, however additional requirements are to be set for the materials chosen in the construction of the balance. The balance should be made of materials free of magnetic impurities so that time-varying magnetic fields do not produce a false signal. The balance operates in high vacuum, so component materials need to have low outgassing rates. Furthermore, in order to create a balance exhibiting a high degree of symmetry the test masses themselves should be as similar as possible in mass, shape, size, and their position from the center of the balance. To this end, materials with similar mass densities are required. As discussed in Chapter 2, certain theoretical considerations motivate the choice of materials most likely to produce an equivalence principle violation. Cost and machinability also factored into the decision to use aluminum (Al) and quartz glass (SiO_2) as the materials for the test masses.

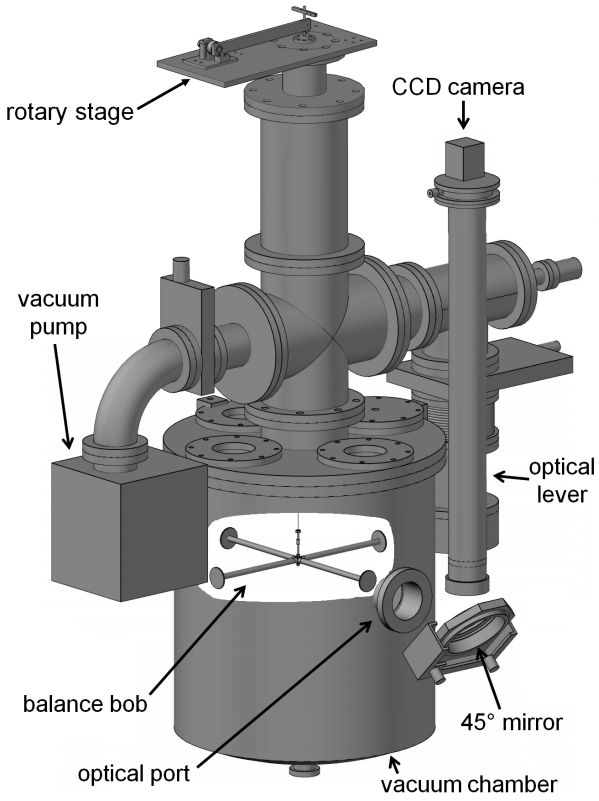

Figure 4.1: AutoCAD drawing illustrating key components of the experiment.

4.1.1 Construction of the Balance

To maximize the signal produced from a potential violation of the equivalence principle, the test masses of the balance should make up as much of the total mass of the balance as possible. Thus the rods supporting the four test masses, along with the center cross of the balance, were designed to contribute as little mass as possible while still having the capability of supporting the test masses. The 4-fold geometrically symmetric balance has a center piece which was constructed by removing notches from the center of two 3.17 cm long, 1.27 cm outer diameter hollow aluminum tubes, which fit together to create a cross. A hole was drilled through the top of this cross to accommodate the threaded rod which attaches the balance to the fiber. Four arms were attached to this center cross. Each arm was constructed from a strip of 0.008 cm thick aluminum foil, rolled into rods of length 24.00 ± 0.05 cm with a 1.27 cm inner diameter, with two holes punched approximately 4 cm from the outer end of each rod. The holes in each rod eliminate any chance of trapping air inside the arms of the completed balance which could cause an explosion of the aluminum tubes during evacuation of the vacuum chamber or collapse when the chamber is brought back to atmospheric pressure. Inserted into the outer ends of the balance arms are rings which includes a groove to increase the surface area available for bonding the test masses to the ends. All components of the balance were glued together using vacuum compatible Loctite Hysol epoxy.

The Al and SiO_2 test masses are disks with diameters of 5.08 cm and thicknesses of 0.3175

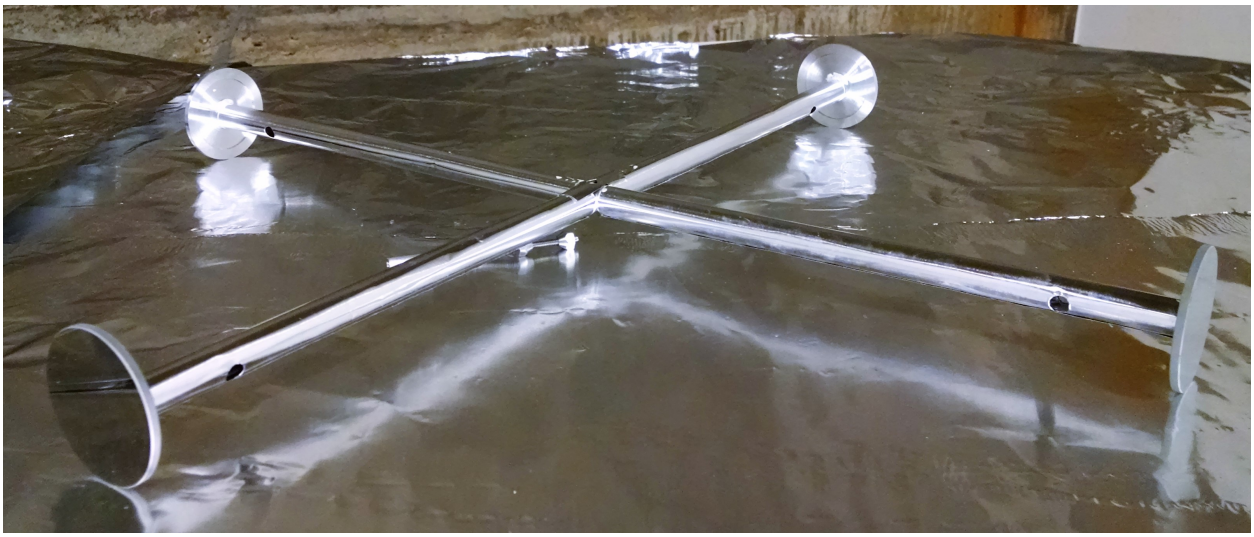

Figure 4.2: The balance before installation. The mirrored SiO_2 masses are in the foreground.

cm. Aluminum has a density of 2.70 g/cm^3, compared to 2.2 g/cm^3 for the SiO_2 masses, and to keep their mass equal, the Al masses were machined with a circular groove cut out of the inward facing side of each disk. Using vacuum deposition, the outward facing sides of the SiO_2 masses were coated with 1000 Å of Al to create a mirrored surface, to be viewed by the optical lever for measuring the angular orientation of the balance.

The Al test masses are made from an alloy, Al 1100, which was chosen for its high percentage of Al composition. Fearing magnetic contamination during the machining process, the atomic composition of a piece of the Al 1100 slab that the masses were machined from was analyzed by a scanning electron microscope. The results found a 99.6% atomic composition of Al, and $< 0.01\%$ composition of Fe. The SiO_2 test masses were used in the form purchased (other than the Al deposition) and were quoted to contain 99.995% SiO_2. The SiO_2 masses arrived ground and polished, and once mirrored produced an image far superior

to the image obtained when reflected off a $\lambda/4$ mirror.

Including the threaded rod assembly that attaches the balance to the fiber, the completed balance has a total mass of 75.1 ± 0.1 g, with each of the test masses contributing 14.32 ± 0.03 g. The balance has a moment of inertia about the fiber of approximately 3.85×10^4 g cm^2.

4.2 The Suspension System

The torsion balance is suspended by a system which includes a Picomotor-driven rotary stage that allows for adjustments of the angular orientation of the balance and for controlled damping of the torsional oscillations of the balance. An eddy current damping scheme precedes the fiber and reduces unwanted pendular swings of the balance.

4.2.1 Top Rotary Feedthrough

In order to align the balance with the chamber optical port and optical lever it is necessary to have the ability to manipulate the orientation of the balance, after the apparatus is assembled. In addition, well-timed adjustments of the balance equilibrium position are used to quickly damp the rotational oscillations of the balance by removing energy from the system. By adjusting the equilibrium position towards the position of the balance when it is at a turning point, oscillations of the balance can be suitably damped within a few periods of the balance — a process that would otherwise take months for such a high-Q oscillator.

A picture of the rotary stage is shown in Figure 4.4. Once the equilibrium position of

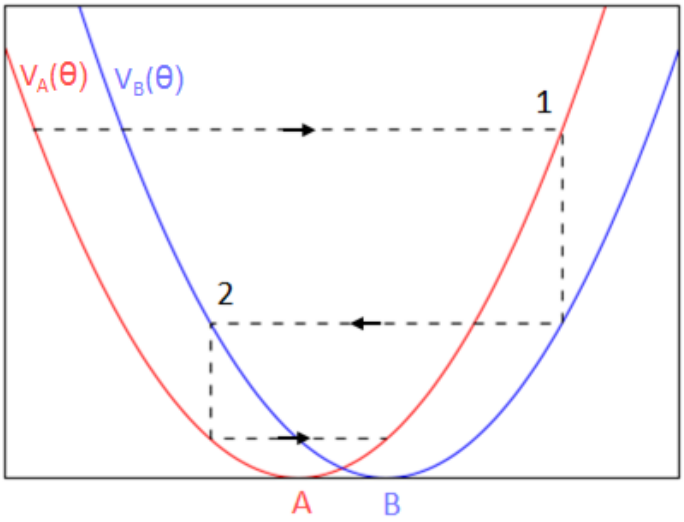

Figure 4.3: Illustration of the mechanical damping scheme to reduce the amplitude of torsional oscillations. When the balance reaches position 1, the 'zero' of the balance is shifted from position A to position B. When the balance reaches position 2, the 'zero' of the balance is shifted back to position A. This leads to a $2\,|A - B|$ reduction in amplitude.

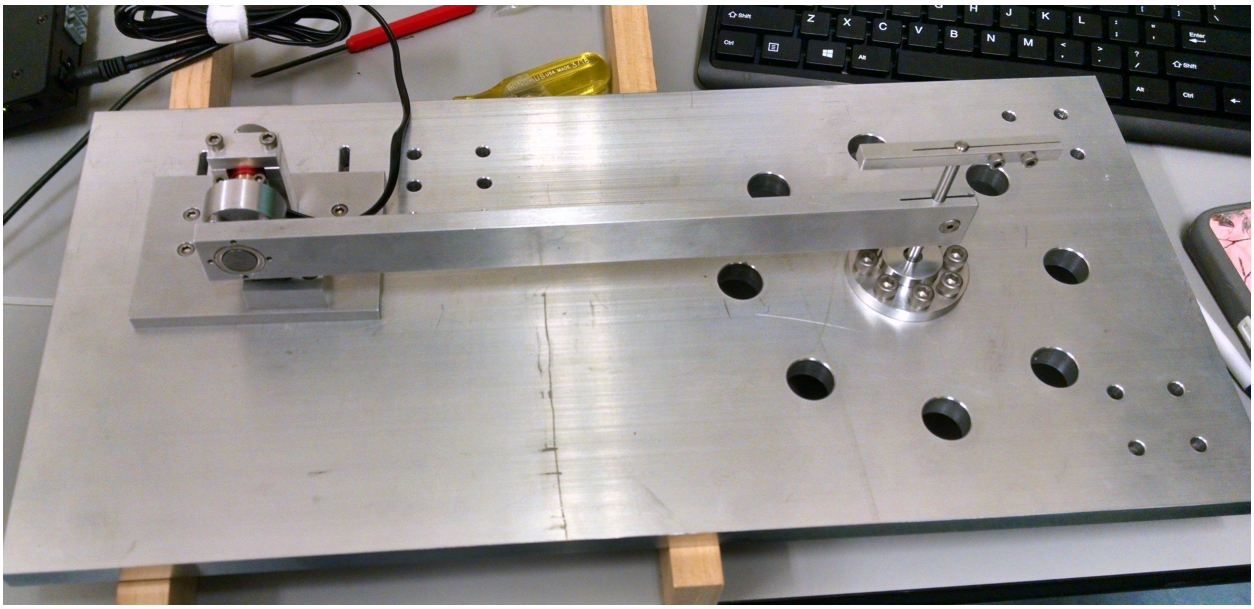

Figure 4.4: Top view of the Picomotor driven rotary feedthrough. The Picomotor actuator drives the left end of the bar which is clamped around a rod extending from the top of the rotary feedthrough. This bar is magnetically connected to the linear actuator. The eddy current damper described in § 4.2.2 attaches to the bottom of the rotational feedthrough.

the balance has been approximately centered on the optical port and the oscillations of the balance have been reduced to ∼0.02 rad, a bar which is driven on the opposite end by a Picomotor piezo linear actuator is clamped to a rod extending from the top of the rotary feedthrough. The 1.27 cm linear range of motion of the Picomotor corresponds to an angular range of about 0.05 rad, more than enough to control the balance once it has been roughly damped by hand. The Picomotor actuator is operated remotely through the data acquisition computer.

4.2.2 Eddy Current Damper

Attached to a rod extending from the bottom of the rotary feedthrough is an eddy current damping scheme which is designed to quickly reduce any pendular motion of the balance that can arise due to seismic or other disturbances. While mechanical modes such as pendulum swing, wobble, and bounce occur at very high frequencies compared to the torsional mode of the balance, these unwanted motions can feed energy into the torsional mode [66]. Early integrations of the instrument using a less effective approach for this damping mechanism showed that the pendular motion coupled to the torsional motion and produced an oscillation of the balance at the beat frequency and indicated the need for a more efficient damper. This phenomenon has been previously investigated by a group at the Huazhong University of Science and Technology [82, 83], and a model of this process is presented in Appendix A.

The first part of this damper is a tungsten fiber which is ∼8.5 cm long and 75 µm in diameter. Two aluminum pads clamp this "pre-hanger" fiber to a copper disk which is located

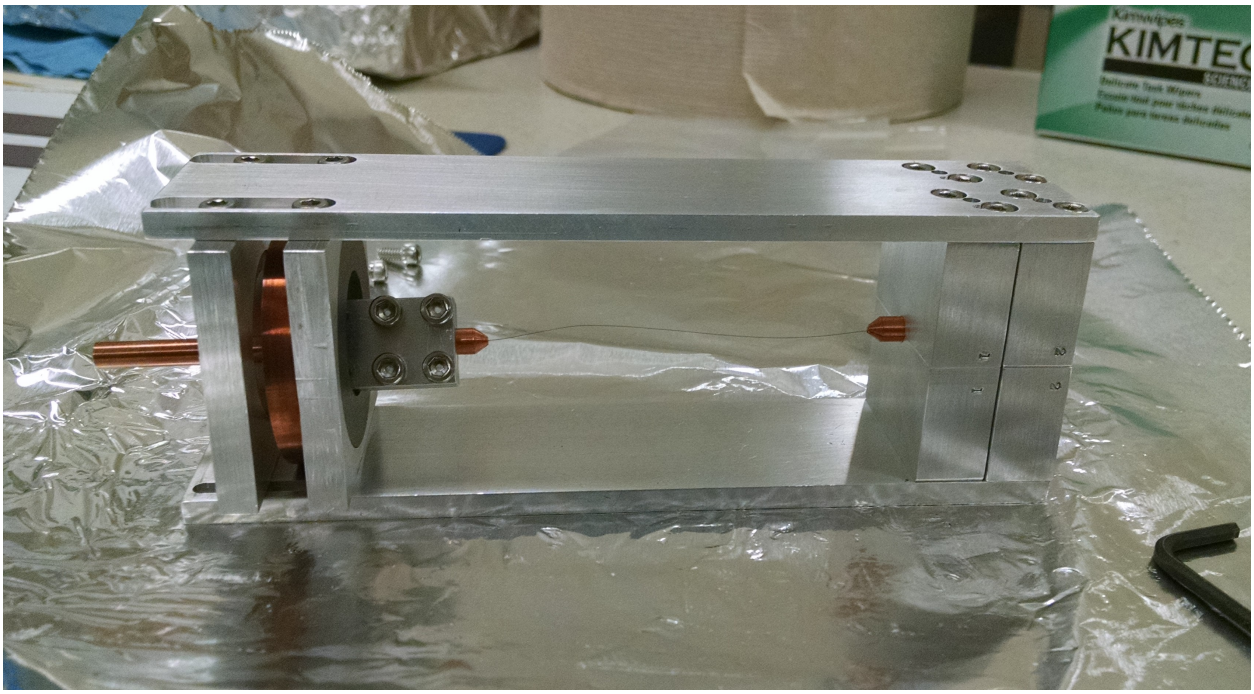

Figure 4.5: Pendular damper before installation, shown resting on its side. The pre-hanger is visible, clamped between copper bits. The ring magnets are held in place by aluminum holders which have the ability to be adjusted to accommodate the pre-hanger length. The top of the damper (on the right) attaches to the bottom of the rotary feedthrough; the torsion fiber (not shown) is clamped to the copper rod extending from the bottom of the damper (on the left).

between two ring magnets. The plane of the copper disk is perpendicular to the magnetic field lines between the magnets such that pendular oscillations of the fiber will generate eddy currents in the copper disk. As these eddy currents are dissipated the pendular motion of the balance is damped, while the axial symmetry of the system allows torsional oscillations to endure. This pre-hanger also ensures that the main torsion fiber is aligned with the local gravitational field, while the circular cross section of the pre-hanger significantly reduces the effects of ground tilts on the angular deflection of the balance [5, 66, 84].

4.2.3 The Fiber

Clamped to the bottom of the pendular damper is the torsion fiber. The fiber is made of tungsten, is 98 cm long, and has a circular cross section of diameter 25 µm. The torsion constant, κ_f, of a fiber of circular cross section is given by

$$\kappa_f = \frac{\pi \mu r^4}{2l} \tag{4.1}$$

where μ is the modulus of rigidity of the fiber material (1.61×10^{12} g cm^{-1} s^{-2} for tungsten), r is the cross-sectional radius of the fiber, and l is its length. With these values the torsion constant is $\kappa_f = 6.3 \times 10^{-2}$ dyne cm rad^{-1}. The natural period of torsional oscillations is $T = 2\pi\sqrt{I/\kappa_f} \approx 81$ min for the prototype balance. The maximum load this fiber could support was determined to be about 120 g. In an effort to prevent the fiber from breaking during the process of closing the vacuum chamber a limit of about 80 g was placed on the mass of the balance.

When a new fiber was installed, the balance exhibited random twists sporadically, as internal stresses in the fiber were relieved. In addition, torsion fibers exhibit a fairly constant drift, causing the equilibrium position of the balance to continuously move, generally at a rate of $\sim 1 \times 10^{-4}$ rad/day. This drift presents a challenge during data analysis, and limits the amount of time the balance can be viewed without adjusting the optical lever alignment. It is standard procedure to hang fibers supporting a small amount of mass ahead of integration, or

to apply a current to heat them, to anneal out these mechanical stresses ahead of integration of the experiment; however, previous attempts at annealing fibers have not shown significant improvement in the quality of the fiber [85], thus no annealing was undertaken in setting up the prototype balance.

The process of installing a fiber involved threading the fiber through a series of holes in an aluminum block which was clamped tight around a rod extending from the copper disk of the pendular damper. The bottom end of the fiber was clamped between two aluminum bits which fit into the end of a threaded rod, with a nut to secure the aluminum bits. The fiber was then lowered through the top of the chamber, with great caution taken to avoid introducing any kinks in the fiber which would compromise its ability to support the balance. Once the fiber was in place, the balance was attached by passing the threaded rod at the end of the fiber through the hole in the center of the balance, with a nut tightened below it.

4.3 The Vacuum System

To reduce noise due to collisions with air molecules and the effects of radiometric winds, the torsion balance is housed inside a vacuum chamber operating at about 10^{-8} torr. The chamber consists of an upper cross-shaped section, with the rotary stage and pendular damper at the top, a turbomolecular pump and an ion pump attached to the sides, and the large bell jar section where the torsion balance itself is located at the bottom (see Figure 4.1). The bell jar has a diameter of about 60 cm, height of about 75 cm, and includes

a 15 cm diameter side optical port which allows the position of the balance to be monitored with an optical lever. The bell jar also houses a mesh platform that was installed as a safety net for the delicate balance in the case that the torsion fiber were to snap. The bell jar is clamped to a large flange which is attached to the rest of the vacuum chamber. The entire chamber rests on a sturdy framework built from a t-slotted aluminum frame.

The process of pumping on the chamber is started by evacuating the chamber to rough vacuum using an Edwards XDS dry pump. This scroll pump is attached to the chamber by vacuum bellows which is eventually removed during data collection. An Osaka Vacuum turbomolecular pump, which is backed by the scroll pump, is then switched on, bringing the chamber pressure down to about 10^{-8} torr. Generally theses two pumps are left on for a few days before the VacIon Starcell Ion Pump is switched on to maintain a pressure of about 10^{-8} torr. While the turbomolecular and scroll pumps have moving parts which introduce vibrational noise into the system, the ion pump maintains vacuum by ionizing the gas within the chamber and using an electric potential to capture the ionized particles, thus it lends itself well to sensitive experiments such as those involving torsion balances.

4.3.1 Glitches

Upon first observing the freely hanging balance, semi-periodic jolts to the balance, which were termed "glitches", were observed, occurring every several hours. For a time it was thought that the glitches were caused by some local event, such as a switch in the nearby Metrolink power grid, or by the sporadic emission of charged particles from the ion pump.

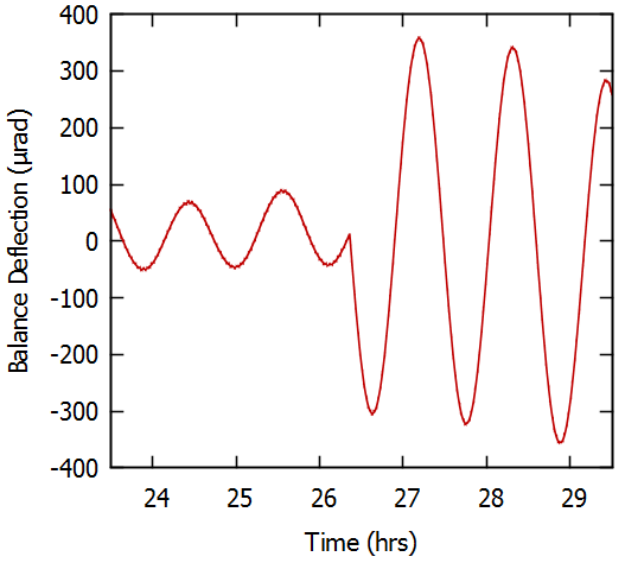

Figure 4.6: At $t = 26.3$ hrs a glitch occurs, drastically altering the amplitude and phase of the oscillation of the balance.

However, after the glitches persisted upon moving the experiment to the Tyson Research Center bunker and adding a grounded mesh screen between the ion pump and the rest of the vacuum chamber, it was discovered that these events corresponded to spikes in the ion pump current (monitored to track the pressure in the chamber) and were the result of sudden pressure bursts at different o-ring seals. A proposed explanation is as follows: a small leak fills a bubble of vacuum grease which eventually bursts, releasing the trapped gas and causing a transient jump in the measured vacuum pressure. The process repeats as the leak creates another bubble [86]. The same kind of behavior was observed in torsion balance tests of the gravitational inverse-square law and the equivalence principle test performed by the Eöt-Wash group [55, 87].

The current spikes occur with different magnitudes, and only spikes around a certain

magnitude have an obvious affect on the torsion balance. This seems to suggest that the pressure bursts occur at multiple o-ring seals, however only bursts at one specific seal have a significant effect on the balance. This seal was identified as the o-ring at the chamber optical port; after removing most of the vacuum grease on this o-ring and replacing the seal a significant decrease in the magnitude and frequency of glitches was immediately observed. Rather than occurring every several hours, glitches occur every few weeks - a frequency low enough to carry out a search for a diurnal signal. While attempts to find the locations of other seals emitting pressure bursts were largely unsuccessful, these were not deemed as critical based on the lack of noticeable response of the balance. Ideally, a chamber without rubber o-ring seals would be used.

4.4 Thermal Shielding

The importance of achieving a high level of thermal stability in this experiment cannot be overstated. Temperature variations cause expansion and contraction across many parts of the experiment; the autocollimator is affected by thermal fluctuations, the drift of the fiber is temperature dependent, the aluminum support structure may undergo minuscule shifts, and the curvature of the mirrors used for position readout may be affected. Of particular concern, is the fact that the diurnal temperature cycle occurs at exactly the frequency of interest for a possible violation of the equivalence principle. It is likely that the ability to maintain a constant temperature will be the limiting factor on the sensitivity of the experiment. The

benefits of an underground laboratory in terms of thermal stability will be discussed § 4.6, however, after an initial data run where a diurnal variation of ∼7 mK was measured in the laboratory, additional measures were employed to reduce temperature variation.

The effectiveness of passive temperature control can be estimated by solving the heat diffusion equation. Considering a semi-infinite sheet of insulating material lying in the yz-plane with thermal conductivity k, density ρ, and heat capacity c, subject to surface temperature variations given by

$$T(x=0,t) = A_0 e^{i\omega t} \tag{4.2}$$

it is straightforward to show that the temperature T at a depth x is given by

$$T(x,t) = A_0 e^{-\sqrt{\omega/2\alpha}x} e^{i(\omega t - \sqrt{\omega/2\alpha}x)} \tag{4.3}$$

where A_0 is the amplitude of the periodic variation, ω is the frequency of the variation, and $\alpha = k/\rho c$ is the thermal diffusivity of the insulating material. Thus the insulation reduces the amplitude of the thermal wave by a factor of $e^{-\sqrt{\omega/2\alpha}x}$ while also introducing a frequency dependent phase shift which increases with depth.

4.4.1 The Insulating Enclosure

To provide this additional improvement in thermal stability, two layers of insulation were built around the assembled apparatus from 2 inch thick FOAMULAR Extruded Polystyrene Rigid Foam panels. The inner layer is attached to a wooden 2x4 frame and closely encompasses the entirety of the apparatus and aluminum support frame without coming in contact with either the apparatus or the support frame. The outer layer stands freely, not contacting the first layer of insulation at any point. Joints in the extruded polystyrene sheets were sealed with a polyurethane-based insulating foam sealant and duct tape. In addition, the space beneath the chamber within the support frame was filled with rolls of fiberglass insulation, providing additional insulation and reducing air currents within the insulating structure.

From Equation (4.3), using values of κ, ρ, and c for $\sim$5 cm of extruded polystyrene, it can be shown that the thermal shielding reduces a diurnal temperature wave in the laboratory to about 40% of its initial amplitude.

4.4.2 Temperature Sensors

The temperature inside the thermal shielding was monitored by four negative temperature coefficient thermistors (Measurement Specialties, model no. 55016) located at each corner of the aluminum support frame. The resistance of a thermistor changes with temperature, and this relationship can be modeled using the Steinhart-Hart equation

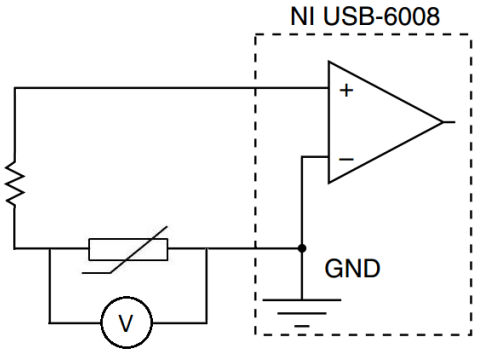

Figure 4.7: Circuit diagram of a single temperature sensor. The NI USB-6008 DAQ provides +5 V and a reference ground, and also measures the voltage across the thermistor.

$$\frac{1}{T} = A + B\ln(R) + C[\ln(R)]^3 \tag{4.4}$$

where T is the temperature in Kelvins, R is the resistance in ohms, and A, B, and C are coefficients which depend on the thermistor. At a temperature of 25 °C these glass thermistors have a reported resistance of 10 kΩ.

Each thermistor was enclosed in a aluminum casing to increase the thermal inertia of the sensor, and was wired in series with a 10 kΩ resistor. A National Instruments USB-6008 DAQ device was used to power each of the circuits and to measure the voltage on either side of the thermistor. These voltage readings are used to determine how the thermistors' resistance changes with time. By averaging the temperature recorded by a single thermistor over 100 seconds, a precision of better than 0.002 K is measured.

Figure 4.8: The mu-metal magnetic shielding and support structure. The mirrored SiO_2 test mass used to monitor the position of the balance can be seen in the open end of the shielding tube.

4.5 Magnetic Shielding

A serious concern during the operation of any sensitive torsion balance experiment of this type is the possibility of a time-varying magnetic field affecting the motion of the balance. While the balance was built from non-magnetic materials, and the test masses were tested for ferromagnetic contamination after the machining process, it is often noted that the torsion balance itself is the most sensitive means for testing the magnetic contamination of its components. For this reason, passive magnetic shielding is typically used to reduce the magnetic forces acting on the balance.

This is generally accomplished by surrounding the balance with one or more layers of a high permeability material, providing a low reluctance path for magnetic flux and reducing the magnetic field inside the shielded volume. Due to the large size of the vacuum chamber housing the balance, and the high cost of shielding material, a magnetic shield made from high permeability mu-metal sheets supported by an aluminum frame was designed and constructed to fit neatly around the balance rather than enclosing the entire chamber. This shielding (shown in Figure 4.8) is in the shape of a box, with four protruding tubes that enclose the balance arms. The ends of three of the tubes are covered with mu-metal caps, while the uncovered end faces the optical port to allow the optical lever to monitor the balance. There is a hole in the top of the shielding for the torsion fiber. The shielding was constructed around the balance, then attached to a support frame which attached to the top flange of the vacuum chamber bell jar. Once in place, the balance was attached to the torsion fiber.

After attempting to collect data for a few months with the magnetic shielding in place it became clear that the balance was strongly attracted to the shielding. Damping and centering the balance in the field of view of the optical lever was nearly impossible as the balance always seemed to twist immediately towards one side or the other of the arms of the magnetic shielding. Approximately two weeks of data were obtained in which the torsional period of the balance varied between $\sim$115 min and $\sim$125 min, much longer than the expected 81 min period, indicating the influence of a strong external force.

This attraction was likely due to electrostatic charge build up on the balance, shield-

ing, or both, or magnetic contamination. Typically electrostatic coupling is avoided by gold coating the balance and nearby surfaces. As this was not feasible with the available deposition system, the decision was made to run the prototype instrument without the mu-metal shielding. A next generation version of the instrument should include one or more layers of magnetic shielding, as well as a means for preventing electrostatic attraction between the balance and nearby surfaces. This may be accomplished by gold coating the balance; alternatively, ultraviolet LEDs have been shown to effectively remove built up charge in torsion balance experiments via the photoelectric effect [88].

4.6 The Laboratory at the Tyson Research Center

Following a period of testing the apparatus for proof of concept in our basement laboratory on the campus of Washington University, the experiment was relocated to an empty bunker built partially into a hillside at the Tyson Research Center, about 20 miles southwest of campus. Originally built to store ammunition during World War II, the bunker offers favorable conditions for this type of sensitive experiment on two fronts. Due in large part to its relative isolation, the Tyson bunker is a seismically quiet site. The bunker is located about a mile from the nearest major road, and 50 feet from a lightly traveled service road. Data collected with our robust rotational seismometer indicates that the bunker is subject to less seismic noise than both the campus laboratory and a seismic isolation vault at the Sandia National Laboratory in Albuquerque, New Mexico — considered a quiet site. Furthermore,

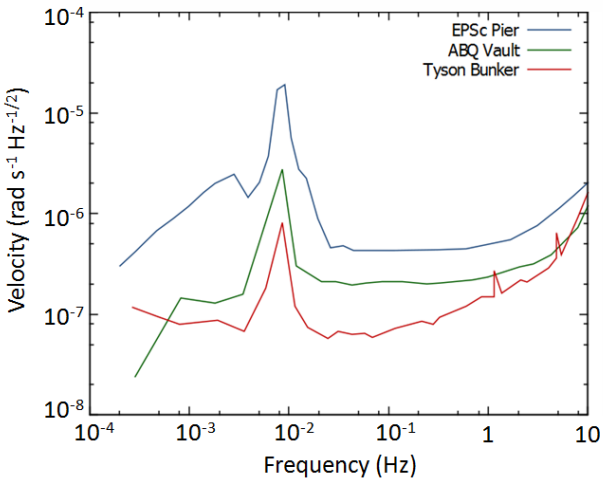

Figure 4.9: Robust rotational seismometer data taken in the Tyson bunker laboratory indicate seismically quiet conditions.

the cover of earth and thick concrete ceiling, walls, and floor provide a natural reduction in temperature variability, even before taking additional measures to maintain thermal stability. Measurements of the internal temperature of the bunker show a diurnal temperature swing of only several mK.

The isolation of the experiment also reduces the risk of time varying gravitational gradients. Once an experimental run is started there is no need to enter the bunker, with the exception of adjusting the gimbal mirror when the drift of the fiber takes the image reflected from the balance near the edge of the imaging CCD. The bunker is wired with an internet connection, and complete control over the data acquisition computer is achieved using TeamViewer software. This also allows for the damping of the balance's torsional oscillations using the Picomotor driven top rotary stage to be done remotely.

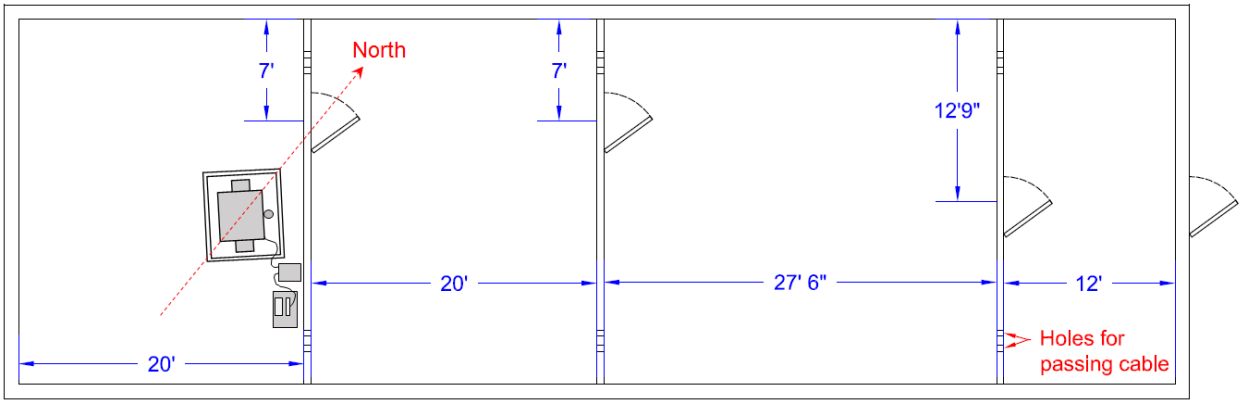

Figure 4.10: Floor plan of the Tyson Bunker. The experiment is located in the room farthest from the entrance to the bunker. The approximate size, location, and orientation of the experiment, electronics rack, and computer used for data collection is shown. True geodetic north is also shown with respect to the experiment. The bunker is a semicylinder; the top of the bunker reaches a height of 12.75' at its center, sloping to the floor at the sides of the room. Not illustrated in the floor plan are various workstations and some robust rotational seismometers (see [5, 6]) which are set up in the other rooms.

Figure 4.11: Outside view of the bunker. Entrance is just to the right of the Jeep, the bunker extends to the right.

Chapter 5

Studies of the Laboratory Environment and the Performance of the Instrument

By April 2014 the instrument had been fully integrated and was running in the campus laboratory at Washington University. At this point, a balance with test masses of 10.4 g was in use, as well as a manual rotational feedthrough at the top of the fiber suspension. During the approximately two months that the torsion balance was in operation in the campus laboratory, the glitch issue discussed in § 4.3.1 was first discovered, and the need for a mechanical torsional damping scheme allowing the remote control of fine adjustments was illuminated. In addition, based on the response of the balance to a strong magnet placed near the outside of the vacuum chamber, it was suspected that this initial balance

was magnetically contaminated.

In August 2014 the entire experiment was disassembled and relocated to the underground bunker at the Tyson Research Center. When rebuilding the instrument, the Picomotor-driven top rotary feedthrough discussed in § 4.2.1 was installed without the eddy current pendular damping scheme described in § 4.2.2 (the resulting coupled modes from this arrangement are discussed in Appendix A). A new balance was also installed; in order to reduce the mass of the non-test mass components of the balance the center cross was redesigned, resulting in a balance with a total mass of $\sim$52 g. From September 2014 to April 2015 the instrument was run at Tyson. During this time, the glitch issue was successfully reduced. During June, July, and August of 2015 a new pendular damping scheme was installed, along with a new balance (as described in § 4.1) and the magnetic shielding described in § 4.5. After discovering the attraction issues with the magnetic shielding and removing this shielding, the prototype instrument was finally set up for a lengthy data run which started on October 26, 2015.

All of the data presented in this chapter were obtained during two data runs in this final configuration, the first, which will be referred to as the Fall 2015 data run, spanned 56 days from October 28 to December 23, 2015. After adding thermal insulation around the experiment, a second data run (Winter 2016 data run) was conducted from February 27 to March 23, 2016. Balance position, temperature at four locations around the experiment, and the vacuum chamber pressure were all monitored throughout periods of data collection. The analysis that follows is meant to characterize both the instrument and the laboratory;

the general approach is illustrated, providing confidence that some straightforward upgrades, which are outlined in Chapter 7, will allow a next generation version of the instrument to surpass the sensitivities of current efforts to test the equivalence principle.

5.1 Collection of Data

The Fall 2015 data run is comprised of 5 data files, given in Table 5.1. These files are essentially continuous, with small gaps of only a few minutes between files. The files include time and centroid position (corresponding to the balance orientation); for this data run, time stamps were adjusted so that $t = 0$ corresponds to 00:00:00 CDT on October 26, 2015. The temperature of four thermistors and pressure in the chamber were recorded as well, as separate files. The position of the balance for each of these data files is plotted in Figures 5.1 to 5.5 shown in terms of pixels of the autocollimator CCD, and in radians from the initial position. In some places, the amplitude of the balance increases by some (usually small) amount. This is generally caused by a pressure burst at one of the vacuum seals (a glitch). In some cases, a seismic event will also add significant energy into the system, raising the amplitude of the torsional oscillations. Several times during this data run, the equilibrium position of the balance would shift suddenly. It is suspected that this is caused by the sudden slippage of some part of the suspension, most likely at the attachment point of the torsion fiber. Referred to as a 'stick-slip' process, these could be corrected for during most of the analysis approaches shown in this chapter. And finally, twice during the Fall 2015

File Name	*Start Date*	*Start Time*	*Time Shift*
EQPtest_26Oct2015b.txt	26 Oct 2015	13:23:05.8	t + 48185.8 s
EQPtest_12Nov2015.txt	12 Nov 2015	09:30:53.4	t + 1506653.4 s
EQPtest_20Nov2015edit.txt	20 Nov 2015	09:24:00.0	t + 2197440.1 s
EQPtest_3Dec2015.txt	3 Dec 2015	13:00:20.7	t + 3333620.7 s
EQPtest_17Dec2015.txt	17 Dec 2015	15:04:13.9	t + 4550654.0 s

Table 5.1: Five data files that constitute the ∼2 month Fall 2015 data run.

data run the orientation of the gimbal mirror was adjusted as the drift of the fiber brought the image reflected off the balance near the edge of the autocollimator CCD. This is seen in Figure 5.1 and Figure 5.4 as a large shift in the equilibrium position towards a higher CCD pixel number. Following these adjustments, the balance was damped remotely to reduce the amplitude of torsional oscillations.

Jumps and short discontinuities in the data run caused by a shift of the equilibrium position, or a break between data sets were removed by fitting segments of a few hours immediately before or after the anomaly in the data to a sinusoidal function with a linear drift of the form

$$\theta(t) = a_1 + a_2 t + a_3 \sin(a_4 t + a_5), \tag{5.1}$$

where constants a_1, a_2, a_3, a_4, and a_5 were parameters fit using the curve fitting tool in MATLAB. This fit was then used to extrapolate balance position to create a smooth data set. The result of the combined data sets for the Fall 2015 data run is shown in red in Figure 5.6.

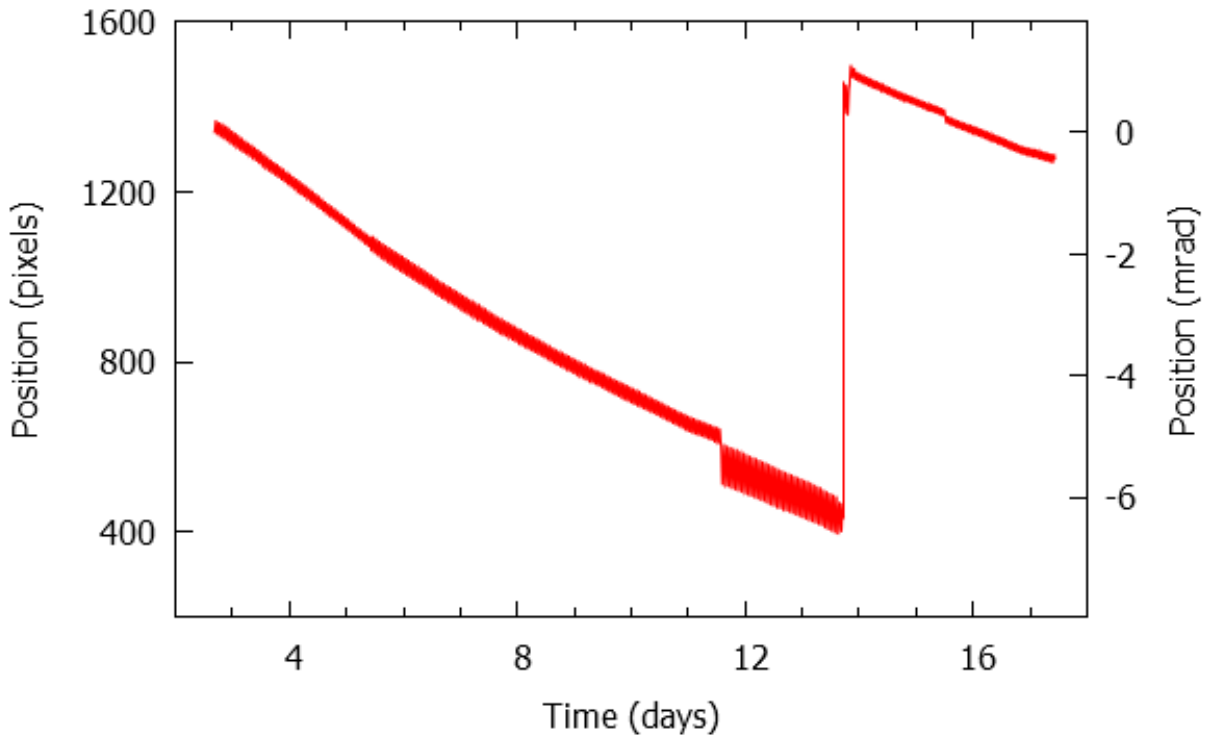

Figure 5.1: Balance position for data file EQPtest_26Oct2015b.txt given in terms of autocollimator CCD pixels and radians from initial position. Near t = 5.5 days a pressure burst occurred which increased the amplitude of torsional oscillations. Near $t = 11.5$ days and $t = 15.5$ days the equilibrium position of the balances shifts suddenly. At about $t = 13.7$ days the gimbal mirror was adjusted manually and the balance was then damped remotely.

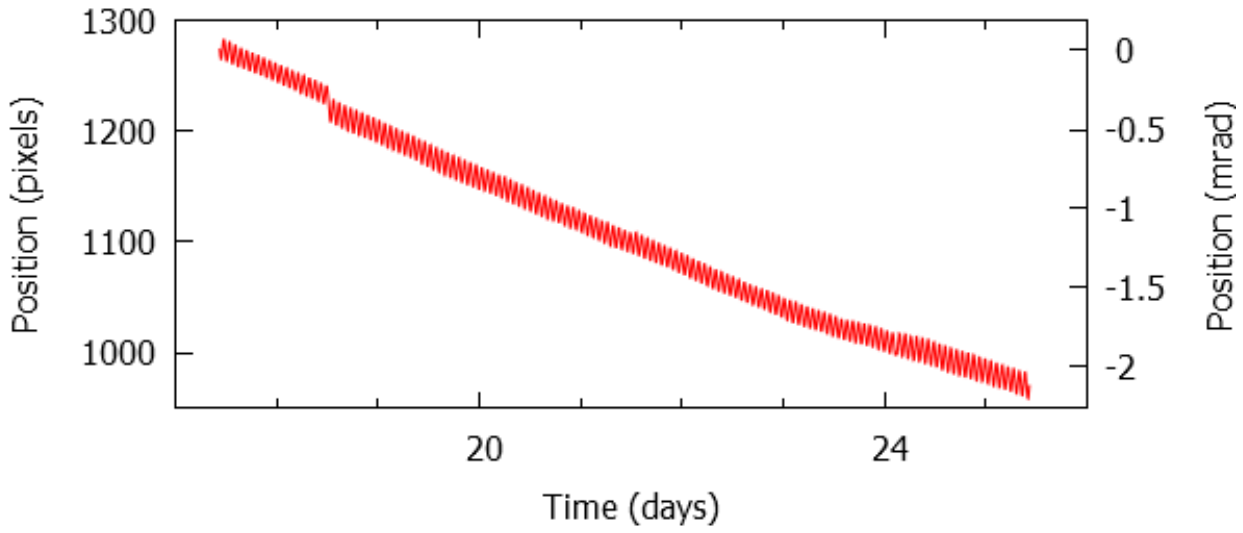

Figure 5.2: Position data for EQPtest_12Nov2015.txt. Shift of the equilibrium position of the balance occurs at $t \approx 18.5$ days.

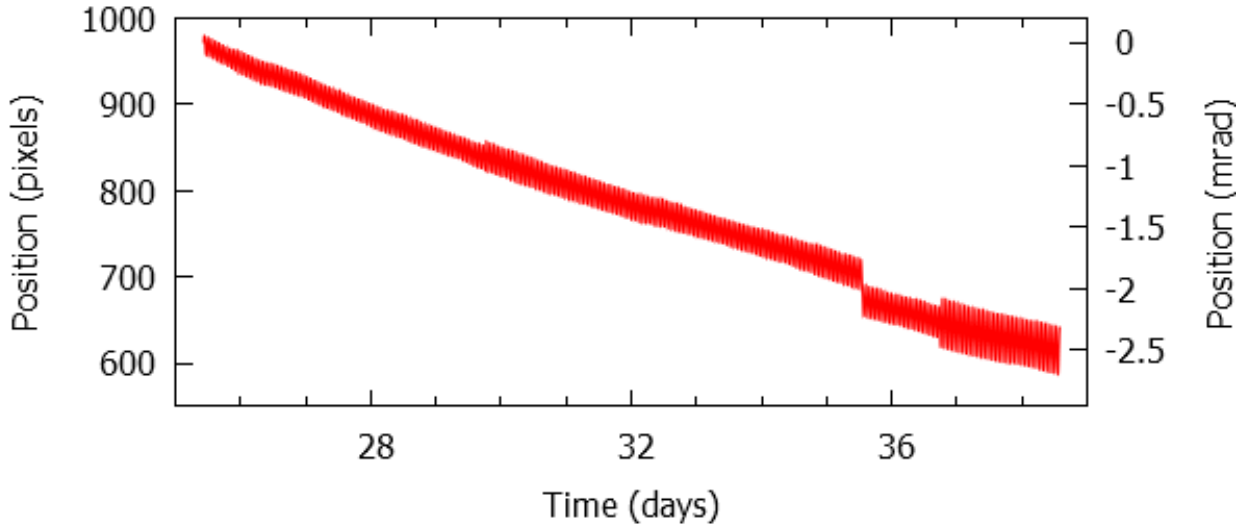

Figure 5.3: Position data for EQPtest_20Nov2015edit.txt. At $t \approx 29.8$ days a large earthquake in South America excited the balance feeding energy into the torsional oscillations (see § 6.3). At $t \approx 35.5$ days a shift in the equilibrium position occurred, and at $t \approx 36.7$ days a pressure burst excited the balance.

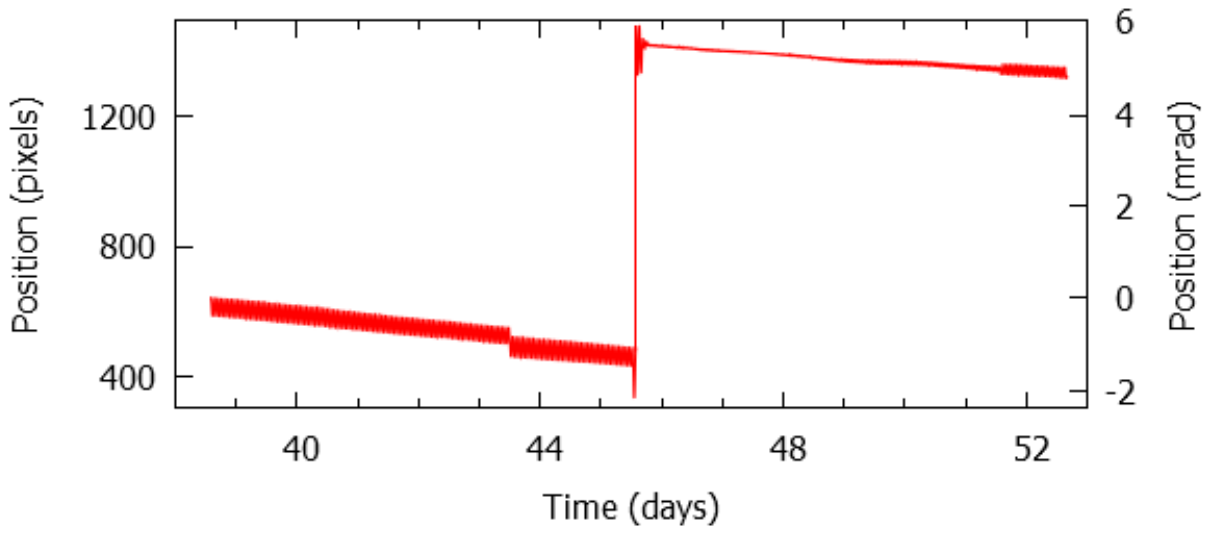

Figure 5.4: Position data for EQPtest_3Dec2015.txt. The equilibrium position of the balance is shifted at $t \approx 43.5$ days, the gimbal mirror was adjusted at $t \approx 45.6$ days, and a pressure burst occurred at $t \approx 51.6$ days. From $t = 46$ to $t = 48.5$ days the amplitude of the balance was damped to < 15 μrad.

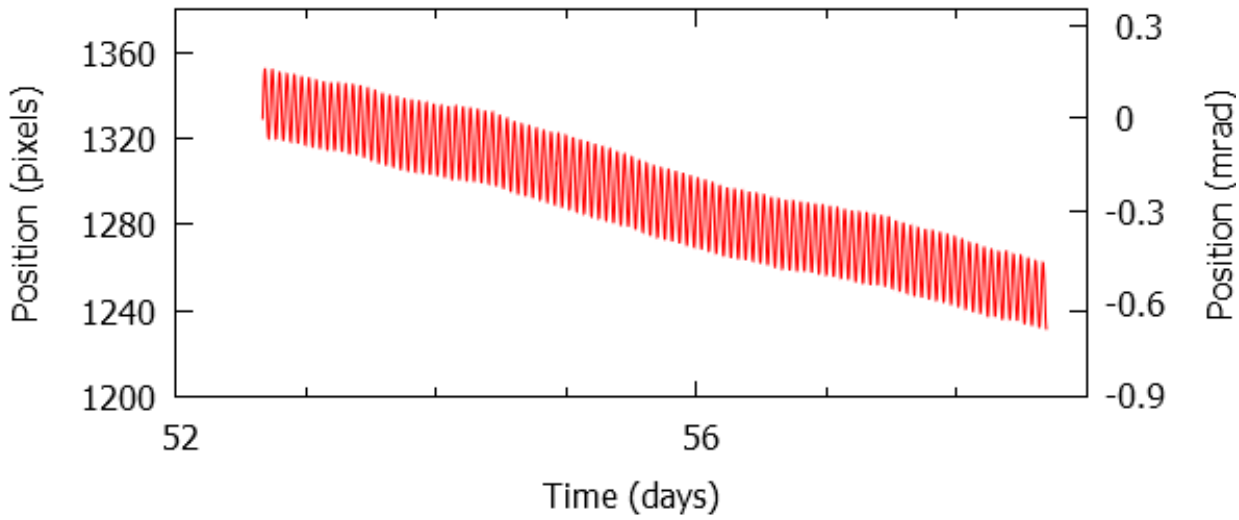

Figure 5.5: Position data for EQPtest_17Dec2015.txt. The end of this run coincided with a power outage caused by flooding in the St. Louis area.

Next the torsional oscillations of the balance were filtered out of the data by simply averaging points half a period apart by the following relationship

$$\theta_{fil}(t) = \frac{1}{2}\left[\theta\left(t - \frac{T_0}{4}\right) + \theta\left(t + \frac{T_0}{4}\right)\right]. \tag{5.2}$$

Here $T_0 = 4867.6$ s gives the torsion period of the balance which is determined from the Fourier transform of the position data. The filtering program searched for the points closest to $t - T_0/4$ and $t + T_0/4$ for each value of t. The combined data sets after the torsional oscillations have been filtered is shown in blue in Figure 5.6, and a enlarged plot of balance position and equilibrium position (torsional oscillations removed) is shown in Figure 5.7. After filtering the data, the effects of pressure bursts on the balance are particularly clear. As illustrated in Figure 5.7, the equilibrium position of the balance is briefly disturbed before returning to roughly its original location. This occurs to varying degrees both for bursts that seem to obviously affect the motion of the balance, as well as for bursts where the effect is not obvious while viewing the raw balance position data. This illustrates the reduction of noise in the balance position that may be achieved by replacing the rubber o-rings with metal seals in a future instrument.

5.2 Characteristics of the Balance

A number of useful characteristics of the balance can be determined from the data presented in the previous plots. The natural torsion period of the balance is determined from the

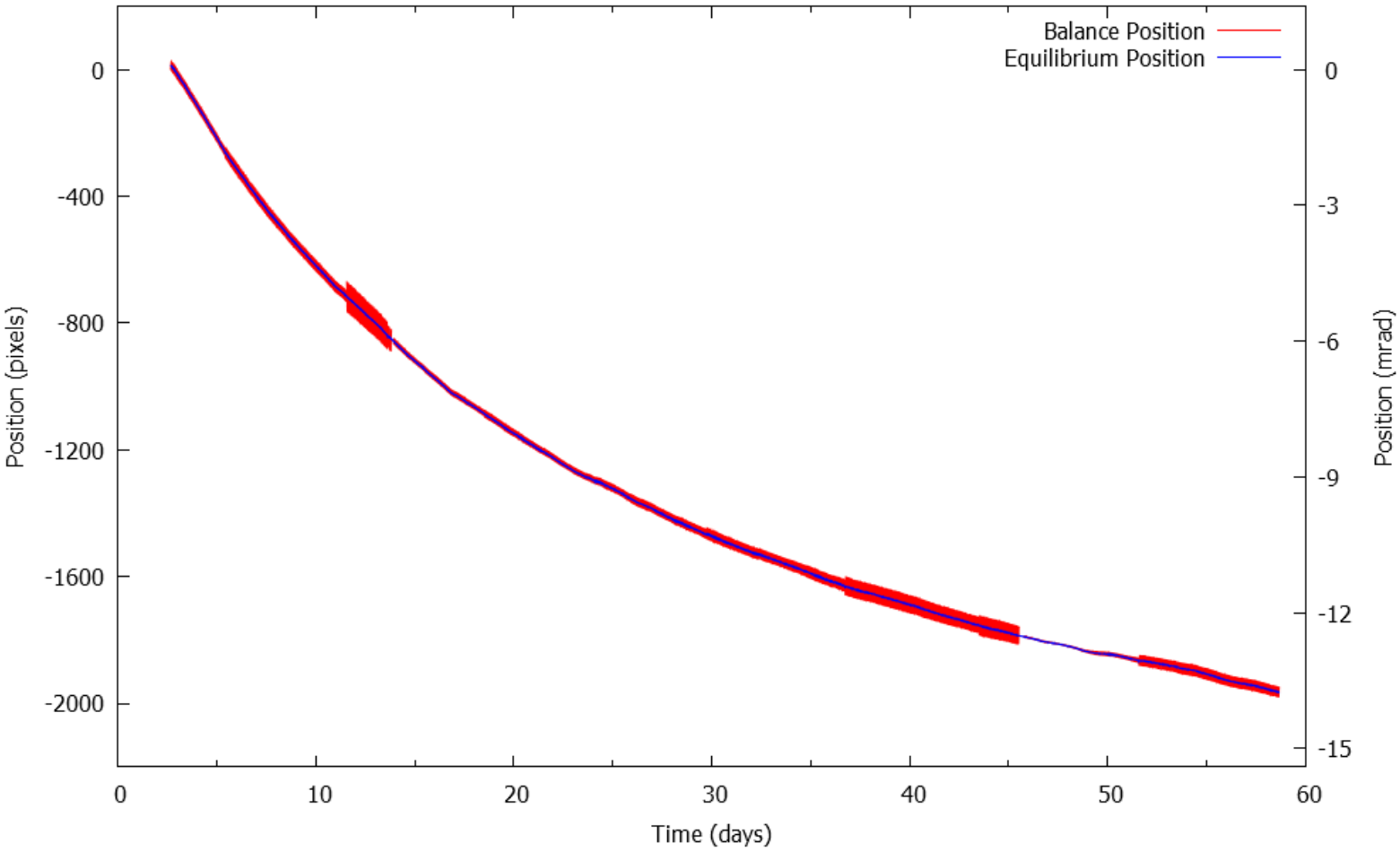

Figure 5.6: Balance position from each of the data files of the Fall 2015 data run is plotted in red. Jumps in the centroid value due to stick-slip processes and adjustments of the gimbal mirror have been corrected for. Plotted in blue is the balance position with torsional oscillations filtered.

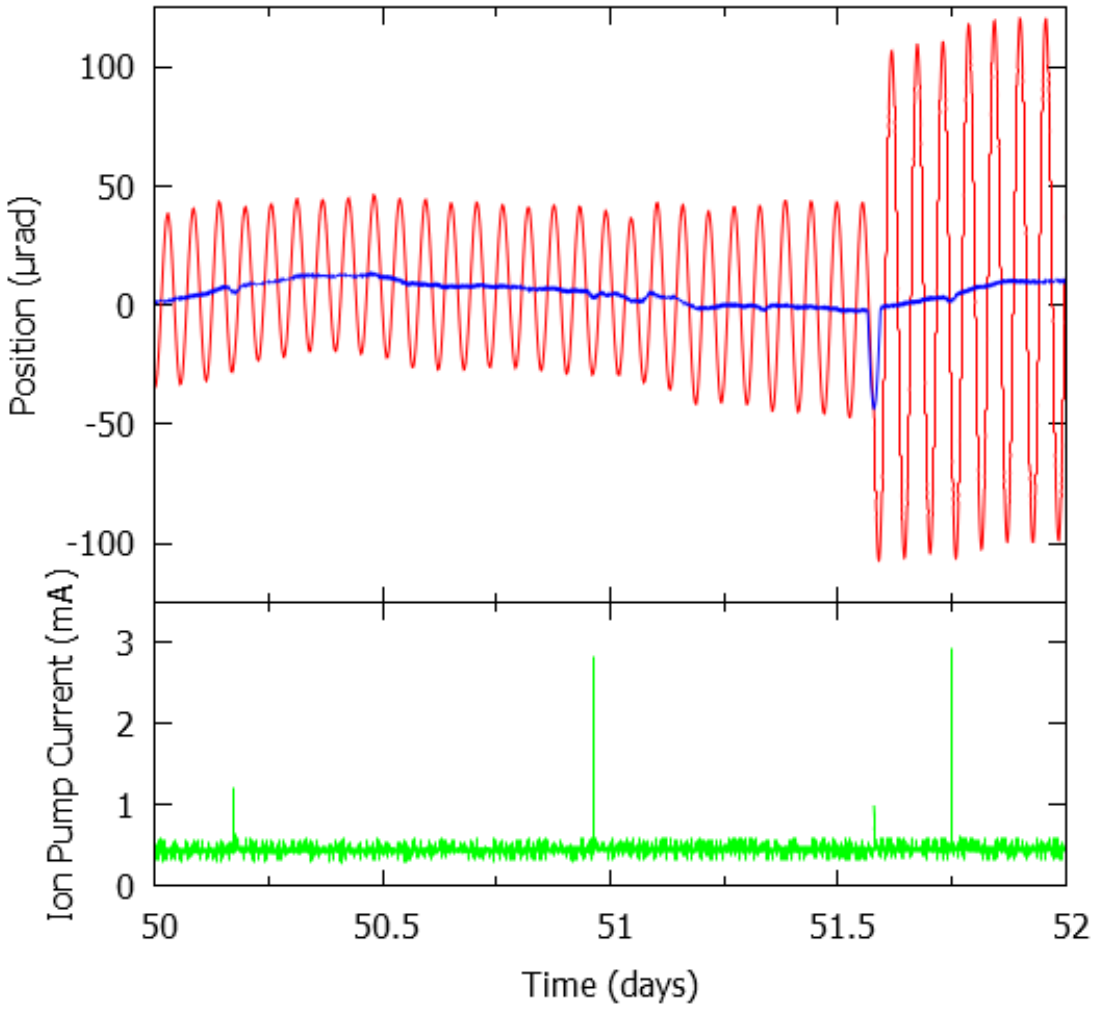

Figure 5.7: Top: An enlarged view of the balance position and filtered data with a linear drift term removed over a 2 day span. Bottom: The current measured across the ion pump which corresponds to the pressure in the chamber. The pressure spike at $t = 51.6$ days caused a glitch, where the balance motion is drastically effected. By referring to the filtered balance position at $t = 50.2, 50.95$, and 51.75 days, corresponding to other pressure spikes, it can be seen that these pressure bursts add noise to the system as well.

Fourier transform of the balance position. In addition, the Q factor, which is a measure of the energy lost in an oscillator, can be deduced from the width of the resonance peak by

$$Q = \frac{f_0}{\Delta f_{FW}} \tag{5.3}$$

where Δf_{FW} gives the full width at half maximum of the resonance peak at f_0. Figure 5.8 illustrates the amplitude spectral density for a portion of the balance position data that can be used to obtain the natural frequency $f_0 = 2.054 \times 10^{-4}$ Hz, which corresponds to a period of about 4868 s or 81.1 min, and $Q = 400$.

When calculating the Fourier transform of a discrete data set, discontinuities in the balance position between the beginning and end of the data set lead to a phenomenon called spectral leakage. Spectral leakage causes the power contained in some frequencies to be smeared into other frequencies, resulting in a spectral density with an amplitude that appears higher than it actually is and potentially hiding faint signals in the Fourier transform. This can be reduced by applying a window function to the original data set. A window function causes the data set to smoothly and gradually go to zero at its endpoints, removing discontinuities at these locations. One such window function, is a Hann window, defined by

$$w(n) = 0.5\left(1 - \cos\left(\frac{2\pi n}{N}\right)\right) \tag{5.4}$$

where $N + 1$ gives the number of points in the data set, and n is an index which ranges

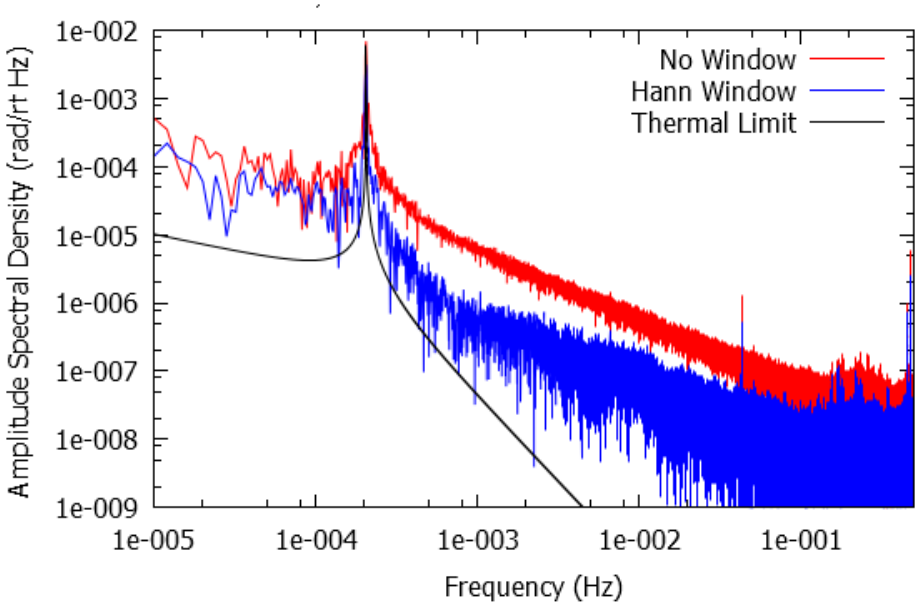

Figure 5.8: Amplitude Spectral Density of a portion of the balance position data. The red line shows the spectral density of the raw data, while the blue line shows the spectral density after applying a Hann windowing function to reduce spectral leakage. The thermal limit for this balance in the case that damping is due to internal losses in the fiber is shown in black.

from 0 to N. The use of a Hann window involves the trade-off that the spectral resolution is reduced. The blue line in Figure 5.8 shows the effect of applying a Hann windowing function on a data set. The thermal limit of the balance as given by Equation (3.16) is also drawn. It is clear the balance is operating above its thermal limit, and that energy is being fed into the system in the form of noise. In Chapter 7 suspected sources of this noise will be discussed.

5.3 Data Analysis

The purpose of the following analysis is to outline a general approach, and to illustrate the type of sensitivity this prototype instrument is capable of. In the case of an equiva-

lence principle violation, the signal that was determined in § 3.1 would have a very narrow bandwidth, on the order of $\Delta f \lesssim 10^{-7}$ Hz at $f_s = 1.157 \times 10^{-5}$ Hz. In addition, because any power in the Fourier transform at the signal bandwidth will be additive, the ability to resolve this signal in the frequency domain depends on the amount of noise in the Fourier transform of the balance position near the signal frequency f_s, not the amplitude. In order to clearly resolve a very narrow peak, and to reduce fluctuations near f_s, a very long data set is required. To obtain an observation bandwidth of $\Delta f = 10^{-7}$ Hz, a continuous data run of about $t_{obs} = 115$ days is the minimum length required. After this time, the noise in the signal goes as $t_{obs}^{-1/2}$, so a next generation instrument will target a $t_{obs} = 1$ year data run.

5.3.1 In the Time Domain

As a first order analysis, the filtered balance position data were studied in the time domain. The continuous data set shown in Figure 5.6 was split into 24 hour segments based on a start and end time that correspond to the Sun being at the nadir — when no torque acts on the balance from a potential violation of the equivalence principle. Next a linear drift term is removed from these segments such that the initial and final positions have position values of $\theta = 0$. The slope of these linear terms gives the drift rate of the fiber; this is plotted for the Fall 2015 data set in Figure 5.9. An upper limit on the portion of the remaining balance deflection that could be due to a violation of the equivalence principle violation is obtained by determining the amplitude of the sine function which is a best fit to the drift subtracted 24 hour segments. The amplitude of this signal θ_A is determined by

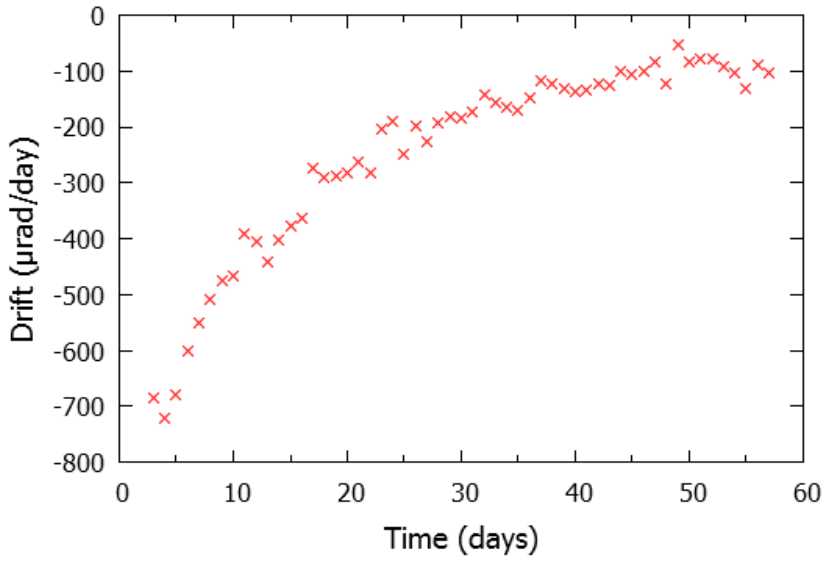

Figure 5.9: Balance drift rate during the Fall 2015 data run.

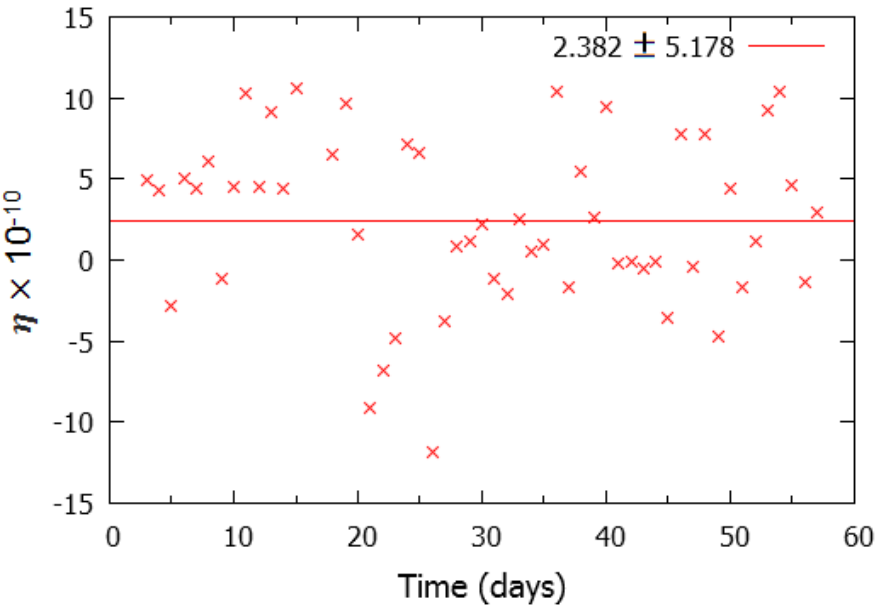

Figure 5.10: Limits on η found by fitting the position data obtained during the Fall 2015 data run. The mean to these points is also plotted, $\eta = (2.382 \pm 5.178) \times 10^{-10}$, where the uncertainty in the measurement is given as the standard deviation in the mean.

$$\theta_A = \frac{1}{12}\int_0^{24} \theta(t) \sin\left(\frac{2\pi t}{24}\right) dt \tag{5.5}$$

where here time t is given in hours. From Equation (3.2) and Equation (3.6), θ_A can be used to place a limit on the Eötvös parameter η. These results are shown in Figure 5.10. For this analysis, which aims only to obtain a sense of the balance performance, the approximation $a_\odot = GM_\odot/R^2 \approx 0.59$ cm s^{-2} has been used. In addition to some simplifying assumptions, this method includes contributions from frequencies besides the diurnal signal frequency. For a more rigorous analysis, using the Fourier transform of a long continuous data run is preferable.

5.3.2 In the Frequency Domain

Fourier analysis makes it possible to discern information about signals at specific frequencies even in the case of a complicated signal with multiple driving forces present. Thus, such an approach is well suited for detecting the well predicted signal arising from a violation of the equivalence principle. The Fourier transform of the filtered position data shown previously in Figure 5.6 is shown in Figure 5.11 for the region near the diurnal signal frequency, along with a linear best fit to these points. It is the residuals to this fit that can be used to place a limit on a signal due to a violation of the equivalence principle.

For a residual amplitude in the amplitude spectral density $\Delta\theta_{AC} = 3 \times 10^{-5}$ rad Hz$^{-1/2}$ at f_s and a bandwidth $\Delta f = 10^{-6}$ Hz,

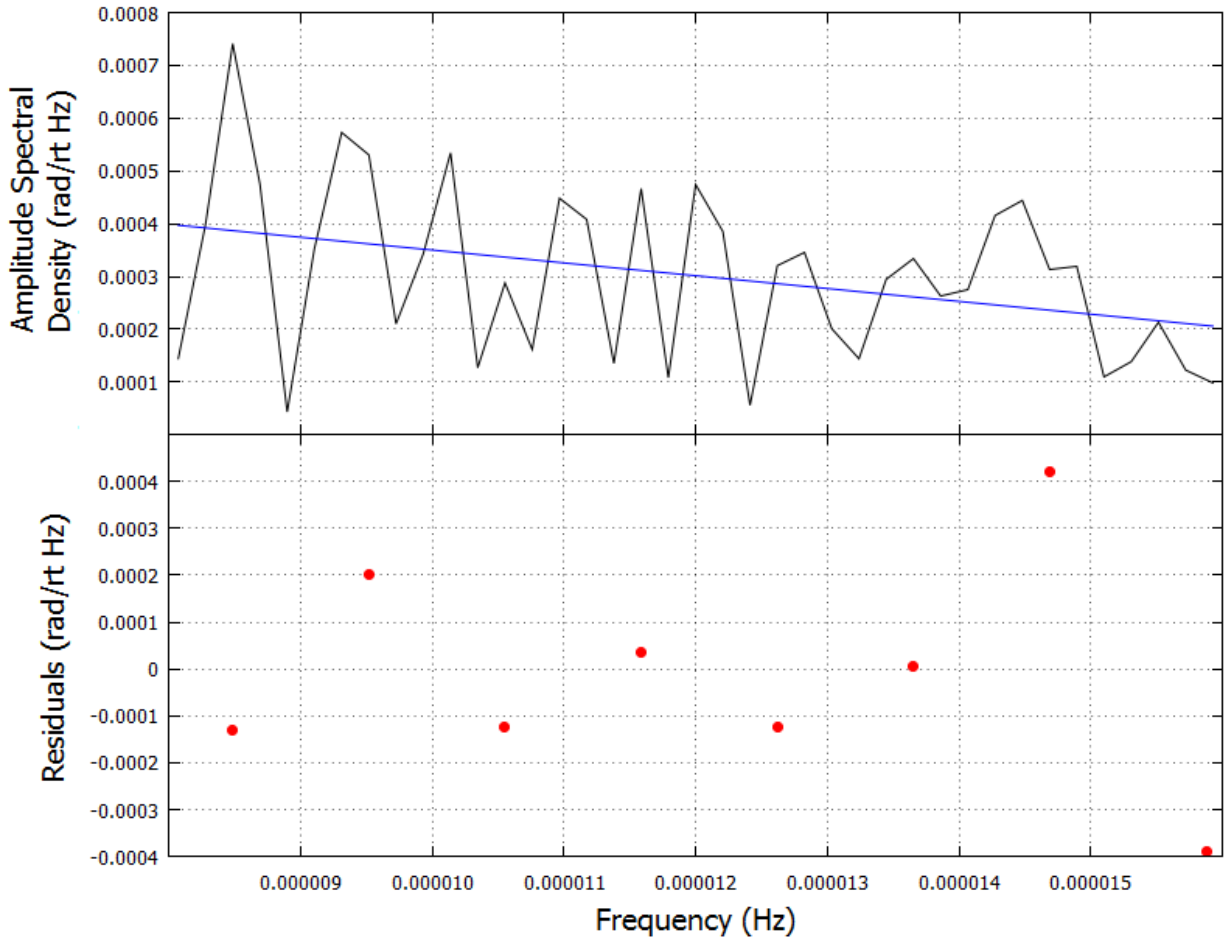

Figure 5.11: Top: Amplitude Spectral Density of the filtered Fall 2015 data run near the diurnal signal frequency, a best fit line is given in blue. Bottom: Residuals to this best fit line averaged over a bandwidth of 10^{-6} Hz.

$$\theta = \Delta\theta_{AC}(\Delta f)^{1/2} \approx 3 \times 10^{-8}\text{rad}. \tag{5.6}$$

Then by consulting Equation (3.2) and Equation (3.6), a value of $\eta \approx 6 \times 10^{-12}$ can be determined from this deflection. The uncertainty in this value depends on the scatter of the Fourier transform points about the best fit line, thus for the relatively short data run shown here the uncertainty is quite large, about an order of magnitude larger than the value itself.

In addition to reducing Δf, a longer data set would reduce the fluctuations in the region near f_s. As the spectral resolution improves, the phase associated with the Fourier components near the signal frequency can also be used to reduce the uncertainty in this limit.

5.4 Study of the Laboratory

Part of this effort has involved the characterization of the Tyson Research Center bunker as a suitable laboratory for a low frequency torsion balance experiment. As mentioned previously, thermal stability and low seismic noise are key qualities for an ideal site. Measurements made prior to the Fall 2015 data run indicated that the conditions inside the bunker were favorable for this experiment; observations of the instrument during the Fall 2015 data run have allowed for a more thorough assessment of this location.

5.4.1 Thermal Stability

In addition to the position of the balance, the temperature inside the bunker was continuously monitored during the Fall 2015 data run using the thermistors described in § 4.4.2. In Figure 5.12 the response of the temperature inside the bunker can be compared to temperature swings in the outside air temperature, obtained from the Weather Underground online database for Lambert-Saint Louis International airport [7]. It is immediately apparent that the diurnal temperature swings are significantly reduced, and upon close inspection it can be discerned that low frequency temperature trends in the outside air temperature are ap-

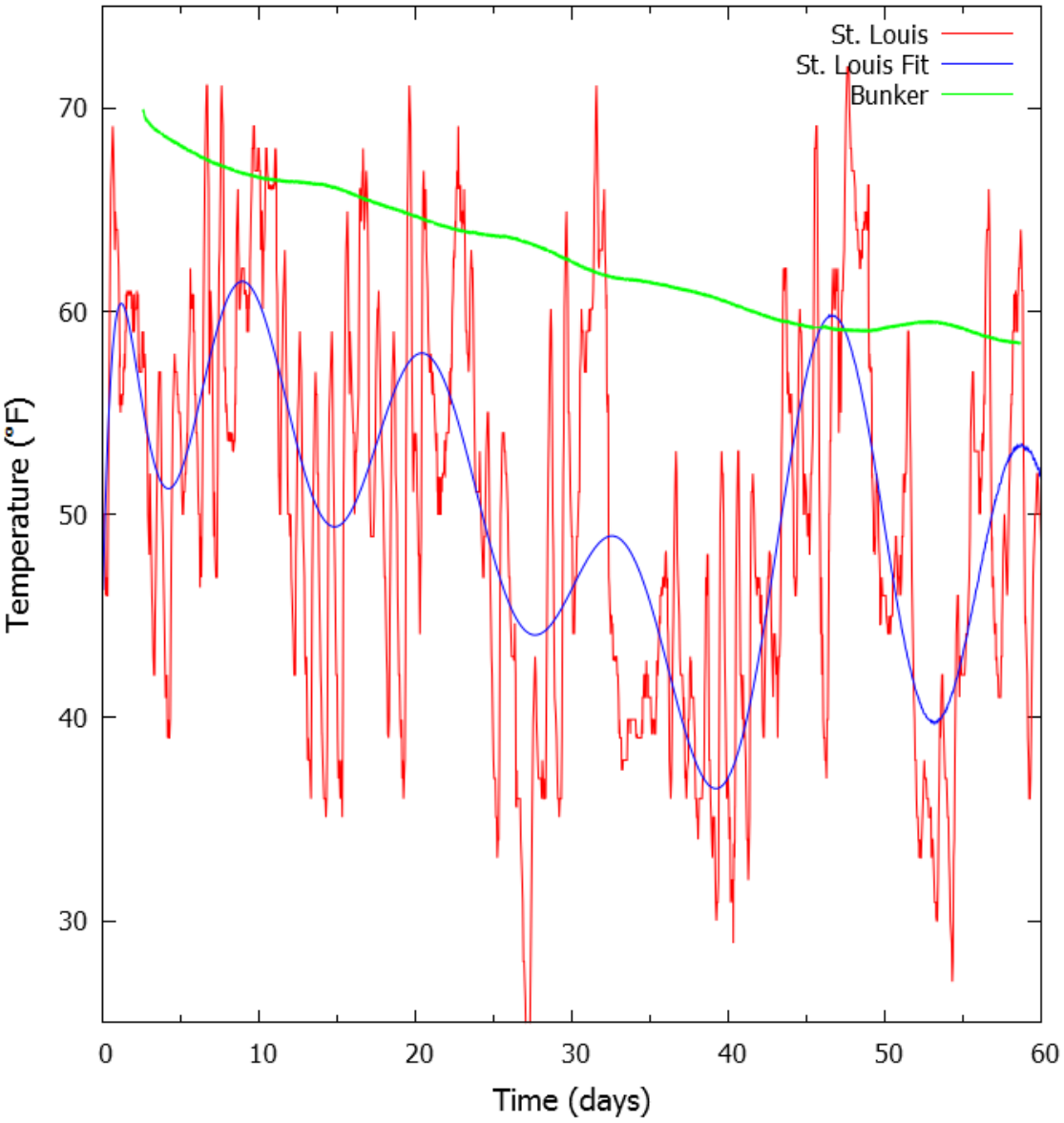

Figure 5.12: Temperature during the Fall 2015 data run. The temperature reported at Lambert-Saint Louis International airport is plotted in red, while a high-order polynomial fit to this data is plotted in blue to show low frequency trends. The temperature inside the Tyson bunker is shown in green. As with the plots of balance position, here $t = 0$ corresponds to 00:00:00 CDT on October 26, 2015.

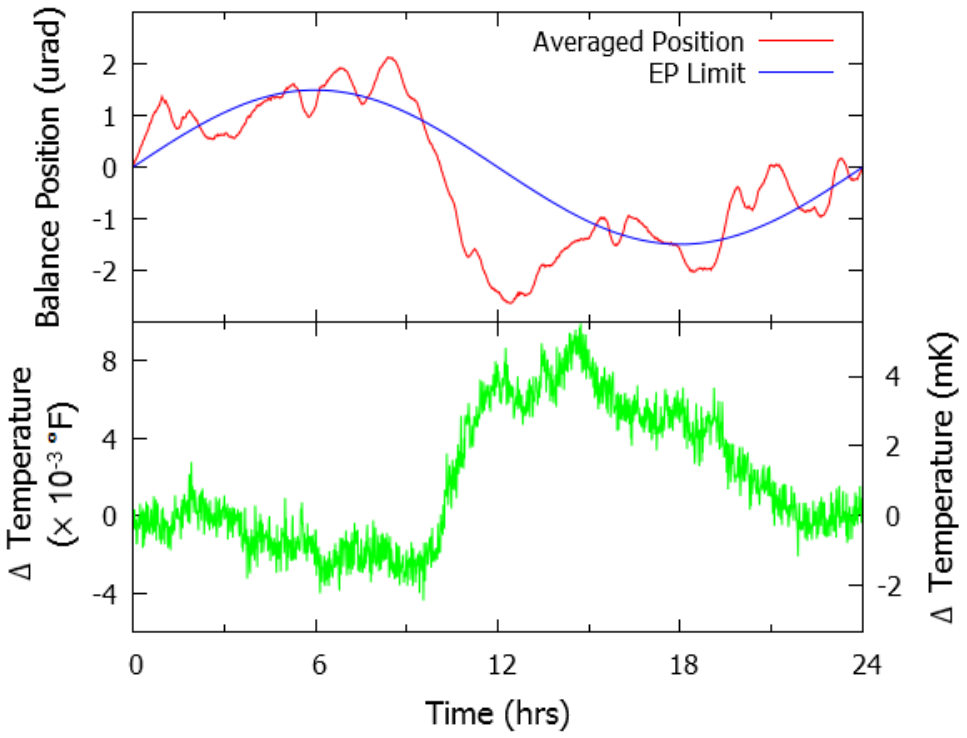

Figure 5.13: Balance position with a linear drift removed, averaged over multiple 24 hour segments shown in red. The best fit for a violation of the equivalence principle in this position data is plotted in blue with an amplitude of 1.492 µrad. The bunker air temperature with a linear drift removed, averaged over separate days is shown in green.

parent in the internal bunker temperature through convective air flow but with a phase lag of approximately 5 days and a significant reduction in amplitude.

To gain insight into the daily temperature behavior, the bunker temperature was analyzed in a similar fashion as outlined for balance position in § 5.3.1. After splitting the data shown in Figure 5.12 into 24 hour segments and removing a linear drift term, the temperature inside the bunker was averaged over each day of the data run and the result is plotted in Figure 5.13. The daily temperature variation, which is of particular interest for an equivalence principle

test with an expected signal with a daily frequency, is $\lesssim$ 7 mK and is approximately in quadrature with the signal expected for an equivalence principle violation. Also shown in Figure 5.13, is the balance position once a linear drift has been removed, averaged over the same time frame. While measuring a direct correlation between balance drift and bunker temperature variation was not particularly fruitful on a day by day basis, the addition of thermal shielding (as described in § 4.4) was explored as a first step to reduce noise in the system.

5.4.2 The Effect of Wind

Another environmental noise source arises from the coupling between wind and the trees located on top of the Tyson bunker. As shown in Figure 5.14, it appears that some amount of vibrational energy is fed into the system during periods of high winds. This is an unfortunate, but unavoidable quality of the bunker laboratory. Fortunately the time period shown here was the windiest period during the Fall 2015 data run; generally any effects caused by gusts of wind are not noticeable. Because this source of noise is not a regularly occurring daily event it is not particularly worrisome for this experiment.

5.5 Follow-Up Data Run

After completing the installation of thermal shielding around the experiment, the Winter 2016 data run commenced on February 27, 2016. The balance position over this data run is

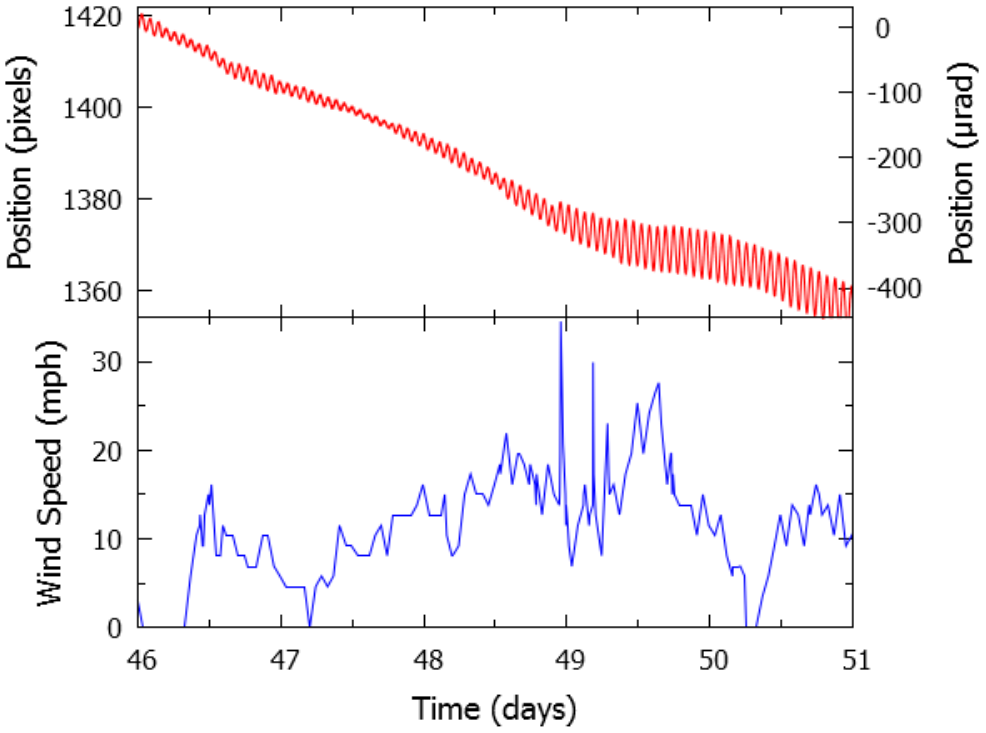

Figure 5.14: Top: Balance position over a span of 5 days. Bottom: Wind speed measured over this period [7]. The largest gusts seem to introduce vibrational energy into the torsion balance system resulting in an increase of oscillation amplitude.

plotted in Figure 5.15. The low frequency drift of the balance was greatly reduced by the time this data run began (see Figure 5.16). Limits on η placed via the analysis approach described in § 5.3.1 are plotted in Figure 5.17. Again, it should be emphasized that this approach yields limits on η with contributions from many frequencies, and has been used only to assess the quality of the data. Unexpectedly, the addition of thermal shielding seemed to be detrimental to these results. A look at the thermistor data averaged over each complete day of this data run offers an indication as to why this is the case. Comparing the average daily temperature swings during the Fall 2015 and Winter 2016 data run shows that

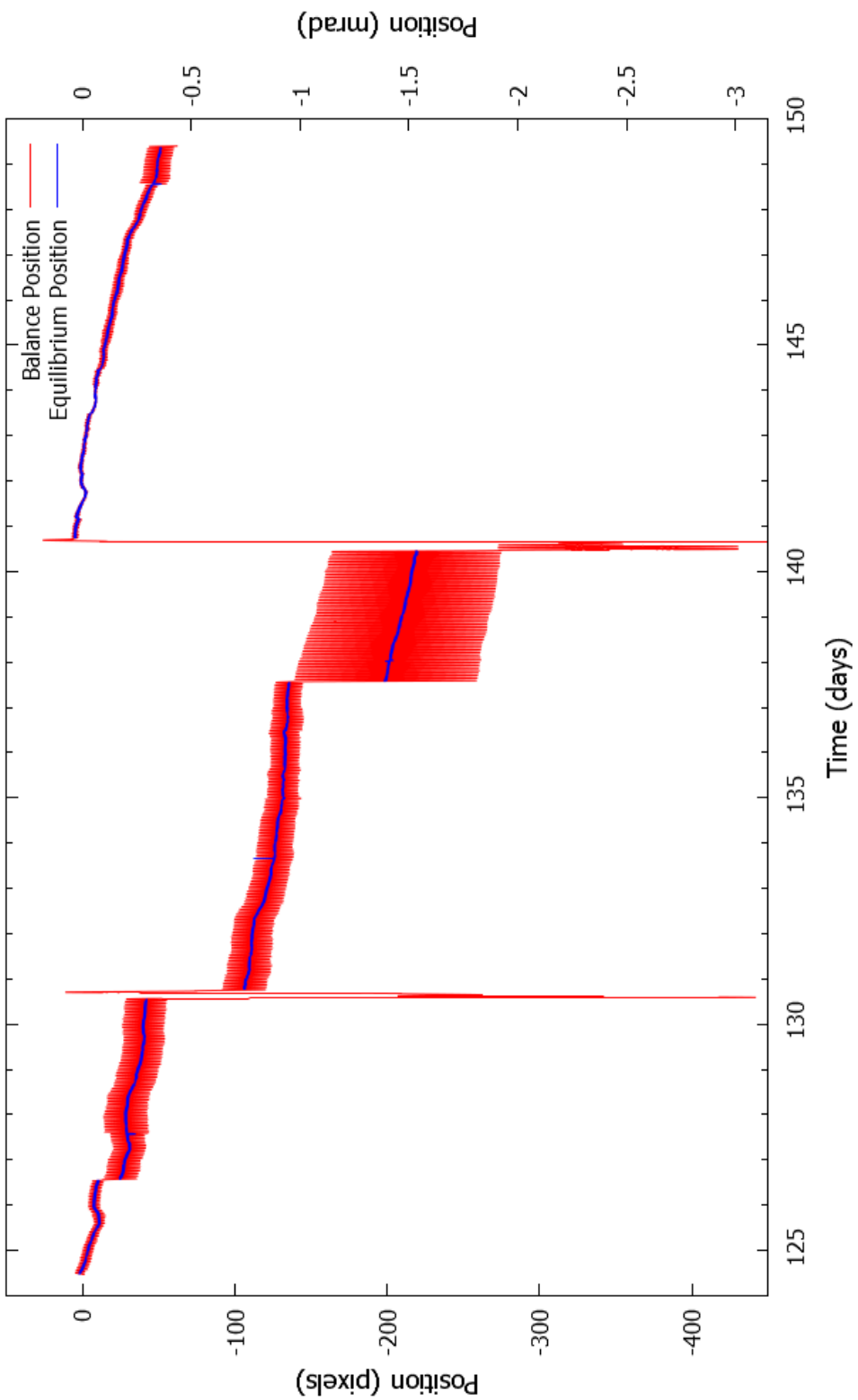

Figure 5.15: Balance position (in red) and equilibrium position (in blue) for the Winter 2016 data set. At $t = 126.5$ days a sudden shift of the balance equilibrium position occurred, at $t = 127.6$ days a glitch increased the amplitude of oscillations, at $t = 130.5$ days the position of the gimbal mirror was adjusted, at $t = 137.6$ and 140.8 days shifts of the equilibrium position occurred, at $t = 140.7$ days the position of the gimbal mirror was adjusted again to improve the quality of the reflected image and the amplitude of torsional oscillations of the balance was damped. At $t = 148.6$ days another pressure burst caused a glitch. Here $t = 0$ again corresponds to 00:00:00 CDT on October 26, 2015, consistent with the Fall 2015 data set.

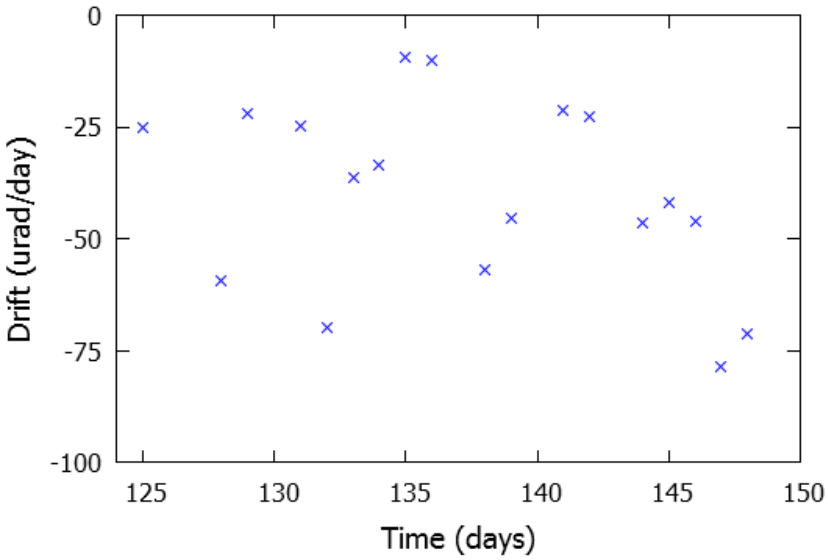

Figure 5.16: Balance drift rate during the Winter 2016 data run. By the beginning of this data run the balance had been suspended for about 8 months.

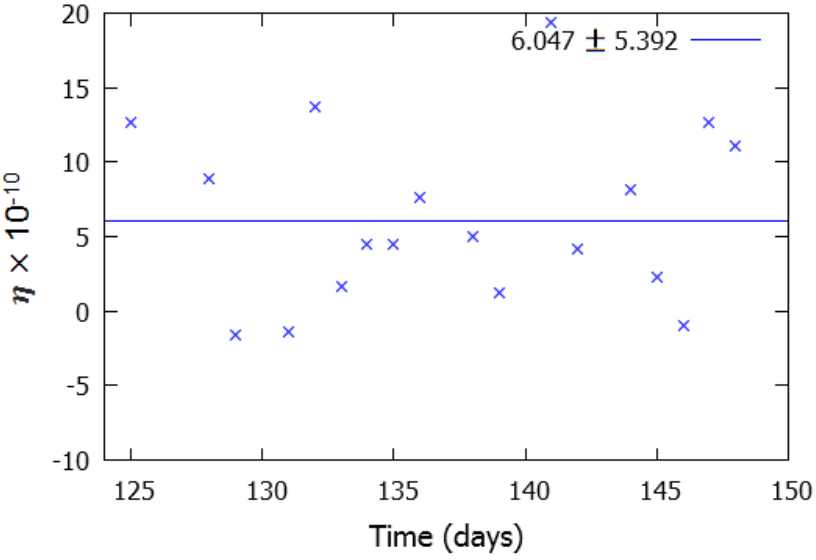

Figure 5.17: Limits on an equivalence principle violation obtained from the position data from the Winter 2016 data run with two layers of thermal insulation enclosing the experiment. The analysis followed the procedure outlined in § 5.3.1. The result was $\eta = (6.047 \pm 5.392) \times 10^{-10}$, where the uncertainty is found from the standard deviation of the data points.

the thermal insulation reduces the daily variation by about 15% — from 6.4 mK without insulation, to 5.5 mK with it — while also introducing a phase shift of about 6 hours. Inconveniently, this causes the peak of this temperature variation to approximately coincide with the expected maximum signal from a potential equivalence principle violation. The temperature dependence of many components of the experiment suggests that the inferior bounds on a violation of the equivalence principle obtained from the Winter 2016 data run, $\eta = (6.047 \pm 5.392) \times 10^{-10}$, are limited by the thermal variation in the laboratory. Means of reducing this issue vary in complexity from an active temperature stabilization system to increasing the amount of thermal insulation enclosing the experiment to correcting for thermal effects on the optics system; a proposed scheme for employing the latter approach has been tested and will be discussed in § 7.2.1.

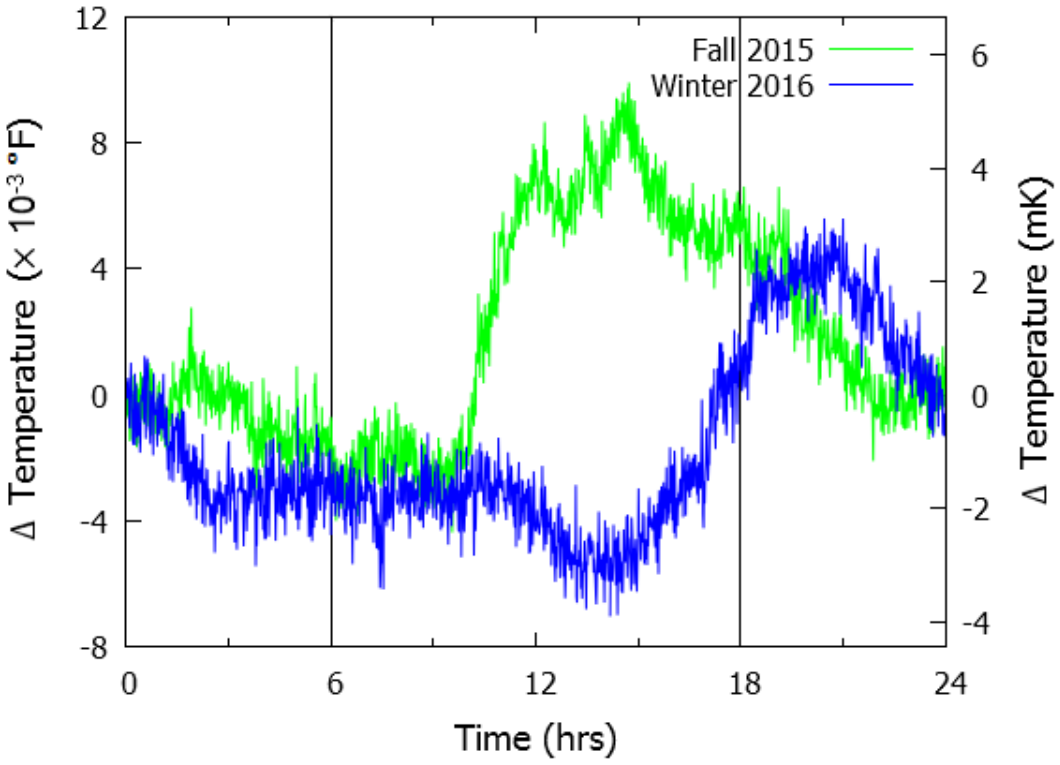

Figure 5.18: Averaged daily temperature variation with a linear drift removed plotted for the Fall 2015 data run (in green) and the Winter 2016 (in blue). While the general trends for each of these data runs are similar, the thermal insulation in place for the Winter 2016 data run seems to introduce a phase shift of about 6 hours. This coincides closely with the times of expected signal maxima from a potential equivalence principle violation, which are marked by vertical lines at $t = 6$ and 18 hours.

Chapter 6

The Earth's Normal Modes

The constructive interference of seismic waves excited during an earthquake creates a standing wave pattern of global free oscillations which are characterized by discrete frequencies which depend on the type of motion involved, and the interior structure of the Earth. These so-called normal modes exist as spherical modes, where oscillatory motion occurs outward from the Earth's center, and torsional (or toroidal) modes, which cause ground rotations about a vertical axis. These oscillations are of interest because they can provide important information about large-scale properties of the Earth, as well as improve understanding of sources and propagation of earthquakes.

Traditionally, seismic observations are made by measuring translational displacement in the x, y, and z directions, however these detectors are poorly suited to measure the low frequency rotational motion associated with normal mode oscillations. Recently, Igel and others have used a ring laser system to observe the torsional free oscillations triggered by

large magnitude earthquakes [89]. In 2007, Cowsik presented a novel approach of directly observing toroidal normal modes, including the lowest frequency mode at 0.37 mHz [5]. The concept behind this approach, using a torsion balance with a long natural period, can be summarized as follows: A torsion balance which has a point of suspension that is fixed to the Earth and has a natural frequency significantly below the frequency of rotational seismic oscillations will couple negligibly to these oscillations. On the other hand, a optical lever which is also fixed to the Earth will follow these seismic motions, thus the measured signal will be of the same magnitude as the seismic rotational motion. Measurements of normal mode oscillations made using this instrument stand to compliment previous observations of rotational seismic motion, as well as the standard translational, strain, and gravitational measurements used to characterize earthquakes.

6.1 Overview of Normal Modes

Free oscillations of the Earth were predicted as early as the 19th century, though they were not observed until 1960. In 1882, Lamb provided a mathematical description of spheroidal and toroidal oscillations for a non-gravitating elastic sphere [90]. Alterman et al. would later calculate theoretical values of the eigenfrequencies of these oscillations for a spherically symmetric Earth [91]. This model was validated to first order after the first unambiguous observations of the Earth's normal modes made by Benioff et al. after the great Chilean earthquake in May 1960 using data from strain and pendulum seismographs [92]. Mod-

ern geophysics relies on the comprehensive Preliminary reference Earth model (PREM), developed by Dziewonski and Anderson [93], to describe the Earth's internal structure by considering radial anisotropic parameters including several elastic parameters and density based on 12 years of seismic observations.

Observations of the Earth's normal modes promise to provide otherwise unobtainable insight about the deep interior of the planet. In addition to providing improved constraints on physical quantities such as density and P-wave and S-wave velocities, studies of these oscillations will improve understanding of properties of earthquakes, such as the energy, geometry, and duration of specific events. It has been suggested that the amplitude and damages caused by rotational motions are underestimated, particularly because these motions may couple to ground tilt [94, 95]. Additional questions that stand to be addressed include the amplitudes of normal modes without the occurrence of a major seismic event, how the spectra of different earthquakes compare, and whether the continuous "hum" of spherical modes that has been observed at frequencies between 2 and 7 mHz, suspected to arise from interactions between the atmosphere, ocean, and seafloor, has an analogous signal in torsional modes [5, 96, 97].

The first measurements of the Earth's torsional and spherical normal modes were made by Benioff et al. using strain and pendulum seismograph readings made in California and Peru from the great Chilean earthquake of May 1960 [92]. This landmark (albeit indirect) detection measured normal modes ranging in period from 54.7 minutes to 3.66 minutes and Q values of greater than 100 for these modes. Data from this incipient observation helped in

the development of improved seismic models. Observations of the magnitude 9.3 Sumatra-Andaman earthquake in December 2004 using two crossed laser extensometers operating in an underground laboratory in Gran Sasso, Italy produced unprecedented resolution of torsional mode oscillations with sub-mHz frequencies [98]. The improved resolution of these measurements showed a few features of both the frequency and time evolution that were not in close agreement with model predictions. The reasons for these discrepancies are under investigation.

In 2011, Igel et al. reported on the first direct observations of the Earth's torsional normal modes using a ring laser system sensitive to rotational ground motions about a vertical axis [89]. These observations were made in the 0.5-4 mHz frequency band following the magnitude 9.0 Tohoku-Oki earthquake that occurred in March 2011. The instrument, located at the Geodetic Observatory in Wettzell, Germany, uses two laser beams traveling in opposite directions along a closed square path rigidly attached to bed rock to detect the rotation rate of a sensor, manifest as a beating of the resulting interference pattern, via the Sagnac effect.

Since the first observations of the Earth's normal modes in 1960, advances in seismological instruments have continued to improve the quality of the measurements of these oscillations. Despite these gains, the gravest normal modes have still been difficult to detect and have only been observed following earthquakes of significant magnitude. Igel and others have stressed the importance of developing improved methods for studying rotational seismology, and have worked to stimulate efforts in this field [99].

6.2 Calculation of Normal Modes and Expected Balance Response

Following Stein and Wysession [100], an expression for the rotational motion of a specific event corresponding to torsional modes is obtained starting from the displacement vector for rotations about the local zenith, given in terms of spherical coordinates with the origin located at the center of the Earth and the seismic source located at the pole ($\theta = 0$). The displacement is given by

$$\mathbf{u}^T(r,\theta,\phi) = \sum_n \sum_l \sum_m {}_nA_l^m \, {}_nW_l(r)\, T_l^m(\theta,\phi) e^{i\left({}_n\omega_l^m\right)t} \tag{6.1}$$

where ${}_nA_l^m$ are excitation amplitudes that depend on the location and strength of the seismic source, ${}_n\omega_l^m$ are the eigenfrequencies corresponding to ${}_nA_l^m$, and ${}_nW_l(r)$ gives the radial dependence of the rotation amplitudes. The surface eigenfunctions T_l^m are given in terms of vector spherical harmonics, with components

$$T_l^m = \left(0, \frac{1}{\sin\theta}\frac{\partial Y_l^m(\theta,\phi)}{\partial\phi}, -\frac{\partial Y_l^m(\theta,\phi)}{\partial\theta}\right) \tag{6.2}$$

where the normalized spherical harmonics Y_l^m are given by Stein and Wysession [100] as

$$Y_l^m(\theta,\phi) = (-1)^m \left[\left(\frac{2l+1}{4\pi}\right)\frac{(l-m)!}{(l+m)!}\right]^{1/2} P_l^m(\cos\theta) e^{im\phi}. \tag{6.3}$$

Mode	*Frequency (mHz)*	*Period (min)*
${}_0T_2$	0.371	44.9
${}_0T_3$	0.586	28.5
${}_0T_4$	0.770	21.6
${}_0T_5$	1.08	15.4
${}_0T_6$	1.23	12.5

Table 6.1: The lowest eigenfrequencies and corresponding periods of the fundamental torsional modes of the Earth [5].

Each mode is described by its radial order n which describes how the mode varies with radius, angular order l which describes how it varies with latitude, and azimuthal order m which corresponds to longitude. For torsional modes, denoted as ${}_nT_l^m$, n gives the number of spherical nodal surfaces within the earth. The fundamental modes, which correspond to $n = 0$, have no nodal surfaces, and describe motion which is in the same direction at all depths for any given latitude or longitude. Modes with $n > 0$ are called overtones. The number of nodal lines on the earth's surface is equal to $l - 1$, and the number of vertical nodal planes which pass through the poles is given by the azimuthal order m. The displacements associated with several torsional modes is illustrated in Figure 6.1. In Table 6.1, the eigenfrequencies of the longest fundamental modes are given for a spherically symmetric non-rotating Earth. This model ignores the $(2l + 1)$ splitting of frequencies that occurs in reality due to the Earth's rotation and lateral heterogeneities; however because this splitting is quite small, this simplification is generally a reasonable approximation.

The rotations about the local zenith are calculated by taking the curl of the displacement field

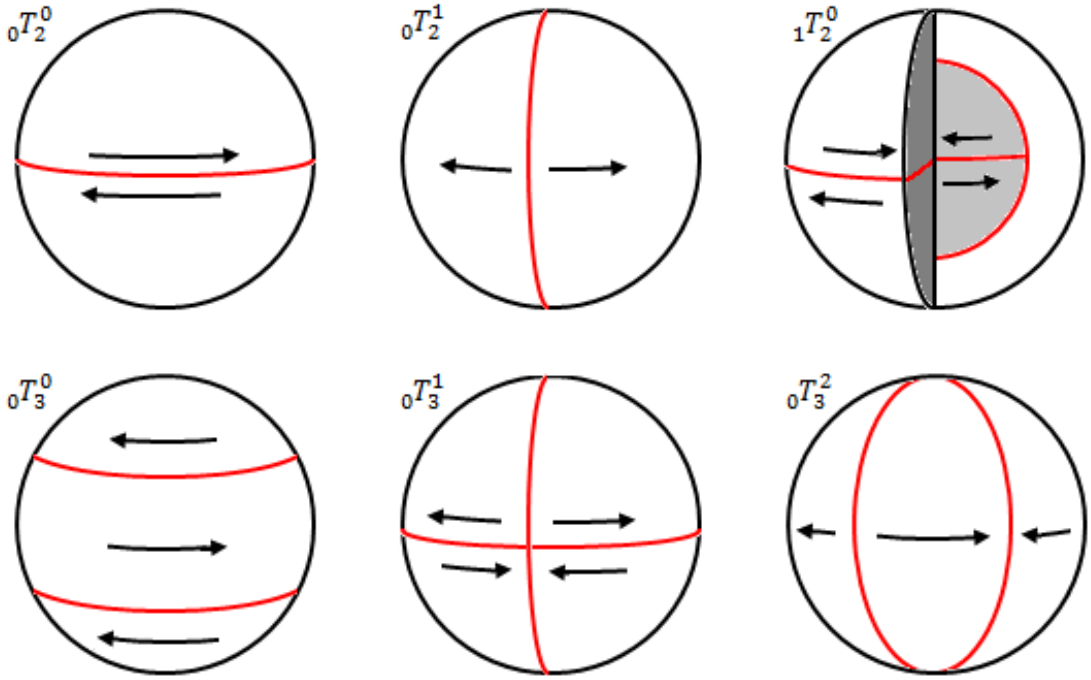

Figure 6.1: Illustration of the displacements associated with various torsional normal modes ${}_nT_l^m$; nodal lines are shown in red. The number of spherical normal modes within the Earth is given by n, while the number of surface nodal lines is given by $l-1$. The horizontal displacements u_θ and u_ϕ are zero along the nodal lines.

$$
\begin{aligned}
R(r,\theta,\phi) &= \left(\nabla \times u^T\right) \cdot \hat{\mathbf{r}} \\
&= \sum_n \sum_l \sum_m {}_nA_l^m \, {}_nW_l\,(r)\, e^{i\left({}_n\omega_l^m\right)t} \times \frac{1}{r\sin\theta} \\
&\quad \times \left[-\frac{1}{\sin\theta}\frac{\partial^2 Y_l^m}{\partial\phi^2} + \cos\theta\frac{\partial Y_l^m}{\partial\theta} + \sin\theta\frac{\partial^2 Y_l^m}{\partial\theta^2} \right] \\
&= \sum_n \sum_l \sum_m R({}_n\omega_l^m)(\cos {}_n\omega_l^m t + i \sin {}_n\omega_l^m t).
\end{aligned}
\tag{6.4}
$$

The response of the balance when the point of suspension undergoes seismic oscillations was shown by Cowsik [5]. Considering the real part of one of the Fourier components of the

rotational ground motion found in Equation (6.4), the torque acting on the balance is given by

$$\tau(\omega) = \kappa_f R(\omega) cos(\omega t) = I\omega_0^2 R(\omega)\cos(\omega t) \tag{6.5}$$

where ${}_n\omega_l^m$ is written as ω for convenience and ω_0 is the natural torsional frequency of the balance. The response of the balance to this torque is given by

$$\ddot{\theta} + 2\beta\dot{\theta} + \omega_0^2\theta = \omega_0^2 R(\omega)\cos(\omega t) \tag{6.6}$$

where θ, β, and ω_0 are the angular displacement, damping term, and the natural torsional frequency of the balance respectively, as given previously in § 3.1. The particular solution to this equation is then

$$\theta = \frac{\omega_0^2 R(\omega)}{[(\omega_0^2 - \omega^2)^2 + 4\omega^2\beta^2]^{1/2}}\cos(\omega t - \delta) \tag{6.7}$$

where δ is the phase shift given by $\delta = \sin^{-1}\left(\frac{2\omega\beta}{\omega_0^2 - \omega^2}\right)$.

The optical lever is rigidly attached to the experiment's support frame which rests on the ground and thus follows the rotational motion

$$\theta_L = R(\omega)\cos(\omega t). \tag{6.8}$$

In the case that $\omega \gg \omega_0$ and the Q of the balance is reasonably high, the resulting angle

measured by the autocollimator α is then given by

$$\begin{aligned}\alpha &= \theta - \theta_L \\ &= \frac{\omega_0^2 R(\omega)}{[(\omega_0^2 - \omega^2)^2 + 4\omega^2\beta^2]^{1/2}} \cos(\omega t - \delta) - R(\omega)\cos(\omega t) \\ &= -R(\omega)\cos\omega t.\end{aligned} \tag{6.9}$$

Thus the instrument measures seismic rotational oscillations with unit response with a phase shift of π rad, provided that the natural frequency of the balance is significantly below the signal frequency. The amplitude spectral density of balance position and velocity over a period of several days is shown in Figure 6.2. As indicated by these plots, the amplitude of oscillation that the instrument can detect at present sensitivity can be estimated as described by Equation (3.9). Rotational ground motions arising from the Earth's normal modes with frequencies near 1 mHz and Q values of at least 200, can be detected for amplitudes of about a nanoradian.

6.3 Study of Data Obtained During Large Earthquakes

During the Fall 2015 and Winter 2016 data runs small earthquakes originating in the geographic vicinity of the torsion balance, often in Oklahoma or California, were briefly detected as an increase in amplitude of the pendular motions of the balance which was quickly damped by the eddy current damping system. During the Fall 2015 data run, a pair of 7.6 magni-

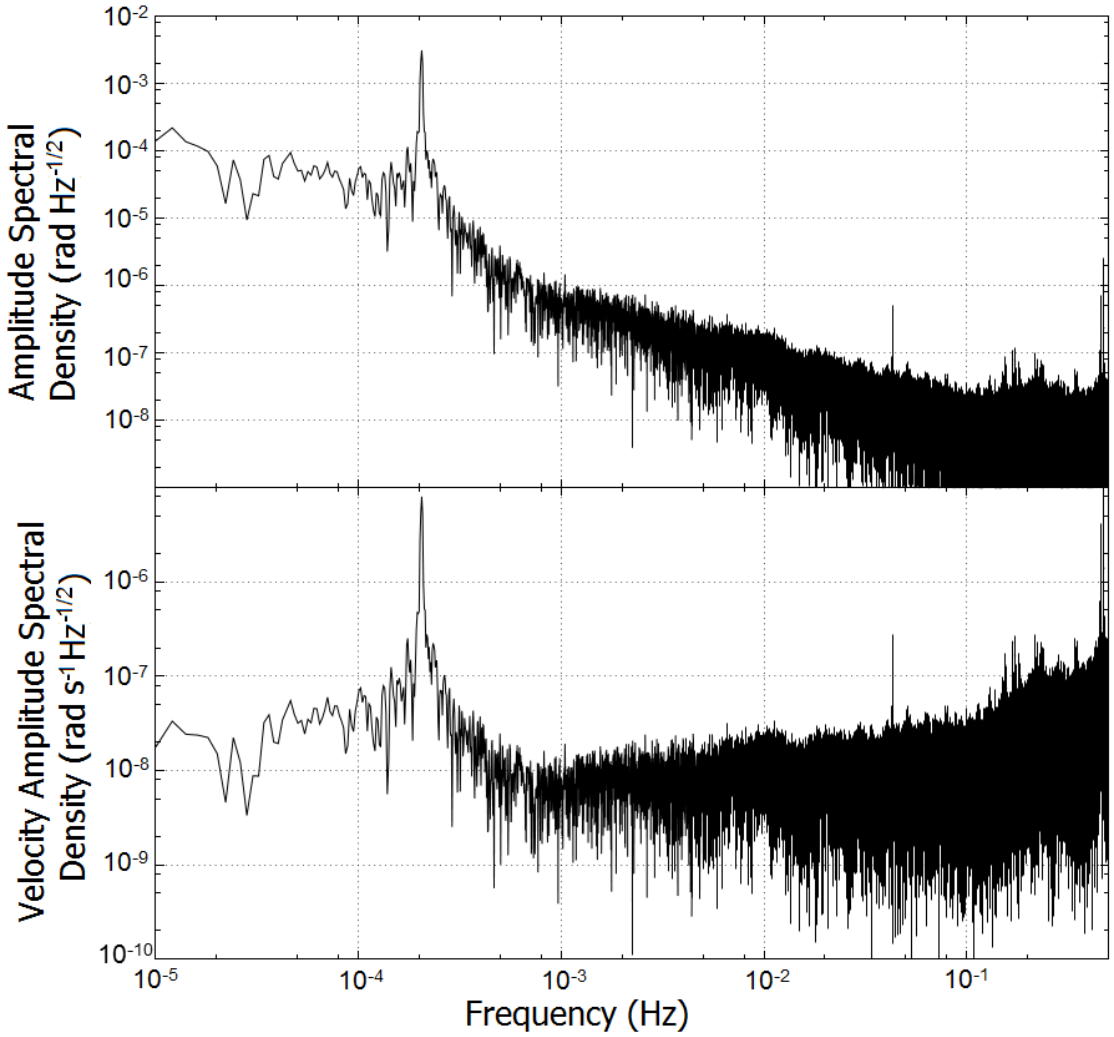

Figure 6.2: Amplitude spectral density of position and velocity of the torsion balance over a period of several days. Shown here to illustrate the current sensitivity of the instrument. The peak near $f_0 = 2 \times 10^{-4}$ corresponds to the natural torsional oscillations of the balance, while the peaks at high frequencies arise from pendular, wobble, and bounce modes of the balance.

tude earthquakes occurred within five minutes of each other in South America to which the balance showed significant response. The data collected from the instrument during these events were studied for evidence of the lowest frequency torsional normal modes; this is presented below. It is worth noting that these events are significantly smaller than the events

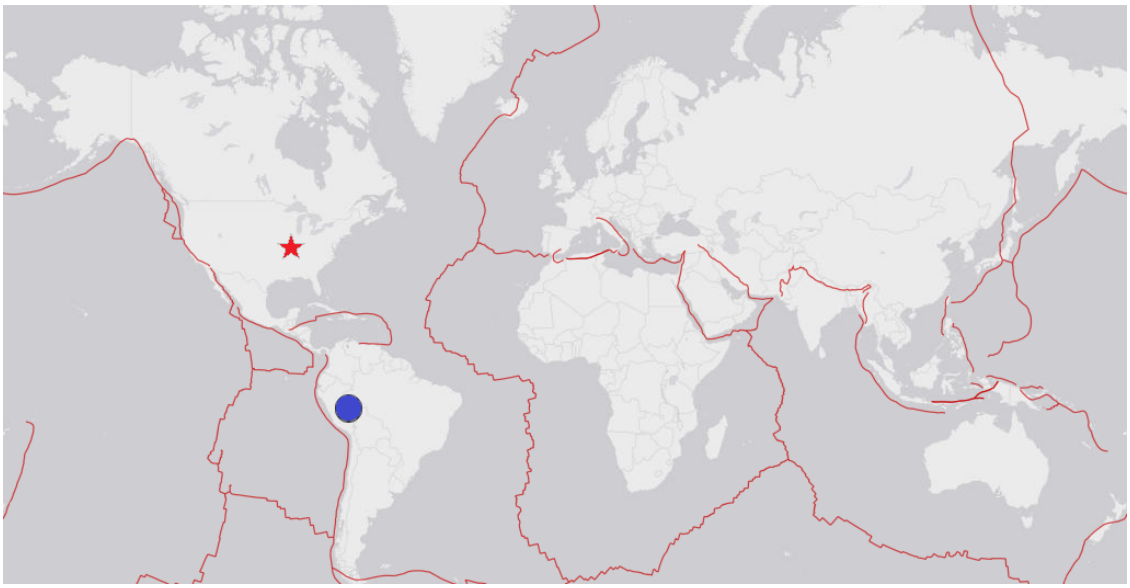

Figure 6.3: The blue circle gives the location of the 7.6 Magnitude earthquakes that occurred on November 24, 2016 in South America near the border of Peru and Brazil. The torsion balance is located near St. Louis, Missouri, represented by the red star.

Location	*Date*	*Time (UCT)*	*Magnitude*	*Depth (km)*
173km WNW of Iberia, Peru	24 Nov 2015	22:45:38	7.6	606.2
211km S of Tarauaca, Brazil	24 Nov 2015	22:50:54	7.6	620.6

Table 6.2: Summary of the large magnitude earthquakes that were observed by the instrument as provided by the USGS online database [10].

which have triggered normal mode oscillations of the earth detected by previous observations. Information about the locations, timing, and magnitude of these events was obtained via the U.S. Geological Survey (USGS) online database [10].

These earthquakes occurred on November 24, 2015; the first occurred 173 km west-northwest of Iberia, Peru (10.537°S 70.944°W) at local time 16:45:54 CST (22:45:38 UTC), the second was located 211 km south of Tarauaca, Brazil (10.060°S 71.018°W) and occurred

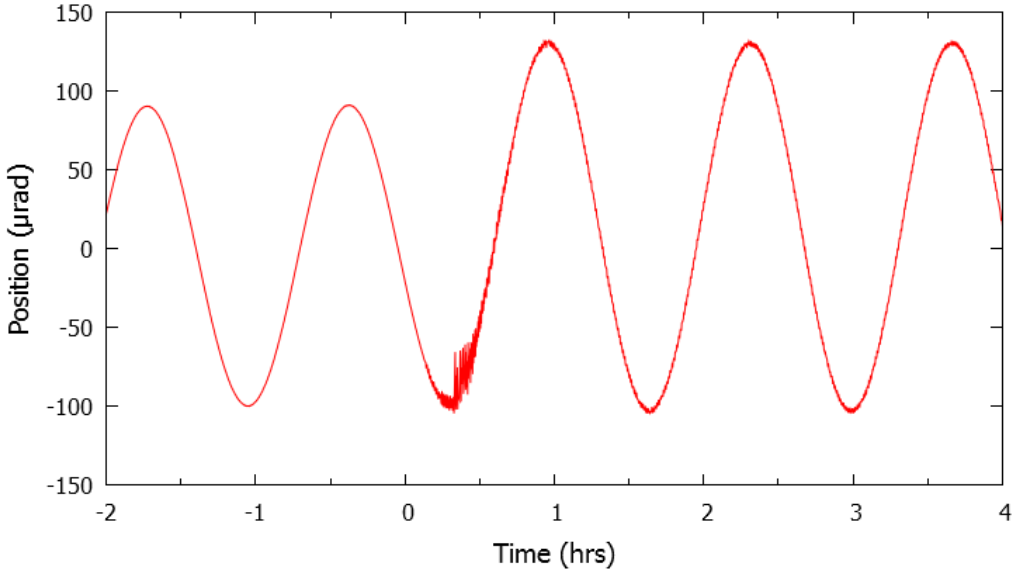

Figure 6.4: The balance position with a linear drift removed during the 7.6 magnitude earthquakes in South America on November 24, 2015. Here $t = 0$ corresponds to 16:45:54 CST, the time that the earthquake occurred.

five minutes later, at 16:50:54 CST (22:50:54 UTC). The initial response of the balance occurs about 8 minutes after the first event occurred, as shown in Figures 6.4 and 6.5. This event occurred a little less than 6000 km from the instrument, at a depth of 606.2 km.

In Figure 6.4 the balance position is shown for a span of several hours around the time the earthquakes occurred ($t = 0$). The high frequency response, which arises from pendular motion and wobble of the balance, is apparent in this plot as the thickening of the red line denoting balance position. In an ideal set up the autocollimator is not sensitive to swinging of the balance. While significant efforts were made to align the autocollimator with the optic axis in the vertical direction, some amount of tilt is unavoidable, leading to a coupling between these other modes and the rotational detection scheme. It may also be

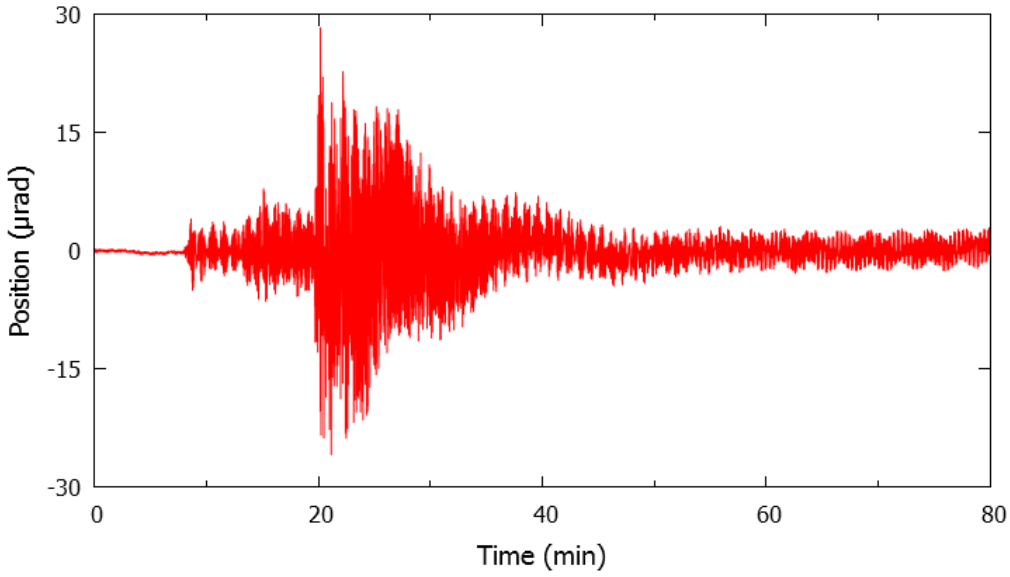

Figure 6.5: The balance position with during the 7.6 magnitude earthquakes in South America on November 24, 2015 after applying a high-pass filter to remove torsional oscillations and long term drifts. Again $t = 0$ corresponds to the time when the earthquake occurred.

noted that the energy generated from the earthquake increased the amplitude of the torsional oscillations as well.

By looking more closely at the balance response in the time domain, with torsional oscillations and low frequency drifts removed using a high-pass filter, the timing of various balance responses becomes clear. Figure 6.5 shows that the initial response occurs at about 479 seconds after the first event, with subsequent shocks about 319 seconds and 698 seconds later. While the pendular damping system is effective at quickly reducing the pendular motion of the balance, some amount persists for several hours.

The amplitude spectral density of the balance position for 36 hour segments before and after the earthquakes is shown in Figure 6.6, with an enlarged view of the normal mode

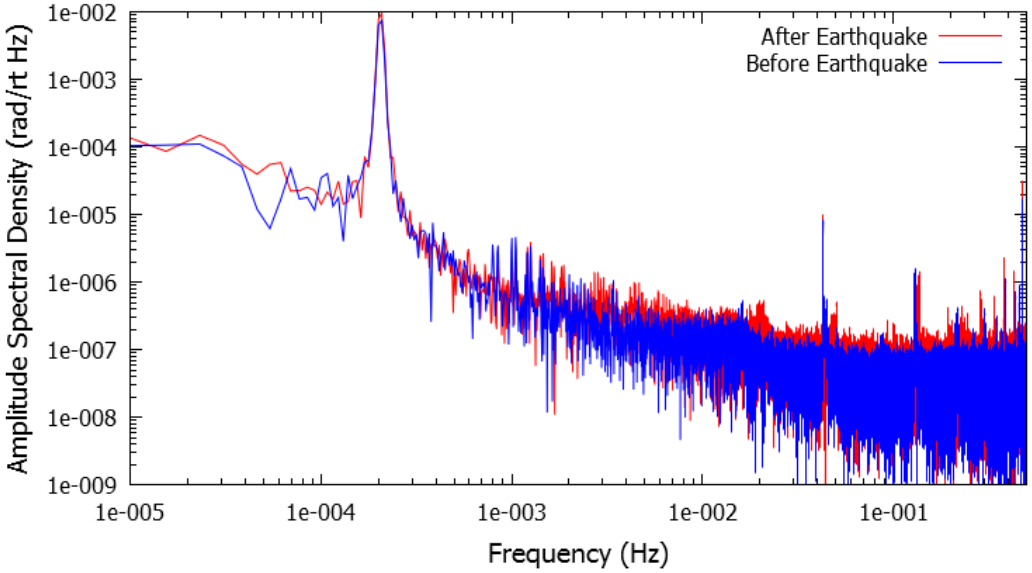

Figure 6.6: Amplitude Spectral Density of the balance position for 36 hour segments before (in blue) and after (in red) the South America 7.6 magnitude earthquakes. The energy at high frequencies in much greater immediately after the earthquake, but reduces as the pendular motions of the balance are damped.

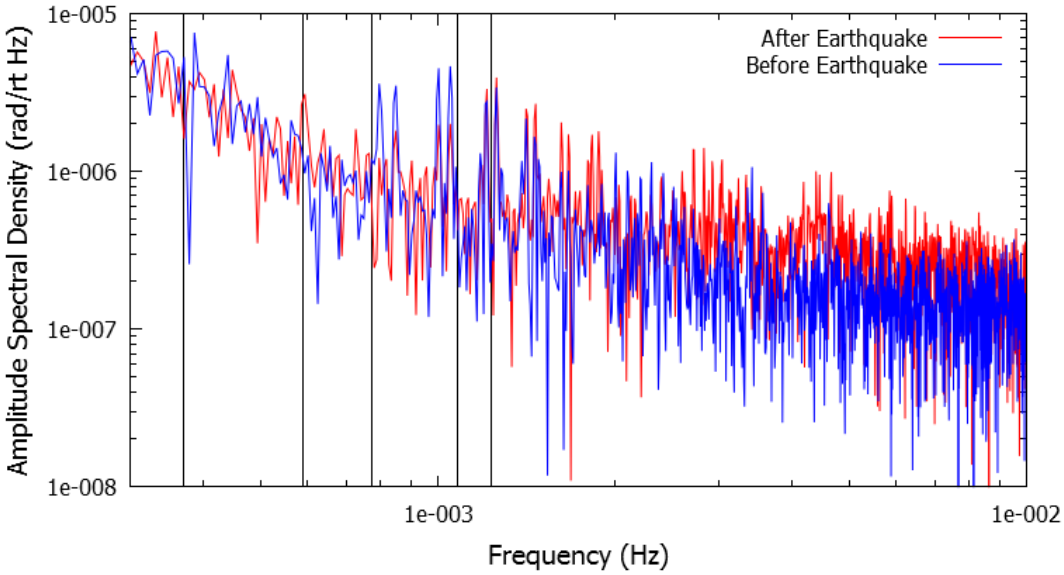

Figure 6.7: An enlarged view of Figure 6.6 around the mHz region where the gravest torsional normal modes should appear. Vertical lines denote the frequencies of modes given in Table 6.1.

frequency range in Figure 6.7. As expected the amount of energy in the system at high frequencies is much higher following the earthquakes. This is even more apparent for segments shorter that what is shown here. At ∼mHz frequencies the implications of the Fourier transform are less clear. The peaks that appear in pairs in the region both before and after the earthquakes are present throughout the data runs whenever the amplitude of torsional oscillations is above several pixels ($\gtrsim 50\,\mu$rad). The origin of these peaks is not currently understood, but it is suspected that they are the result of aliasing of a high frequency signal, an artifact of the Fourier transform process, or perhaps a signal from a coupled mode (see Appendix A). There does not seem to be evidence of detectable driving signals at the frequencies of the gravest torsional normal modes, which are shown by vertical lines in Figure 6.7, however it is known that these rotations are quite small even for earthquakes much larger than these events.

Observations of additional earthquakes, particularly events with larger magnitudes, are needed. It is worth noting that a 7.8 magnitude earthquake off the coast of Sumatra, Indonesia occurred at 07:49:48 CST (12:49:48 UTC) on March 2, 2016, during the Winter 2016 data run. This event, which was at a depth of only 24.0 km, was not detected in the torsion balance position data. It is also important to develop an understanding of the pairs of peaks seen in the mHz region of the balance frequency domain. Whether these are only artifacts in the data, or are caused by some peculiarity of the instrument itself they may be problematic when looking for the signals expected from the Earth's torsional normal mode oscillations.

Chapter 7

Conclusion

Significant progress has been made in the development of an experiment to test the equivalence principle and search for the torsional normal modes of the Earth taking a novel approach. The primary efforts of this work are summarized below. Furthermore, the knowledge and experience gained from operating this prototype instrument have provided an improved understanding of many of the random and systematic effects plaguing the experiment. A list of upgrades that promise to alleviate major hindrances in reaching unprecedented sensitivities with the experiment on both the gravitation and seismic fronts is also discussed.

7.1 Summary of Advances

This work has described the advances achieved in the development of a sensitive torsion balance experiment which aims to both test the equivalence principle and to directly detect the normal mode torsional oscillations of the Earth. Efforts were directed towards three

primary objectives. First, a complete model of the signal expected from a torsion balance configured as a composition dipole operating in the solar gravitational field in the case of an equivalence principle violation was developed. In this approach, the response of the balance to the gravitational field of the Sun is monitored precisely, as the Earth's natural rotation provides a smooth modulation of the torque arising from any assumed level of violation of the equivalence principle. The second objective was to develop and characterize an instrument capable of measuring tiny angular deflections of a torsion balance. To satisfy the requirement of obtaining an extended data set, the monitoring device must also possess a large dynamic range. A multi-slit auto-collimating optical lever with an observation range of about 10 mrad and a resolution of about a nanoradian was developed and integrated to meet these requirements. The performance of this autocollimator was evaluated at low frequencies which are relevant to this experiment. Finally, the torsion balance itself was designed, built, and characterized by operating the instrument at a remote laboratory well-suited for this type of experiment. The balance is comprised of Al and SiO_2 test masses so it may search for a violation of the universality of free fall between these materials. It has a natural period significantly below the lowest frequency of the Earth's torsional normal modes for maintaining sensitivity to these free oscillations. More than 1800 hours of data were collected with the balance in operation to characterize the instrument, evaluate its performance, and identify avenues for improvement in a next generation instrument. Many of the these proposed upgrades are presented below.

7.2 Design of a Next Generation Instrument

The experience and knowledge gained by operating this instrument has illustrated a number of areas in which a new design, improved engineering, or different approach would benefit the experiment. In many cases, problems were identified and addressed and have been discussed in this thesis. Restrictions in time and funding have left other issues to be addressed by a future version of the instrument. The upgrades that promise to offer the most significant advances include the implementation of a reference image setup to remove low frequency drifts in the optics, the eradication of pressure bursts and stick-slip events that disrupt the balance's equilibrium position, the replacement of the torsion fiber with a longer, relatively free-of-drift torsion strip, and the installation of external magnetic shielding, a more well-engineered balance, and a long-term back up power supply for the Tyson bunker laboratory.

7.2.1 Reference Image Autocollimator Arrangement

It is inevitable that the autocollimator readout will include motions other than the deflection of the suspended balance. While the design of an auto-collimating optical lever significantly reduces its sensitivity to thermal variations, some amount of temperature dependence exists. In addition, thermally driven changes in the curvature of the gimbal mirror and slight expansion and contraction of the aluminum support structure contribute to the readout position. Based on comparisons of the averaged position and temperature data presented in § 5.5 for the Fall 2015 and Winter 2016 data runs, these effects seem quite significant in

the prototype instrument. To confirm this suspicion, following the Winter 2016 data run the gimbal mirror was adjusted to image the portion of the autocollimator image that is reflected off the vacuum chamber optical port. This image was tracked for a few weeks, and the result, plotted in Figure 7.1, shows a seemingly random low frequency drift along with a discernible diurnal drift which is of comparable magnitude to the variation seen in the averaged daily balance position as measured by the autocollimator (Figure 5.13). As mentioned previously, one proposed approach for removing drifts which are associated with the optics or support structure, rather than the balance, is the use of a reference image. Such an approach has been implemented recently by the Eöt-Wash group, and has been shown to reduce noise caused by thermal fluctuations and other troubling effects in the autocollimator and relevant optics [68, 101]. Using the autocollimator schematic diagram previously shown in § 3.2, the concept of this set up is illustrated in Figure 7.2.

By subtracting the centroid value x_R obtained for an image reflected off of a fixed reference mirror M_R from the centroid value x_c obtained from a target mirror M_2 on the torsion balance, unwanted drift of the autocollimator readout which is not related to the position of the balance is reduced. With particular interest in improving low frequency resolution, this scheme was tested using two flat mirrors slightly offset, and tilted by several milliradians with respect to each other. The image produced in this reference beam setup is shown in Figure 7.3.

The improvement that the reference mirror setup offers is illustrated by a plot of the centroid position of stationary target and reference mirrors and the difference between them

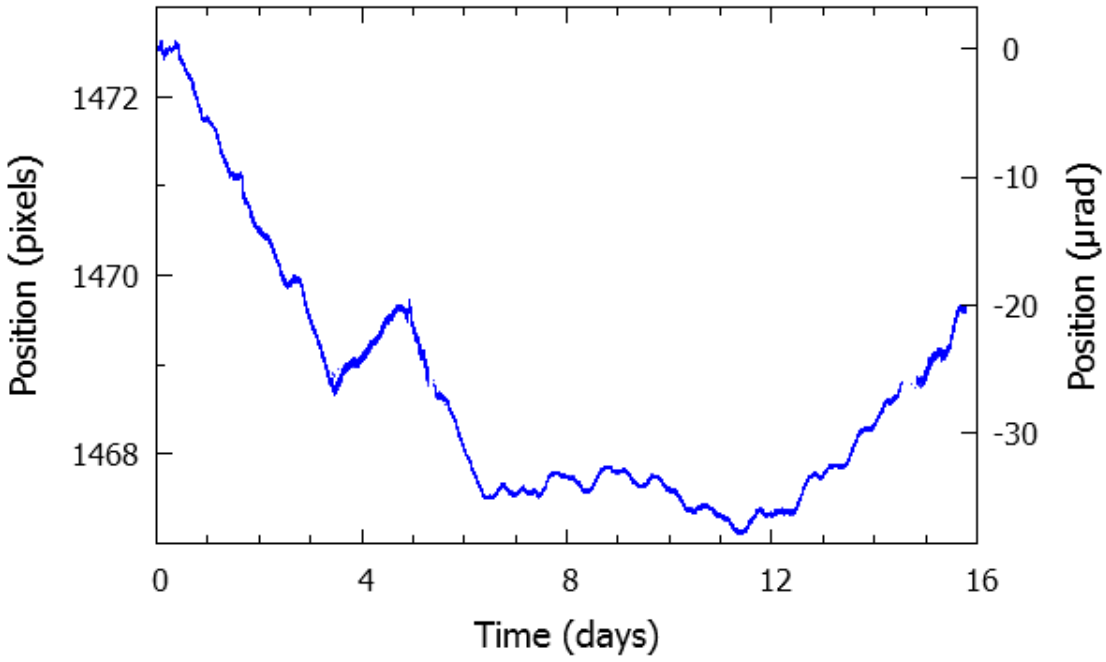

Figure 7.1: Position of autocollimator image reflected off the vacuum chamber optical port. Given in terms of autocollimator CCD pixel number as well as µrad from the initial position.

in Figure 7.4. For successful integration with the experiment, a reference mirror should be located near the balance mirror so that both images can be well focused simultaneously. For practical reasons the orientation of the target mirror should also be adjustable with minimal disruption to the experiment. Ideally this reference mirror would be secured from a location in close proximity to the point from which the torsion fiber is attached to the top of the chamber. For the system currently in use, securing this reference mirror from the inner side of the optical port could be accomplished with minimal modifications to the current experiment.

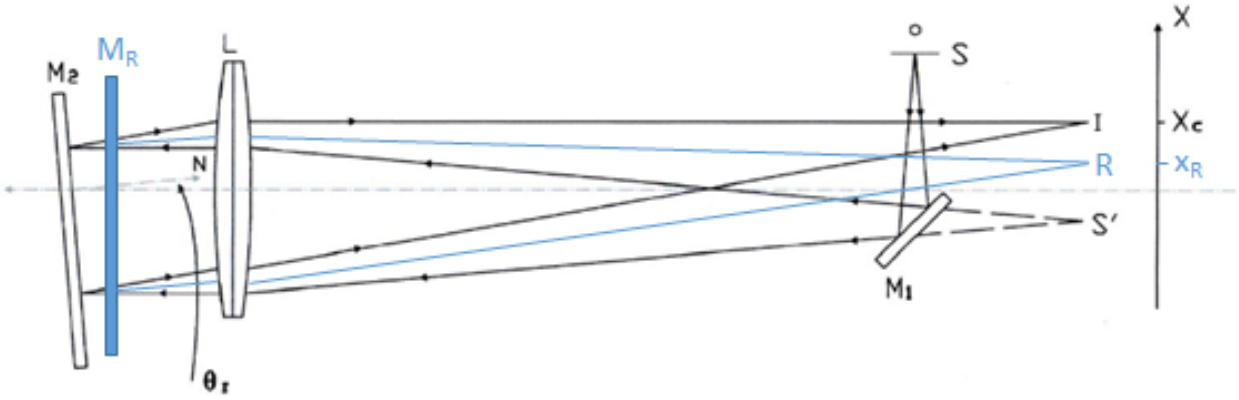

Figure 7.2: Schematic diagram of the reference image set up for the autocollimator. The light blue lines represent the path followed by the image reflected off the reference mirror M_R.

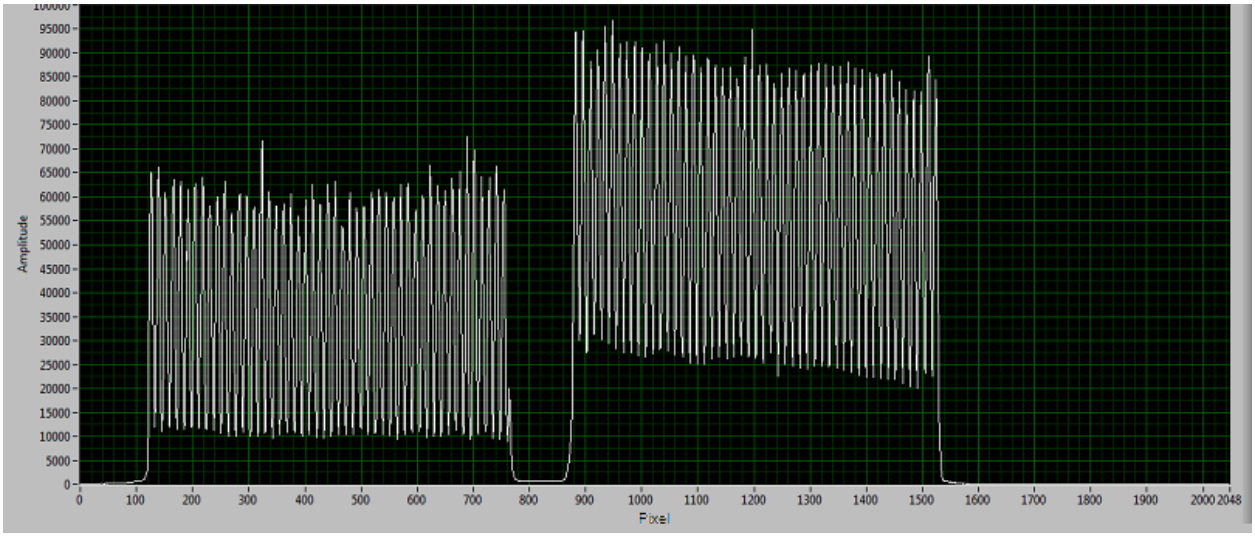

Figure 7.3: Image recorded by the autocollimator during testing of the reference mirror scheme. Intensity is shown in the vertical direction, while pixel number is given in the horizontal direction. The array of 50 peaks on the left is the image reflected off the target mirror, while the image from the reference mirror is on the right.

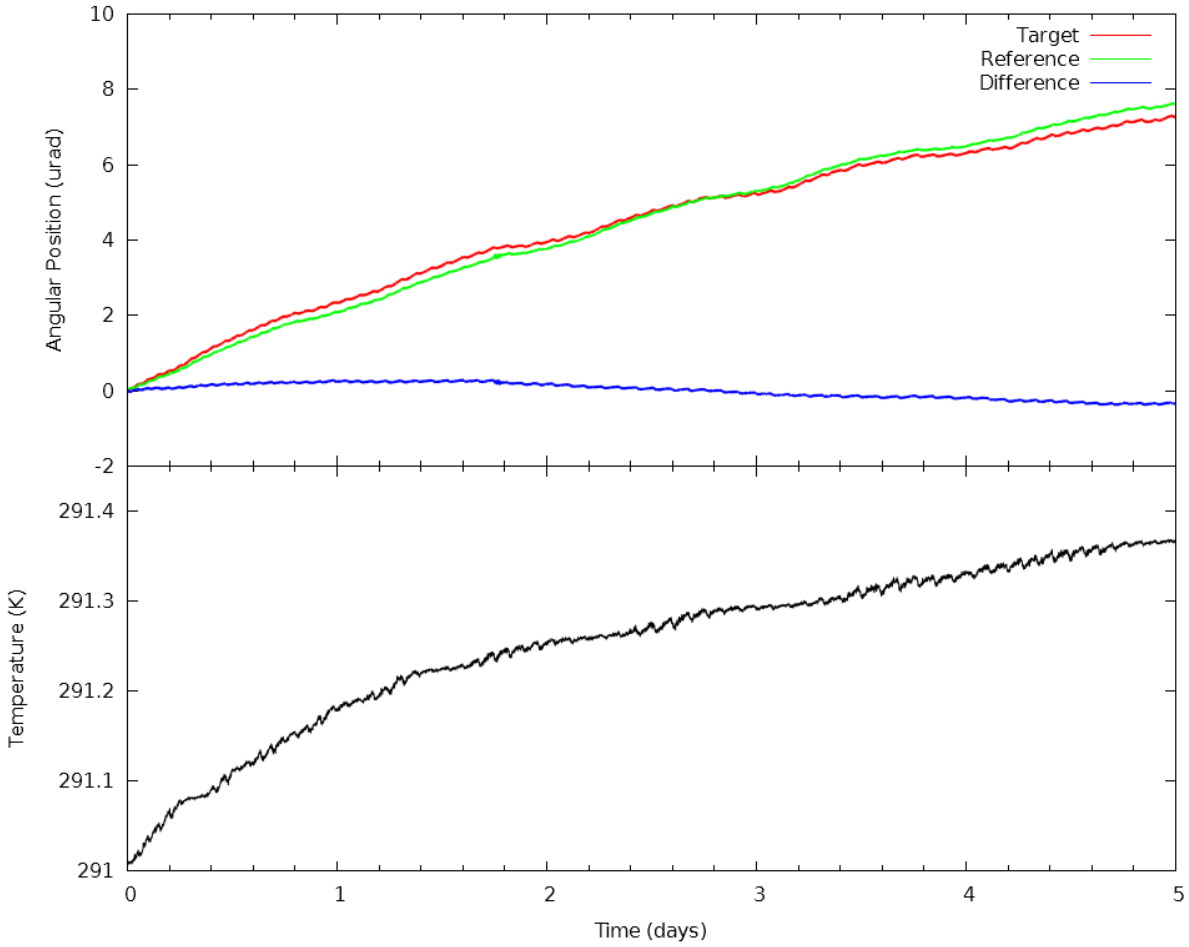

Figure 7.4: (Top) Centroid data recorded by the autocollimator in the reference mirror set up. Shown are the position from the target mirror (in red), reference mirror (in green), and the difference between the two images (in blue). This illustrates the reduction of readout drift possible by the implementation of a reference image.
(Bottom) Temperature data recorded in the laboratory during this time interval. The ∼2 hour signal that shows up in the temperature and position plots was due to the cycling of a dehumidifier that was running in the same room as the autocollimator.

7.2.2 Elimination of Internal Balance Disruptions

Another area where improvement is possible is the elimination of pressure bursts and the stick-slip processes that lead to sudden shifts of the equilibrium position of the balance. As discussed in § 4.3.1 and § 5.1, these pressure bursts have been referred to as glitches when they noticeably affect the amplitude and phase of the torsional oscillations (these events are caused by pressure bursts at the o-ring seal around the optical port which is close to one of the mirrored SiO_2 test masses). Even bursts that do not appear to effect the torsional oscillations of the balance have been shown to cause a brief displacement of the equilibrium position when consulting the filtered position data, thus introducing noise to the system. Based on the explanation laid out in § 4.3.1 involving rubber o-ring seals and vacuum grease, as well as the absence of these spikes in a separate torsion balance experiment under development at Washington University which uses copper gaskets to seal the vacuum chamber, it is expected that by replacing the rubber o-rings used to seal the chamber with metal o-rings, these pressure spikes can be eliminated.

The other type of disruption to be addressed is the sudden shifts in equilibrium position of the balance that occurred throughout the Fall 2015 and Winter 2016 data runs. It is believed that these events are the result of a sudden slippage, or the relieving of stress, of some part of the suspension system. While it is not certain where this release occurs, the most likely locations are the points where the torsion fiber is secured to the top of the suspension system or the threaded rod that attaches to the torsion balance. In the latter

case, the size of the 25 µm diameter fiber required that it was wrapped with a small piece of foil to be securely clamped in place. Alternative means of securing the balance to the fiber, or the top of the fiber to the rest of the suspension system may be required to eliminate this slippage. One alternative approach, which has been implemented elsewhere, would be to crimp the fiber inside of a small metal tube which is attached to the rod supporting the balance.

7.2.3 Torsion Strip of Extended Length

Replacing the circular cross section Tungsten torsion fiber with a torsion strip of rectangular cross section is currently being considered for a number of reasons, but the most compelling point is the significant reduction in fiber drift that has been observed by the torsion balance test of short range gravity under development in-house. This instrument uses a stainless steel torsion strip with a cross section of 7 µm × 110 µm. Operating a balance with minimal drift would be advantageous in obtaining the desired year-long continuous data run for a next generation experiment to test the equivalence principle. About a month of data showing the equilibrium position of the short range gravity experiment balance is shown in Figure 7.5.

The torsion constant of a torsion strip κ_s is given by

$$\kappa_s = \frac{\mu x^3 y}{3l} \tag{7.1}$$

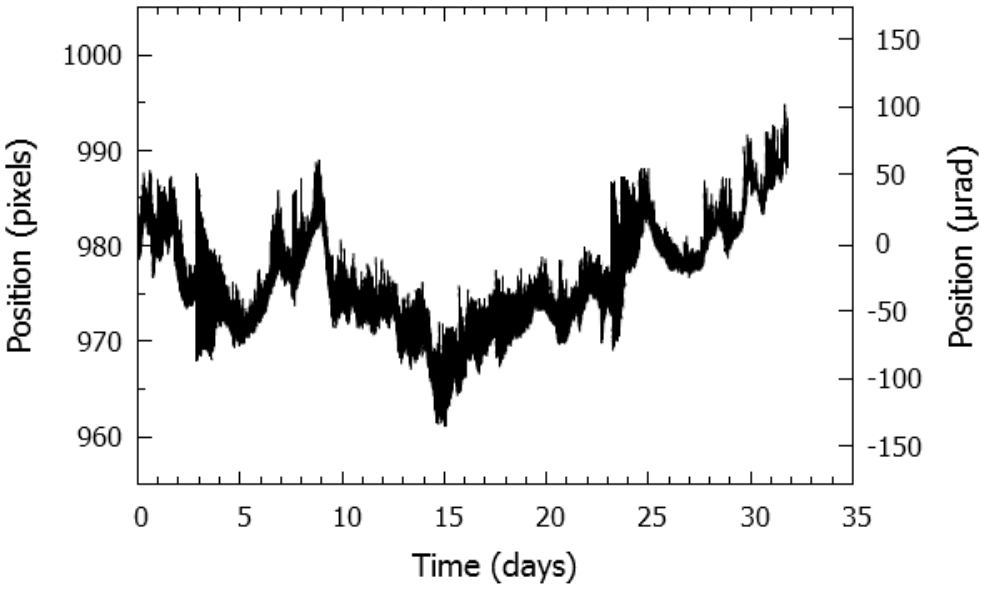

Figure 7.5: The equilibrium position of a separate balance currently under development in the GEE Lab at Washington University which employs a torsion strip with a rectangular cross section. While a large amount of noise from the instrument and laboratory is present in this signal, the minimal amount of long term drift in the torsion strip is the key point illustrated here.

where x and y are the smaller and larger cross section dimensions, respectively, and as before, μ is the modulus of rigidity of the torsion strip material, and l is the length of the strip. The amount of mass that a torsion strip can support is also dependent on the cross sectional area of the strip, however, by making the x dimension of the fiber very small, a torsion strip can provide a much smaller restoring torque compared to a torsion fiber, thus increasing the deflection of a balance θ resulting from a given torque τ. Among with other benefits, Quinn et al. have found these reasons for using torsion strips for torsion balance measurements of the Newtonian constant of gravitation G [102–104].

The additional benefit of using a longer suspension fiber was mentioned in § 3.3.3, and is

apparent from Equation (7.1). When designing the experiment support frame, the possibility of adding an extension to the top of the vacuum chamber to increase the length of the fiber l to $\sim$2 m was kept in mind, thus such a modification would be very straightforward at this point.

There is some concern about the coupling of ground tilts and balance position, particularly for a balance suspended from a torsion strip. While the circular cross section of the pre-hanger suspension fiber helps to reduce this coupling, it may be important to monitor ground tilt and account for this effect in a formal analysis of data obtained from an experiment using a torsion strip.

7.2.4 External Magnetic Shielding

The need for magnetic shielding, as well as efforts to implement shielding made from sheets of mu-metal surrounding the prototype balance and located inside of the vacuum chamber, was discussed in § 4.5. While strong attraction between the balance and the mu-metal shielding prevented the success of this approach, shielding the torsion balance from the effects of external magnetic fields remains a crucial aspect of a future version of this instrument. Currently, a plan for encasing the main bell jar portion of the vacuum chamber with a layer of mu-metal is in the works. If possible, employing multiple layers would be preferable.

7.2.5 New Balance

The total mass of a torsion balance is limited by, among other factors, the tensile strength of the fiber suspending the balance, while the deflection of the balance resulting from a violation of the equivalence principle depends on the mass of the test masses and their distance from the center of the balance. With this in mind the balance was designed to have a large radius and to be built so that the test masses make up as much of the total mass of the balance as possible (about 75% in the prototype balance). The balance relies on a 4-fold geometric symmetry to reduce its sensitivity to local gravitational gradients. Thus asymmetries of the balance, such as the lengths of balance arms, masses of the test masses, and precise direction of the through hole in the center of the balance, may lead to problematic gravitational coupling to local fields. Massive objects in the vicinity of the instrument should be used to quantify this coupling and provide confidence that measurements are not effected by local gravitational fields. In addition, care was taken to prevent obvious magnetic contamination during the construction of the balance, yet completely avoiding ferrous sources seems unlikely given the machining conditions available at this time. Access to superior engineering capabilities would be desirable for avoiding each of these concerns in the construction of an ideal balance.

An additional concern arises from the potential of electrostatic effects. To eliminate work function differences between the balance and nearby surfaces which can lead to electrostatic coupling, the balance (and these surfaces) should be gold coated.

7.2.6 Backup Power Supply

A final improvement desired for the next generation experiment is a reliable backup power supply capable of powering the experiment (at minimum the computer, autocollimator, and ion pump) in the case of a power outage lasting several days. Lengthy power outages have been more problematic than anticipated at the Tyson bunker laboratory. While the remote location of the laboratory is well suited for a sensitive torsion balance experiment, it also means that expedient restoration of power is not a high priority.

The experiment is currently connected to an uninterruptible power supply (UPS), however this battery backup only lasts for a few hours and is not a suitable solution for power outages lasting for multiple days. Both the Fall 2015 and Winter 2016 data runs were halted by power outages. Once the ion pump has been off for a few days, the pressure inside the chamber rises to the point that the roughing and turbo pumps need to be used to return the chamber to high vacuum. This disrupts the balance and leads to downtime of a week or two before the instrument is aligned, damped, and collecting data again. To avoid these breaks in data collection so that an extended continuous data run may be obtained, a stand-alone power system that can immediately support the power needs of the experiment during an electrical outage will be necessary.

Bibliography

[1] P. G. Roll, R. Krotkov, and R. H. Dicke. The equivalence of inertial and passive gravitational mass. *Annals of Physics*, 26:442–517, 1964.

[2] V. B. Braginsky and V. I. Panov. Verification of the equivalence of inertial and gravitational mass. *JETP*, 61(3), 1972.

[3] T. A. Wagner, S. Schlamminger, J. H. Gundlach, and E. G. Adelberger. Torsion-balance tests of the weak equivalence principle. *Class. Quantum Grav.*, 29(184002), 2012.

[4] R. Cowsik, R. Srinivasan, S. Kasturirengan, A. Senthil Kumar, and K. Wagoner. Design and performance of a sub-nanoradian resolution autocollimating optical lever. *Rev. Sci. Instrum.*, 78(035105), 2007.

[5] R. Cowsik. An instrument for direct observations of seismic and normal-mode rotational oscillations of the earth. *PNAS*, 104(17):6893–6898, 2007.

[6] Ramanath Cowsik, Tsitsi Madziwa-Nussinov, Kasey Wagoner, Douglas Wiens, and Michael Wysession. Performance characteristics of a rotational seismometer for near-field and engineering applications. *Bull. Seismol. Soc. Am.*, 99(2B):1181–1189, May 2009.

[7] Weather underground website. www.wunderground.com/history/.

[8] Thibault Damour. Theoretical aspects of the equivalence principle. *Class. Quantum Grav.*, 29(184001), Feb 2012.

[9] Y. T. Chen and Alan Cook. *Gravitational Experiments in the Laboratory.* Cambridge University Press, 1993.

[10] U.s. geological survey online database. earthquake.usgs.gov/earthquakes/map/.

[11] A. Einstein. On the relativity principle and the conclusions drawn from it. *Jahrbuch der Radioaktivität und Elecktronik*, 4:411–462, 1907.

[12] S. Weinberg. *Gravitation and Cosmology.* John Wiley & Sons, New York, 1972.

[13] Clifford M. Will. *Theory and experiment in gravitational physics.* Cambridge University Press, 1993.

[14] L. I. Schiff. On experimental tests of the general theory of relativity. *Am. J. Phys.*, 28(340), 1960.

[15] R. H. Dicke. *Relativity, Groups and Topology.* Gordon & Breach, New York, 1964.

[16] K. Nordtvedt. Quantitative relationship between clock gravitational redshift violations and non-universality of free-fall rates in non-metric theories of gravity. *Phys. Rev. D*, 11:245–7, 1975.

[17] M. P. Haugan. Energy conservation and the principle of equivalence. *Ann. Phys. (N. Y.)*, 118:156–86, 1979.

[18] Albert Einstein. The foundation of the general theory of relativity. *Annalen der Physik*, 49(7):769–822, 1916.

[19] F. W. Dyson, A. S. Eddington, and C. Davidson. A determination of the deflection of light by the sun's gravitational field, from observations made at the total eclipse of 29 may 1919. *Philos. Trans. Roy. Soc. London*, 220A:291–333, 1920.

[20] R. V. Pound and G. A. Rebka Jr. Gravitational red-shift in nuclear resonance. *Phys. Rev. Lett.*, 3(9):439–441, November 1959.

[21] E. B. Fomalont, S. M. Kopeikin, G. Lanyi, and J. Benson. Progress in measurements of the gravitational bending of radio waves using the vlba. *Astrophys. J.*, 699(2):1395–1402, July 2009.

[22] R. F. C. Vessot, M. W. Levine, E. M. Mattison, E. L. Blomberg, T. E. Hoffman, G. U. Nystrom, B. F. Farrel, and et al. R. Decher. Test of relativistic gravitation with a space-borne hydrogen maser. *Phys. Rev. Lett.*, 45(26):2081–2084, December 1980.

[23] I. I. Shapiro, M. E. Ash, R. P. Ingalls, W. B. Smith, D. B. Campbell, R. B. Dyce, R. F. Jurgens, and G. H. Pettengill. Fourth test of general relativity: New radar result. *Physical Review Letters*, 26(18):1132–1135, May 1971.

[24] C. W. F. Everitt and et al. Gravity probe b: Final results of a space experiment to test general relativity. *Physical Review Letters*, 106(22), 2011.

[25] J. M. Weisberg, D. J. Nice, and J. H. Taylor. Timing measurements of the relativistic binary pulsar psr b1913+16. *Astrophys. J.*, 722:1030–1034, 2010.

[26] B. P Abbott and et al. Observation of gravitational waves from a binary black hole merger. *Phys. Rev. Lett.*, 116(6), February 2016.

[27] P. J. E. Peebles. Probing general relativity of the scales of cosmology. *arXiv:astro-ph/0410284v1*, October 2004.

[28] Thibault Damour. Testing the equivalence principle: why and how? *Class. Quantum Grav.*, 13:A33–A41, 1996.

[29] T. Appelquist, A. Chodos, and P. G. O. Freund. *Modern Kaluza-Klein Theories*. Addison-Wesley, Menlo Park, California, 1987.

[30] P. A. M. Dirac. The cosmological constants. *Nature*, 139(323), 1937.

[31] P. Jordan. Naturwissenschaften. *Z. Phys.*, 113(660), 1939.

[32] M. Fierz. *Helv. Phys. Acta*, 29(128):128–134, 1956.

[33] T. Damour and A. M. Polyakov. The string dilaton and a least coupling principle. *Nucl. Phys. B*, 423:532–558, 1994.

[34] T. Dent. Eotvos bounds on couplings of fundamental parameters to gravity. *Phys. Rev. Lett.*, 101(041102), 2008.

[35] T. Damour and J. F. Donoghue. Phenomenology of the equivalence principle with light scalars. *Class. Quant. Grav.*, 27(202001), 2010.

[36] T. Damour and J. F. Donoghue. Equivalence principle violations and couplings of a light dilaton. *Phys. Rev. D*, 82(084033), 2010.

[37] Virginia Trimble. Existence and nature of dark matter in the universe. *Ann. Rev. Astron. Astrophysics*, 25:425–72, 1987.

[38] Scott Tremaine. The dynamical evidence for dark matter. *Physics Today*, 45(2), 1992.

[39] X. Wu, T. Chiueh, L. Fang, and Y. Xue. A comparison of different cluster mass estimates: consistency or discrepancy? *Mon. Not. R. Astron. Soc.*, 301(3):861–871, 1998.

[40] F. Zwicky. On the masses of nebulae and of clusters of nebulae. *Astrophys. J.*, 86(217), 1937.

[41] V. Springel and et al. Simulating the joint evolution of quasars, galaxies and their large-scale distribution. *Nature*, 435(7042):629–636, 2005.

[42] G. Hinshaw and et al. Five-year wilkinson microwave anisotropy probe (wmap) oobservation: Data processing, sky maps, and basic results. *The Astrophysical Journal Supplement*, 180(2):225–245, 2009.

[43] N. Jarosik, C. L. Bennett, J. Bennett, J. Dunkley, B. Gold, and et al. Seven-year wilkinson microwave anisotropy probe (wmap) observations: Sky maps, systsystem errors, and basic results. *Astrophys. J. Suppl. Ser.*, 192(14), 2011.

[44] Gary Steigman and Michael S. Turner. Cosmological constants on the properties of weakly interacting massive particles. *Nucl. Phys. B*, 253:375–386, 1985.

[45] John Preskill, Mark B. Wise, and Frank Wilczek. Cosmology of the invisible axion. *Phys. Lett. B*, 120(13):127–132, 1983.

[46] Christopher W. Stubbs. Experimental limits on any long range nongravitational interaction between dark matter and ordinary matter. *Physical Review Letters*, 70(2):119–122, 1993.

[47] S. Schlamminger, K. Y. Choi, T. A. Wagner, J. H. Gundlach, and E. G. Adelberger. Test of the equivalence principle using a rotating torsion balance. *Phys. Rev. Lett.*, 100(041101), 2008.

[48] Adam G. Riess, Alexei V. Filippenko, Peter Challis, Alejandro Clocchiattia, Alan Diercks, Peter M. Garnavich, Ron L. Gilliland, Craig J. Hogan, Saurabh Jha, Robert P. Kirshner, B. Leibundgut, M. M. Phillips, David Riess, Brian P. Schmidty, Robert A.

Schommer, R. Chris Smith, J. Spyromilio, Christopher Stubbs, Nicholas B. Suntzeff, and John Tonry. Observational evidence from supernovae for an accelerating universe and a cosmological constant. *Astronomical Journal*, 116(3):1009–38, 1998.

[49] S. Perlmutter, G. Aldering, G. Goldhaber, R. A. Knop, P. Hugent, P. G. Castro, S. Deustua, S. Fabbro, A. Goobar, D. E. Groom, I. M. Hook, A. G. Kim, M. Y. Kim, J. C. Lee, N. J. Nunes, R. Pain, C. R. Pennypacker, R. Quimby, C. Lidman, R. S. Ellis, M. Irwin, R.G. McMahon, P. Ruiz-Lapuente, N. Walton, B. Schaefer, B. J. Boyle, A. V. Filippenko, T. Matheson, A. S. Fruchter, H. J. M. Newberg, and W. J. Couch. Measurements of omega and lambda from 42 high-redshift supernovae. *Astrophys. J.*, 517(2):565–86, 1999.

[50] Sean M. Carroll. Quintessence and the rest of the world: Suppressing long-range interactions. *Phys. Rev. Lett.*, 81(15):3067–3070, 1998.

[51] Sean M. Carroll, William H. Press, and Edwin L. Turner. The cosmological constant. *Annu. Rev. Astron. Astrophys.*, 30(499), 1992.

[52] E. G. Adelberger, C. W. Stubbs, B. R. Heckel, Y. Su, H. E. Swanson, G. Smith, and J. H. Gundlach. Testing the equivalence principle in the field of the earth: Particle physics at masses below 1 μev? *Phys. Rev. D: Part. Fields*, 42(10):3267–3292, November 1990.

[53] Y. Su. *A New Test of the Weak Equivalence Principle*. PhD thesis, University of Washington, 1992.

[54] Y. Su, , B. R. Heckel, E. G. Adelberger, J. H. Gundlach, M. Harris, G. L. Smith, and H. E. Swanson. New tests of the universality of free fall. *Phys. Rev. D: Part. Fields*, 50:3614–3636, 1994.

[55] Todd A. Wagner. *Rotating Torsion Balance Tests of the Weak Equivalence Principle*. PhD thesis, University of Washington, 2013.

[56] T. W. Murphy. Lunar laser ranging: the millimeter challenge. *Rep. Prog. Phys.*, 76(076901), June 2013.

[57] J. G. Williams, S. G. Turyshev, and D. H. Boggs. Lunar laser ranging tests of the equivalence principle with the earth and moon. *Int. J. Mod. Phys. D*, 18:1129–75, 2009.

[58] J. G. Williams, S. G. Turyshev, and D. H. Boggs. Lunar laser ranging tests of the equivalence principle. *Class. Quantum Grav.*, 29(184004), 2012.

[59] J. Müller, F. Hofmann, and I. Biskupek. Testing various facets of the equivalence principle using lunar laser ranging. *Class. Quantum Grav.*, 29(184006), 2012.

[60] Joel Bergè, Pierre Touboul, and et al. Manuel Rodrigues. Status of microscope, a mission to test the equivalence principle in space. *arXiv*, (1501.01644v1), Jan 2015.

[61] eoportal directory. https://directory.eoportal.org/web/eoportal/satellite-missions/m/microscope#references.

[62] James Overduin, Francis Everitt, Paul Worden, and John Mester. Step and fundamental physics. *arXiv*, (1401.4784v1), Jan 2014.

[63] Robert D. Reasenberg, Biju R. Patla, James D. Philips, and Rajesh Thapa. Design and characteristics of a wep test in a sounding-rocket payload. *Class. Quantum Grav.*, 29(184013), 2012.

[64] Jpl horizons webpage. ssd.jpl.nasa.gov/?horizons.

[65] Stephen T. Thornton and Jerry B. Marion. *Classical Dynamics of Particles and Systems*. Brooks Cole, 5 edition, 2003.

[66] E. G. Adelberger, J. H. Gundlach, B. R. Heckel, S. Hoedl, and S. Schlamminger. Torsion balance experiments: A low-energy frontier of particle physics. *Prog. Part. Nucl. Phys.*, 62(102), 2009.

[67] Riley Newman, Michael Bantel, Eric Berg, and William Cross. A measurement of g with a cryogenic torsion pendulum. *Philos. Trans. Roy. Soc. London*, 372(20140025), 2014.

[68] T. B. Arp, C. A. Hagedorn, S. Schlamminger, and J. H. Gundlach. A reference-beam autocollimator with nanoradian sensitivity from mhz to khz and dynamic range of 10(7). *Rev. Sci. Instrum.*, 9(095007), 2013.

[69] Krishna Venkateswara, Charles A. Hagedorn, Matthew D. Turner, Trevor Arp, and Jens H. Gundlach. A high-precision mechanical absolute-rotation sensor. *Rev. Sci. Instrum.*, 85(015005), 2014.

[70] Byron D. Tapley, Srinivas Bettadpur, John C. Ries, Paul F. Thompson, and Michael M. Watkins. Grace measurements of mass variability in the earth system. *Science*, 305:503–505, July 2004.

[71] H. Nyquist. Thermal agitation of electric charge in conductors. *Physical Review*, 32, July 1928.

[72] Herbert B. Callen and Theodore A. Welton. Irreversibility and generalized noise. *Physical Review*, 83(1), July 1951.

[73] Herbert B. Callen and Richard F. Greene. On a theorem of irreversible thermodynamics. *Physical Review*, 86(5), June 1952.

[74] Peter R. Saulson. Thermal noise in mechanical experiments. *Phys Rev D: Part Fields*, 42(8):2437–2445, October 1990.

[75] E. G. Adelberger, B. R. Heckel, and A. E. Nelson. Tests of the gravitational inverse-square law. *Ann. Rev. Nucl. Part. Sci.*, 53:77–121, 2003.

[76] B. P. Abbott, R. Abbott, R. Adhikari, P. Ajith, B. Allen, G. Allen, R. S. Amin, S. B. Anderson, and et al. Ligo: the laser interferometer gravitational-wave observatory. *Reports on Progress in Physics*, 72, 2009.

[77] T. J. Quinn, C. C. Speake, and L. M. Brown. Materials problems in the construction of long-period pendulums. *Phil. Mag. A*, 65:261–76, 1992.

[78] Gabriela I. González and Peter R. Saulson. Brownian motion of a mass suspended by an anelastic wire. *J. Acoust. Soc. Am.*, 96(96):207–212, July 1994.

[79] Kazuaki Kuroda. Does the time-of-swing method give a correct value of the newtonian gravitational constant? *Phys. Rev. Lett.*, 75(15):2796–2798, October 1995.

[80] C. C. Speake, T. J. Quinn, R. S. Davis, and S. J. Richman. Experiment and theory in anelasticity. *Meas. Sci. Technol.*, 10:430–434, 1999.

[81] Riccardo DeSalvo. Unaccounted source of systematic errors in measurements of the newtonian gravitational constant g. *Physics Letters A*, 379:1202–1205, 2015.

[82] Ying Tu, Liang Zhao, Qi Liu, Hong-Ling Ye, and Jun Luo. An abnormal mode of torsion pendulum and its suppression. *Phys. Lett. A*, 331:354–360, 2004.

[83] Xiang-Dong Fan, Qi Liu, Lin-Xia Liu, Vadim Milyukov, and Jun Luo. Coupled modes of the torsion pendulum. *Phys. Lett. A*, 372:547–552, 2008.

[84] G. Rajalakshmi. *Torsion Balance Investigation of the Casimir Effect.* PhD thesis, Bangalore University, May 2004.

[85] Kasey Wagoner. *Laboratory Investigations of Short Range Gravity.* PhD thesis, Washington University in St. Louis, 2010.

[86] Technical report, Kurt J. Lesker Company. https://www.lesker.com/newweb/technical_info/vacuumtech/pressure_03_cyclingbouncing.cfm?section=pressure.

[87] C. D. Hoyle, D. J. Kapner, B. R. Heckel, E. G. Adelberger, J. H. Gundlach, U. Schmidt, and H. E. Swanson. Submillimeter tests of the gravitational inverse-square law. *Phys. Rev. D*, 70(042004), 2004.

[88] S. E. Pollack, M. D. Turner, S. Schlamminger, C. A. Hagedorn, and J. H. Gundlach. Charge management for gravitational-wave observatories using uv leds. *Phys. Rev. D*, 81(021101(R)), 2010.

[89] Heiner Igel, Maria-Fernanda Nader, Dieter Kurrle, Ana M. G. Ferreira, Joachim Wassermann, and K. Ulrich Schreiber. Observations of earth's toroidal free oscillations with a rotation sensor: The 2011 magnitude 9.0 tohoku-oki earthquake. *Geophys. Res. Lett.*, 38(L21303), 2011.

[90] H. Lamb. Earth vibrations of an elastic sphere. *Proc. London Math. Soc.*, 13(189), 1882.

[91] Z. Alterman, H. Jarosch, and C. L. Pekeris. Oscillations of the earth. *Proceedings of the Royal Society A*, 252(1268), August 1959.

[92] Hugo Benioff, Frank Press, and Stewart Smith. Excitation of the free oscillations of the earth by earthquakes. *J. Geophys. Res.*, 66(2):605–619, February 1961.

[93] Adam M. Dziewonski and Don L. Anderson. Preliminary reference earth model. *Phys. Earth Planet. Inter.*, 25(4):297–356, June 1981.

[94] A. Castellani and Z. Zembaty. Comparison between earthquake rotation spectra obtained by different experimental sources. *Eng. Struct.*, 18(8):597–603, 1996.

[95] A. Cochard, H. Igel, B. Schuberth, W. Suryanto, A. Velikoseltsev, U. Schreiber, J. Wassermann, F. Scherbaum, and D. Vollmer. Rotational motions in seismology: theory, observation, simulation. *Earthquake source asymmetry, structural media and rotation effects*, 2006.

[96] N. Suda, K. Nawa, and Y. Fukao. Earth's background free oscillations. *Science*, 279(5359):2089–91, March 1998.

[97] Junkee Rhie and Barbara Romanowicz. Excitation of earth's continuous free oscillations by atmosphere-ocean-seafloor coupling. *Nature*, 431:552–556, September 2004.

[98] J. Park, A. Amoruso, L. Crescentini, and E. Boschi. Long-period toroidal earth free oscillations from the great sumatra-andaman earthquake observed by paired laser extensometers in gran sasso, italy. *Geophys. J. Int.*, 173:887–905, 2008.

[99] H. Igel, W. H. K. Lee, and M. I. Todorovska. Agu fall meeting 2006, rotational seismology sessions s22a and s23b. *Inauguration of the International Working Group on Rotational Seismology.*

[100] Seth Stein and Michael Wysession. *An Introduction to Seismology, Earthquakes, and Earth Structure*. Blackwell Publishing, 2003.

[101] C. A. Hagedorn. Personal Correspondence, 2015.

[102] T. J. Quinn, R. S. Davis, C. C. Speake, and L. M. Brown. The restoring torque and damping in wide cu-be torsion strips. *Phys. Lett. A*, 228:35–42, January 1997.

[103] T. J. Quinn, C. C. Speake, and R. S. Davis. Novel torsion balance for the measurement of the newtonian gravitational constant. *Metrologia*, 34:245–249, 1997.

[104] Terry Quinn, Clive Speake, Harold Parks, and Richard Davis. The bipm measurements of the newtonian constant of gravitation, *g*. *Philos. Trans. Roy. Soc. A*, 372(20140032), 2014.

[105] Massimo Bassan, Fabrizio De Marchi, Lorenzo Marconi, Giuseppe Pucacco, Ruggero Stanga, and Massimo Visco. Torsion pendulum revisited. *arXiv*, (1305.7075v1), May 2013.

[106] L. D. Landau and E. M. Lifshitz. *Mechanics*. Pergamon Press Ltd., 2 edition, 1976.

[107] Aliasing and sampling at frequencies above the nyquist frequency. www.ni.com/white-paper/3000/en.

Appendices

Appendix A

Modeling the Torsion Balance Motion

As described in § 4.2.2, the eddy-current damper that the torsion fiber is attached to quickly damps away pendular motion of the balance that can be excited by seismic disturbances. While the simplified equations of motion usually used to describe the motion of a pendulum suggest that the torsional oscillations of the balance are independent of other modes of oscillation, a more detailed analysis of the motion of the balance shows that if not properly damped, pendular modes will couple to the torsional mode of the balance [82, 83, 105]. A detailed numerical model of this coupling for the balance used in this experiment is presented.

A.1 The Lagrangian of the Balance

To describe the setup illustrated in Figure A.1, two coordinate systems are defined. A stationary coordinate system, set in the reference frame of the laboratory, is described by coordinates (x_0, y_0, z_0) with the origin set at the point O_0 from which the torsion fiber is

attached. The second coordinate system is defined with respect to the moving balance, with the origin O_1 located at the point where the fiber attaches to the rigid balance, with coordinates (x_1, y_1, z_1). The five degrees of freedom shown for this system are labeled by $\phi_0, \varphi_0, \phi_1, \varphi_1$, and θ_1, where ϕ_0 and φ_0 represent the deflection of the fiber about the axes of the fixed frame given by coordinates x_0 and y_0, respectively, ϕ_1 and φ_1 represent a deflection about the axes of the frame fixed to the balance, x_1 and y_1, respectively, and θ_1 represents a rotation about the fiber, along the axis described by z_1. Also labeled in Figure A.1, the length of the torsion fiber (O_0 to O_1) is given by l_0, and the distance from O_1 to the center of mass of the balance is given by l_1.

The transformation between the laboratory-fixed reference frame and the moving frame is given by

$$\begin{aligned}
x_0 =& -l_0\cos\varphi_0 + x_1\cos\varphi_1\cos\theta_1 - y\cos\varphi_1\sin\theta_1 + z\sin\varphi_1,\\
y_0 =& \, l_0\cos\varphi_0\sin\phi_0 + x_1(\cos\phi_1\sin\theta_1 + \cos\theta_1\sin\varphi_1\sin\phi_1)\\
&+ y_1(\cos\phi_1\cos\theta_1 - \sin\theta_1\sin\varphi_1\sin\phi_1) - z_1\cos\varphi_1\sin\phi_1,\\
z_0 =& -l_0\cos\varphi_0\cos\phi_0 + x_1(\sin\phi_1\sin\theta_1 - \cos\theta_1\sin\varphi_1\cos\phi_1)\\
&+ y_1(\sin\phi_1\cos\theta_1 + \sin\theta_1\sin\varphi_1\cos\phi_1) + z_1\cos\varphi_1\cos\phi_1.
\end{aligned} \tag{A.1}$$

The Lagrangian for the torsion balance system is given by

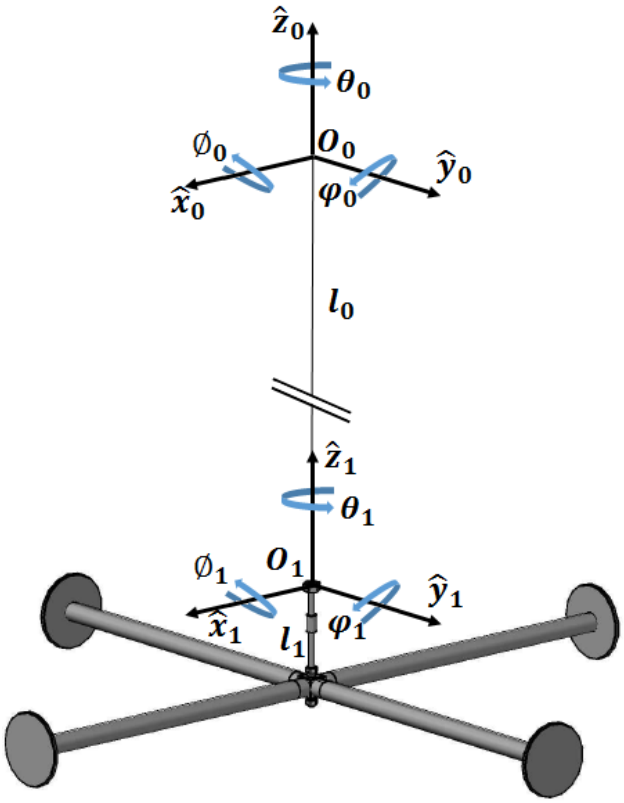

Figure A.1: Diagram of the balance with stationary lab-based coordinate system (x_0, y_0, z_0) and moving balance coordinates (x_1, y_1, z_1) illustrated.

$$L = T_{trans} + T_{rot} - U \tag{A.2}$$

where the T_{trans} is the translational kinetic energy of the balance, T_{rot} is the rotational kinetic energy of the balance, and U is the potential energy, which includes the energy due to the restoring torque of the torsion fiber.

To find the translational kinetic energy of the system, the balance is treated as a point, with all of its mass, m, located at the center of mass. Since the center of mass of the balance is located at $(0, 0, -l_1)$ in the frame of the balance,

$$\begin{aligned}
T_{trans} =& \frac{1}{2}m(\dot{x}_0^2 + \dot{y}_0^2 + \dot{z}_0^2) \\
=& \frac{1}{2}ml_0^2\cos^2\varphi_0\dot{\phi}_0^2 + \frac{1}{2}ml_0^2\dot{\varphi}_0^2 + \frac{1}{2}ml_1^2\cos^2\varphi_1\dot{\phi}_1^2 + \frac{1}{2}ml_1^2\dot{\varphi}_1^2 \\
&+ ml_0l_1\cos\varphi_0\cos\varphi_1\cos(\phi_0-\phi_1)\dot{\phi}_0\dot{\phi}_1 \\
&+ ml_0l_1\cos\varphi_0\sin\varphi_1\sin(\phi_0-\phi_1)\dot{\phi}_0\dot{\varphi}_1 \\
&- ml_0l_1\sin\varphi_0\cos\varphi_1\sin(\phi_0-\phi_1)\dot{\varphi}_0\dot{\phi}_1 \\
&+ ml_0l_1[\cos\varphi_0\cos\varphi_1 + \cos(\phi_0-\phi_1)\sin\varphi_0\sin\varphi_1]\dot{\varphi}_0\dot{\varphi}_1
\end{aligned} \tag{A.3}$$

The rotational kinetic energy of the system is given by

$$T_{rot} = \frac{1}{2}I_{ij}\omega_i\omega_j \tag{A.4}$$

where I_{ij} is the inertia tensor of the balance, and ω_i and ω_j are vectors which give the components of the angular velocity of the balance in the moving frame. The inertia tensor, as defined by Landau and Lifshitz [106], for a continuous rigid body is given explicitly by

$$I_{ij} = \int \rho(x_1, y_1, z_1)\begin{bmatrix} y_1^2+z_1^2 & -x_1y_1 & -x_1z_1 \\ -x_1y_1 & z_1^2+x_1^2 & -y_1z_1 \\ -x_1z_1 & -y_1z_1 & x_1^2+y_1^2 \end{bmatrix} dV. \tag{A.5}$$

For this system the angular velocity vectors are given by [105]

$$\begin{aligned}\omega_x =&\dot{\varphi}_1 \sin\theta_1 + \dot{\phi}_1 \cos\varphi_1 \cos\theta_1,\\ \omega_y =&\dot{\varphi}_1 \cos\theta_1 - \dot{\phi}_1 \cos\varphi_1 \sin\theta_1,\\ \omega_z =&\dot{\theta}_1 + \dot{\phi}_1 \sin\varphi_1.\end{aligned} \tag{A.6}$$

If the balance is symmetric about its center of mass in the x_0, y_0, and z_0 directions, I_{xx}, I_{yy}, and I_{zz} are the principle moments of inertia, and the off diagonal elements of the inertia tensor are zero. Then, by Equation (A.4), the rotational kinetic energy of the balance is

$$\begin{aligned}T_{rot} =&\frac{1}{2} I_{xx}[\dot{\varphi}_1^2 \sin^2\theta_1 + \dot{\phi}_1^2 \cos^2\varphi_1 \cos^2\theta_1 + 2\dot{\varphi}_1\dot{\phi}_1 \sin\theta_1 \cos\theta_1 \cos\varphi_1]\\ &+ \frac{1}{2} I_{yy}[\dot{\varphi}_1^2 \cos^2\theta_1 + \dot{\phi}_1^2 \cos^2\varphi_1 \sin^2\theta_1 - 2\dot{\varphi}_1\dot{\phi}_1 \sin\theta_1 \cos\theta_1 \cos\varphi_1]\\ &+ \frac{1}{2} I_{zz}[\dot{\theta}_1^2 + \dot{\phi}_1^2 \sin^2\varphi_1 + 2\dot{\theta}_1\dot{\phi}_1 \sin\varphi_1].\end{aligned} \tag{A.7}$$

The potential energy, U, of the system is given by

$$\begin{aligned}U =&mgz_0 + \frac{1}{2}\kappa_f \theta_1^2\\ =&- mg(l_0 \cos\phi_0 \cos\varphi_0 + l_1 \cos\phi_1 \cos\varphi_1) + \frac{1}{2}\kappa_f \theta_1^2\end{aligned} \tag{A.8}$$

where g is the local acceleration due to the Earth's gravity, and κ_f is the torsion constant of the fiber.

Inserting the results from Equations (A.3), (A.7) and (A.8) into Equation (A.2) gives the Lagrangian of the system. Using Lagrange's equation

$$\frac{\partial L}{\partial q_i} - \frac{d}{dt}\left[\frac{\partial L}{\partial \dot{q}_i}\right] = 0, \tag{A.9}$$

where $q_i = (\phi_0, \varphi_0, \phi_1, \varphi_1, \theta_1)$, a system of five non-linear equations of motion is obtained which can be solved numerically for specified initial conditions.

A.2 Coupled Modes of the Balance

A Mathematica code was written to numerically solve the system of equations given by Equation (A.9). The results illustrate a number of features arising from the coupled modes which are observed in the actual balance. Because the alignment of the autocollimator is not perfectly perpendicular to the plane of the balance, modes other than solely the torsional mode are detected in the balance position readout. Thus the pendular (corresponding to ϕ_0 and φ_0) and wobble (corresponding to ϕ_1 and φ_1) modes have also been investigated. While not considered in this analysis, various other modes exist, such as the 'violin' modes and the 'bounce' mode. Initial conditions of $\phi_0 = \varphi_0 = \phi_1 = \varphi_1 = 0.0002$ rad, $\theta_1 = 0.001$ rad, and $\dot{\phi_0} = \dot{\varphi_0} = \dot{\phi_1} = \dot{\varphi_1} = \dot{\theta_1} = 0$ rad/s were used for the results shown.

In Figure A.2, the pendular and wobble modes of the balance are shown (ϕ_0 and ϕ_1, respectively). In each case, a varying amplitude indicates the presence of multiple driving frequencies. For a symmetric balance, as shown here, the pendular modes ϕ_0 and φ_0 are

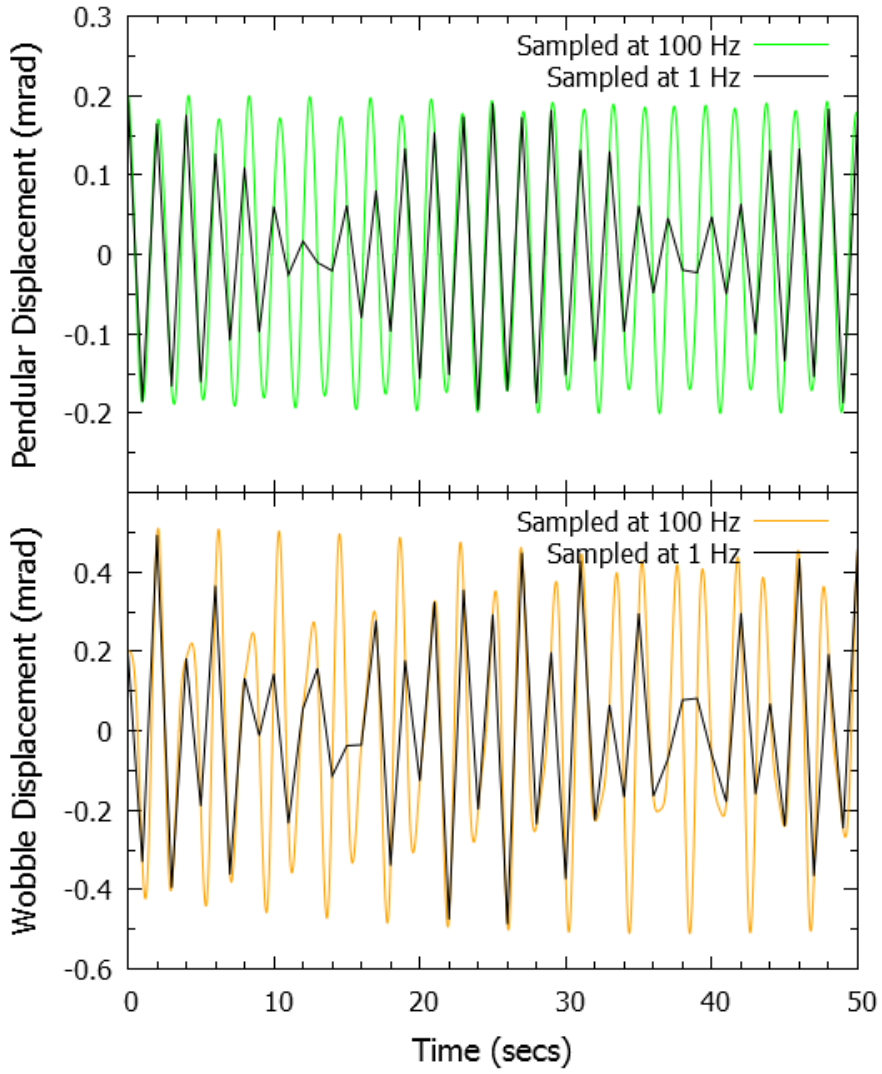

Figure A.2: Top: Pendular displacement $\phi_0(t)$ for the balance sampled at 1 Hz (shown in black) and 100 Hz (green). Bottom: Wobble of the balance $\phi_1(t)$, also sampled at 1 Hz (black) and 100 Hz (orange). In both modes the balance was initially at rest with a displacement of 0.0002 rad.

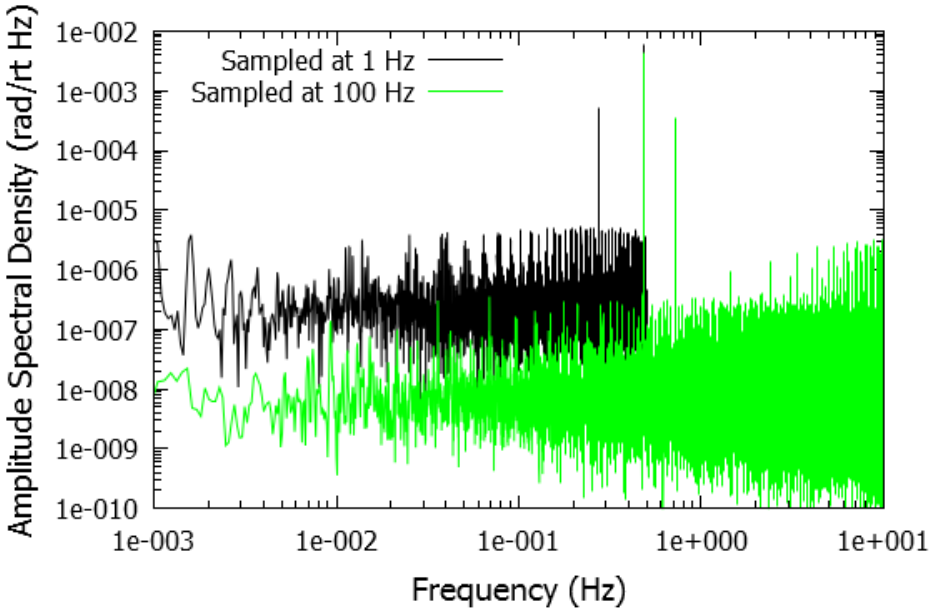

Figure A.3: Amplitude Spectral Density of the pendular motion of the balance. Prominent peaks occur at $f = 0.48$ and 0.73 Hz. Aliasing causes the higher frequency peak to appear at $f = 0.27$ Hz when the signal is sampled at 1 Hz (shown in black).

identical (as are the wobble modes ϕ_1 and φ_1). As discussed when addressing the torsional mode, asymmetries of the balance affect the behavior of the balance by introducing addition driving frequencies. Also illustrated in this figure is a phenomena known as aliasing. Aliasing is a limitation of discrete-time sampling which occurs when a signal with frequency f_s is sampled below the Nyquist frequency $f_N = 2f_s$. The frequency of an aliased signal f_a is given by

$$f_a = |nf_{samp} - f_s| \tag{A.10}$$

where f_{samp} is the frequency the signal is being sampled at and n is the closest integer

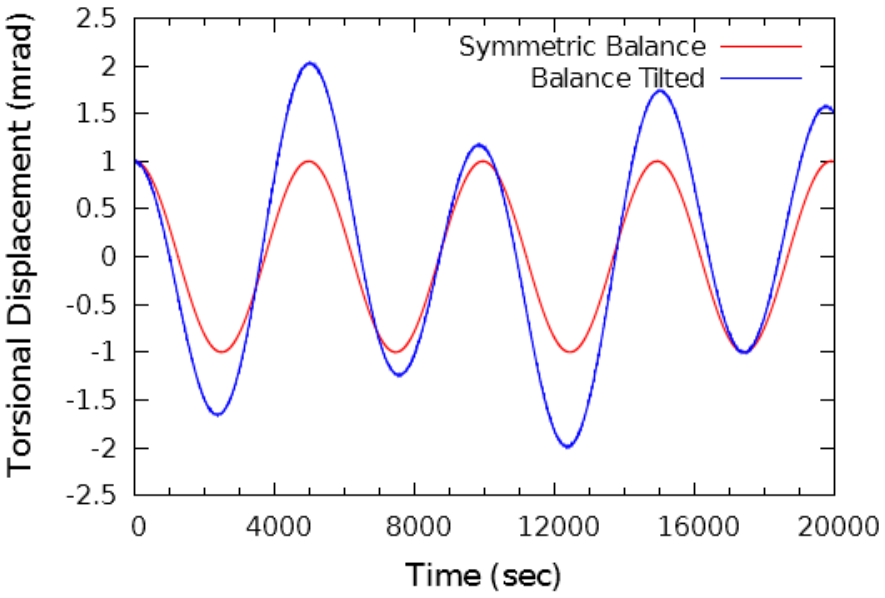

Figure A.4: Torsional oscillations for a symmetric balance (in red), and one that is slightly tilted (in blue).

multiple of f_{samp} to f_s [107]. During data collection, the balance position was sampled with at $f_{samp} \approx 1$ Hz, thus modes with $f_s > 1$ Hz appear in the Fourier transform of the signal as peaks at lower frequencies. In the future, this could be avoided by using an anti-alias filter.

The torsional motion of the balance θ_1 obtained from the numerical computation is shown in Figure A.4 both for a symmetric balance, where I_{xx}, I_{yy}, and I_{zz} are the principle moments of inertia, and for a balance that is tilted by some amount. This tilt has been exaggerated, but nonetheless illustrates the importance producing a symmetric balance. An enlarged view of the torsional motion for both cases is given in Figure A.5. Here it is demonstrated that the oscillations of other modes effect the torsional mode, thus it is important to adequately damp these oscillations.

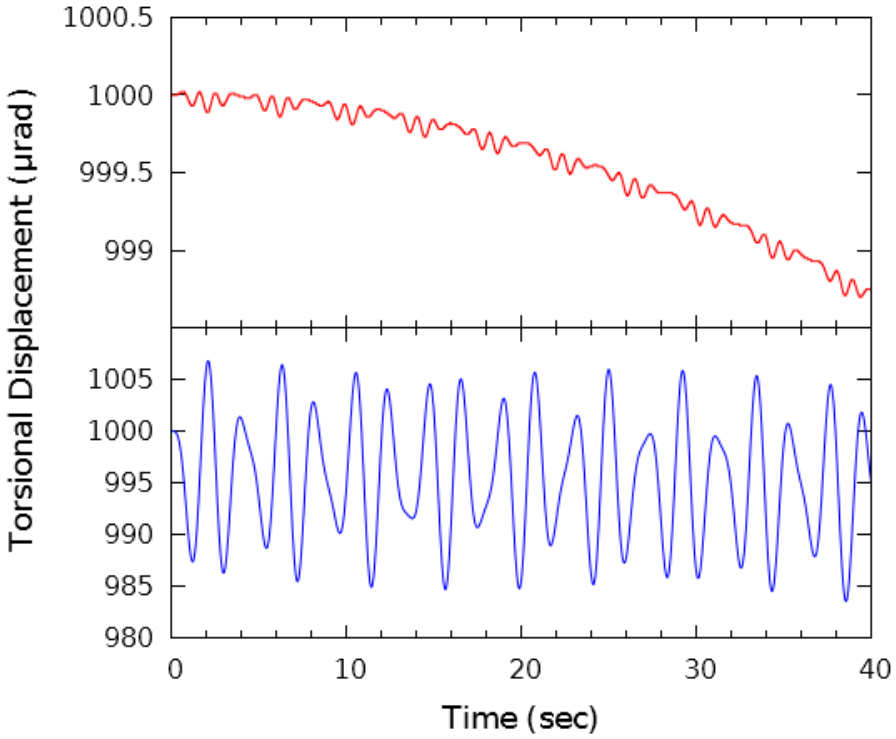

Figure A.5: Top: Enlarged view of the high frequency torsional motion of for a symmetric balance (in red). Bottom: View of the high frequency torsional motion of a balance with some tilt (in blue). The torsional oscillations are affected by the other modes of the balance.

Appendix B

MATLAB Programs

B.1 Calculating the Signal Expected from a Potential Violation of the Equivalence Principle

```
% EPsignal.m

% This program calculates the expected deflection of the balance given an input
% file with three columns: Solar azimuth (in deg), elevation (deg), and the
% Earth–Sun separation (AU) recorded at regular intervals – this info can be
% obtained via the JPL Horizons online ephemeris (ssd.jpl.nasa.gov/?horizons)

load JPLsolarPos.txt % replace "JPLsolarPos" with your filename
azi=JPLsolarPos(:,1);
elv=JPLsolarPos(:,2);
R=JPLsolarPos(:,3);

% The follow constants and parameters may be set for your balance
delT = 600/86400;        % time interval between entries (in days)
eot = 10^(-12);          % Eotvos parameter
G = 6.67384*10^(-11);    % in m^3 kg^-1 s^-2
M = 1.9891*10^(30);      % mass of sun (in kg)
m_g = 0.0143;            % mass of a balance test mass (in kg)
```

```
p = 1.4142;              % balance geometric parameter
r = 0.25;                % length of balance arm (in m)
AU = 1.49598*10^(11);    % in m
theta = 0;               % orientation of the balance wrt north
k = 0.0647;              % rigidity of the torsion fiber (in dyne cm)

% Determine length of input file
[sizT,z] = size(azi);

auR = zeros(sizT,1);
t = zeros(sizT,1);
for n=1:sizT
    auR(n)=AU*R(n);      % convert earth-sun separation distances to meters
    t(n) = delT*(n-1);   % create array of time entries
end

const = eot*G*M*m_g*r*p;
torque = zeros(sizT,2);
torQ = zeros(sizT,1);
defl = zeros(sizT,1);
angles = zeros(sizT,1);
angles1 = zeros(sizT,1);
val = zeros(sizT,2);
for m=1:sizT
    xi = (90-elv(m))*0.01745329;        % zenith angle (converted to radians)
    phi = (azi(m)-theta)*0.01745329;    % angle btw balance,sun in horizon dir
    rad = auR(m);                       % Earth-sun separation (in meters)
    tor = const*sin(xi)*sin(phi)/rad^2; % torque on the balance
    torQ(1,m) = t(m);                   % put time, torque values in an array
    torQ(2,m) = tor;
    defl(1,m) = t(m);                   % put time, deflection in an array
    defl(2,m) = tor/(k/10000000);
end

plot(defl(1,:),defl(2,:))               % plot the balance deflection

% Write the time and deflection data to a text file called "defl.txt"
% The output file is given with two columns: time (days) and deflection (rad)
fid = fopen('defl.txt', 'w');
fprintf(fid,'%15.18f %15.18f\r\n',defl);
fclose(fid);
```

B.2 Analysis of Data in the Time Domain

```
% EPdataAnalysis.m

% This program determines the maximum amplitude of a signal from a potential
% EP violation from balance position data collected from the experiment.
% Input files: (1) text file containing time (in sec) and centroid position
% (in pixels) in separate columns (2) text file with time (sec), four columns
% of voltages across thermistors (in V), and the voltage corresponding to the
% current across the ion pump (in V, where 1V = 1mA).

load EQPtest_27Feb2016.txt     % balance position file
load EQPtest_27Feb2016temp.txt % temperature, ion pump current file
t = EQPtest_27Feb2016(:,1);
pos = EQPtest_27Feb2016(:,2);
temp = EQPtest_27Feb2016temp;

% User input parameters, set these for each particular input file
T = 4867.6; % Torsional period of the balance (in sec)
t0 = 32424.04 % Seconds after midnight that the file starts
ts = -780; % Seconds after midnight when expected signal is 0
avgInt = 60; % Number of seconds to average over
tT0 = 32428.08; % Seconds after midnight that the temperature file starts

% Calls the function "filt2pt.m", returns filtered t and pos arrays
[tFil,pFil] = filt2pt(t,pos,T);

% Calls the function "TEMPprog(temp), converts thermistor voltages into temp
[thermTemps] = TEMPprog(temp); % output temperature is in deg F
tT = thermTemps(:,1);          % Thermistor time array (in sec)
temp1 = thermTemps(:,2);       % One thermistor temperator output (in deg F)

% Calls the functions "split24hr.m" and "split24hrT.m"
% Input the filtered time (sec), pos (pix), and parameters defined above and
% retuns the linear drift removed from position data (slpArray, in pix/s),
% time and pos (in pix), time and temp (in deg F) in arrays, broken into 24
% hour segments.
[slpArray,posArray,noDays] = split24hr(tFil,pFil,t0,ts,avgInt);
[slpTArray,tempArray] = split24hrT(tT,temp1,tT0,ts,avgInt);

% Calls the function "fourierCmpts.m" and fits EP violation signal to position
% data from posArray (position with drift removed).
% intPosSum has two columns: days number and amplitude of deflection (in urad)
% fourFits has four columns: t, averaged pos, sine function, avgPos*sin
[fourFits,intPosSum] = fourierCmpts(posArray); %posArray in pixels
```

```
plot(intPosSum(1,:),intPosSum(2,:))

% This section was added to qualitatively look for a correlation between
% balance deflection and temperature, can be removed if not needed
% Print plots of position and temperature for each day separately
for k = 1:noDays
    filename = ['MyPlot_',num2str(k)]

    figure
    subplot(1,2,1)
    plot(posArray(:,1)/3600,posArray(:,k*2+1))
    title('Position')
    xlabel('Time (hrs)')
    ylabel('Position (pix)')
    axis([0 24 -inf inf])
    set(gca,'xTick',0:6:24)

    subplot(1,2,2)
    plot(tempArray(:,1)/3600,tempArray(:,k*2+1))
    title('Temperature')
    xlabel('Time (hrs)')
    ylabel('Temp (deg F)')
    axis([0 24 -inf inf])
    set(gca,'xTick',0:6:24)

    print(filename,'-dpng')
end

% Write the filtered data to an output file "EQPtest_27Feb2016_2ptFIL.txt"
A(1,:)=tFil;
A(2,:)=pFil;

fid = fopen('EQPtest_27Feb2016_2ptFIL.txt', 'w');
fprintf(fid,'%15.6f %15.6f\r\n',A);
fclose(fid);

% Write the amplitude of balance deflection limiting an EP violation to a file
fic = fopen('EQPtest_27Feb2016_deflAmp.txt', 'w');
fprintf(fid,'%15.6f %15.6f\r\n',intPosSum);
fclose(fic);
```

```
% TEMPprog.m

% This is a function which takes an array with six columns (temp) containing
% time (in sec), the voltage across four thermistors, and the voltage recorded
% by an ion pump controller (NI USB-6008 DAQ used to measure these voltages)
% and converts these voltages to temperatures (in deg F).

function [thermTemps] = TEMPprog(temp)

t=temp(:,1);
therm(:,1)=temp(:,2);
therm(:,2)=temp(:,3);
therm(:,3)=temp(:,4);
therm(:,4)=temp(:,5);
pres(:,1)=temp(:,6); % pressure info not used here, could be converted as well

[sizT,z] = size(t);  % determine the number of entries in the input file

% Constants for thermistors, can be adjusted if necessary
V = 5.052;
Rres = 10000;
a = 0.0011253088521;
b = 0.0002347118633;
c = 0.0000000856635;

% Converting the thermistor voltages to temperature using Steinhart-Hart Eq.
for j = 1:4
    for i = 1:sizT
        Vtherm = therm(i,j);
        Vres = V-Vtherm;
        Rtherm = (Vtherm/Vres)*Rres;
        Tk = 1/(a+b*log(Rtherm)+c*log(Rtherm)^3);
        Tf = (Tk-273.15)*1.8+32;
        temp(i,j) = Tf;
    end

    % Averaging over 100 temperature entries to reduce scatter (optional)
    sizAvg = fix(sizT/100);
    k = 1;
    for n = 1:sizAvg
        tempSum = 0;
        for m = 1:100
            tempSum = temp(k,j)+tempSum;
            k = k + 1;
        end
            tempAvg(n,j) = tempSum/100;
            tAvg(n) = 100*n-50+t(1);
    end
end
```

```
A(:,1) = t;
A(:,2) = temp(:,1);
A(:,3) = temp(:,2);
A(:,4) = temp(:,3);
A(:,5) = temp(:,4);
B = transpose(A);
thermTemps = A;     % array with time and temperature measured by 4 thermistors
```

```
% split24hr.m

% This is a function that takes the filtered balance position data, breaks it
% into 24 hr segments that start and end at solar nadir, remove the linear
% drift from each of these segments, and return the number of full days in the
% file (noDays), an array with time and position for the drift-subtracted 24
% hr segments (posArray, in pix), and the slope of the linear drift that was
% removed for each day (slpArray, in pix/s).

function [slpArray,posArray,noDays] = split24hr(tFil,pFil,t0,ts,avgInt)

t = tFil;    % Time data corresponding to filtered position points
pos = pFil;  % Filtered position data

t = t-ts+t0; % Time shift based on data file start time

% Determine how many full days are in the data file (day starts at solar nadir)
[z,sizT] = size(t);
if z > sizT
    sizT = z;
end
strtT = floor(t(1)/86400)+1;
noDays = floor(t(sizT)/86400)-strtT; % Number of full days in the data file

% Remove entries beyond the last complete day in the file
for q = 1:sizT
    if t(q)>(strtT*86400)
        indxT = q;
        break
    end
end

t = t(indxT:sizT);
pos = pos(indxT:sizT);

% Average the time and position across 'avgInt'-length segments to ensure
% uniform number of entries for each day (autocollimator timing not uniform).
% jIndx is the total number of 'avgInt'-length segments span 'noDays' of data
```

```
jIndx = 86400*noDays/avgInt;
iIndx = 1;
tSum = 0;
posSum = 0;
posIndx = 0;
for j = 1:jIndx
    tMed(j) = avgInt*j-10+t(1); % Median time for each 'avgInt'-long segment
    jMin = avgInt*(j-1)+t(1);
    jMax = avgInt*j+t(1);
    for i = iIndx:sizT-indxT
        tVal = t(i);
        posVal = pos(i);
        if tVal > jMin
            if tVal < jMax
                tSum = tSum+tVal;
                posSum = posSum+posVal;
                posIndx = posIndx+1;
                iIndx = i;
            else
                tAvg(j) = tSum/posIndx;     % Average time for each segment
                posAvg(j) = posSum/posIndx; % Average position for each segment
            end
        end
    end
    tSum = 0;
    posSum = 0;
    posIndx = 0;
end

% Reshape the avg time and position arrays into separate columns for each day
tAvg = reshape(tAvg,86400/avgInt,noDays);
posAvg = reshape(posAvg,86400/avgInt,noDays);

% Remove drift across pos(t=0s) to pos(t=86400s) for each segment, m(k)
% posAvgSub gives the average position for each day with drift removed
% posAvgDay gives the position (w/o drift) averaged over each day in segment
posAvgDay=zeros(86400/avgInt,1);
for k=1:noDays
    m(k) = (posAvg(86400/avgInt,k)-posAvg(1,k))/(tAvg(86400/avgInt,k)-tAvg(1,k));
    b(k) = posAvg(1,k)-m(k)*tAvg(1,k);
    for l = 1:86400/avgInt
        posAvgSub(l,k) = posAvg(l,k)-(m(k)*tAvg(l,k)+b(k));
        posAvgDay(l) = posAvgSub(l,k)+posAvgDay(l);
    end
end

% Create array with day number and slope (pix/s) for each day in segment
for r = 1:noDays
    A(r,1) = strtT+r-1;
```

```
    A(r,2) = m(r);
end
slpArray = transpose(A);

% Create array with averaged position with drift removed for each day
C(1,:) = tAvg(:,1)-t(1);    % First column has time from 0s to 86400s
for s = 1:noDays
    C(2*s,:) = tAvg(:,s);   % 2*s columns have time for each segment
    C(2*s+1,:) = posAvgSub(:,s);
end
posArray = transpose(C);
```

```
% split24hrT.m

% This function performs a similar role as "split24hr.m" except for temp data.
% It takes temperature data, breaks it into 24 hr segments ending at solar
% nadir, and returns temperature change across each 24 hr segment (slpTArray)
% and an array of 24 hr temperature segments (with or without drift removed).

% For additional comments see "split24hr.m"

function [slpTArray,tempArray] = split24hrT(tT,temp1,tT0,ts,avgInt)

t = tT;       % Array of time stamps for input temperature values
pos = temp1;  % Array of temperature values from thermistor 1

t = t-ts+tT0; % Time shift based on temperature data start time

% Determine how many full days (noDays) are in the data file
[z,sizT] = size(t);
if z > sizT
    sizT = z;
end
strtT = floor(t(1)/86400)+1;
noDays = floor(t(sizT)/86400)-strtT;

% Remove entries beyond the last complete day in the file
for q = 1:sizT
    if t(q)>(strtT*86400)
        indxT = q;
        break
    end
end

t = t(indxT:sizT);
pos = pos(indxT:sizT);
```

```
% Average the time and temperature across 'avgInt'-length segments to ensure
% uniform number of entries for each day and to match position timing.
% j Indx gives total number of 'avgInt'-length segments span 'noDays' of data
jIndx = 86400*noDays/avgInt;
iIndx = 1;
tSum = 0;
posSum = 0;
posIndx = 0;
for j = 1:jIndx
    tMed(j) = avgInt*j-10+t(1); % Median time for each 'avgInt' long segment
    jMin = avgInt*(j-1)+t(1);
    jMax = avgInt*j+t(1);
    for i = iIndx:sizT-indxT%noDays*86400
        tVal = t(i);
        posVal = pos(i);
        if tVal > jMin
            if tVal < jMax
                tSum = tSum+tVal;
                posSum = posSum+posVal;
                posIndx = posIndx+1;
                iIndx = i;
            else
                tAvg(j) = tSum/posIndx;
                posAvg(j) = posSum/posIndx;
            end
        end
    end
    tSum = 0;
    posSum = 0;
    posIndx = 0;
end

% Reshape the avg time and position arrays into separate columns for each day
tAvg = reshape(tAvg,86400/avgInt,noDays);
posAvg = reshape(posAvg,86400/avgInt,noDays);


% Remove drift across pos(t=0s) to pos(t=86400s) for each segment, m(k)
% posAvgSub gives the average temperature for each day with drift removed
% posAvgDay gives the temperature (w/o drift) averaged over each day in segment
posAvgDay=zeros(86400/avgInt,1);
for k=1:noDays
    m(k) = (posAvg(86400/avgInt,k)-posAvg(1,k))/(tAvg(86400/avgInt,k)-tAvg(1,k));
    b(k) = posAvg(1,k)-m(k)*tAvg(1,k);
    for l = 1:86400/avgInt
        posAvgSub(l,k) = posAvg(l,k)-(m(k)*tAvg(l,k)+b(k));
        posAvgDay(l) = posAvgSub(l,k)+posAvgDay(l);
    end
end
```

```
% Create array of daily temperature drifts
for r = 1:noDays
    A(r,1) = strtT+r-1;
    A(r,2) = m(r);
end
slpTArray = transpose(A);

% Create array of temperature over 24 hr segments
% With or without temp drift removed chosen by uncommenting relevant option,
% dependence of balance drift was qualitatively investigated both ways
C(1,:) = tAvg(:,1)-t(1);
for s = 1:noDays
    C(2*s,:) = tAvg(:,s);
    %C(2*s+1,:) = posAvg(:,s); % Print temp without drift removed
    C(2*s+1,:) = posAvgSub(:,s); % Print temp with linear drift removed
end
tempArray = transpose(C);
```

```
% fourierCmpts.m

% This function takes the 24 hr segments and determines the amplitude of a
% sine function in phase with the signal from an EP violation.

function [fourFits,intPosSum] = fourierCmpts(posArray)

v = posArray;
t = v(:,1); % t is averaged time array from 0s to 86400s

% Determine indices of "NaN" entries
kt=find(isnan(t));
[sizKt,z] = size(kt);
for l = 1:sizKt
    ktIndx = kt(l);
    t(ktIndx)=(t(ktIndx-1)+t(ktIndx+1))/2;
end

% Replace "NaN" entries with average of adjacent entries
[z,sizV] = size(v);
sizV = (sizV-1)/2;
avgPos = 0;
for j = 1:sizV;
    t = v(:,2*j);
    kt=find(isnan(t));
    [sizKt,z] = size(kt);
    for l = 1:sizKt
        ktIndx = kt(l);
```

```
        t(ktIndx)=(t(ktIndx-2)+t(ktIndx+2))/2;
    end

    avgPos = v(:,2*j+1);

    k=find(isnan(avgPos));
    [sizK,z] = size(k);
    for l = 1:sizK
        kIndx = k(l);
        avgPos(kIndx)=(avgPos(kIndx-1));
    end
    avgPos = avgPos*7;      % convert from pixels to urad
    t = t/3600;             % convert from sec to hrs

    % Create an array of values for sin(w*t) where w is 2*pi/(24 hr)
    % Create an array of values for sin(w*t)*avgPos(t) - store as intPos
    for i = 1:1440
        sinPos(i) = sin(0.2617993878*t(i));
        intPos(i) = avgPos(i)*sinPos(i);
    end

    intPosTerms = transpose(intPos);
    intPosSum(1,j) = round(t(1)/24);          % time (in days)
    intPosSum(2,j) = trapz(t,intPosTerms)/12; % fit from integral of intPos
end

% Save time (in hrs), avgPos (in urad), array of the sine function, and
% array of sin(w*t)*avgPos(t) used as integrand in array "fourFits"
A(1,:) = t;
A(2,:) = avgPos;
A(3,:) = sinPos;
A(4,:) = intPosTerms;
fourFits = transpose(A);
```

B.3 Calculating the Spectral Density of the Balance Position Data

```
% FFTprogram2015.m

% The program is used to calculate the amplitude spectral density of the
% position measured by the autocollimator. It takes an input text file with
% two columns, time (in sec) and centroid position (in CCD pixel number) and
% returns files with (1) the centroid position, converted to radians with
% some specified drift removed, and (2) the Fourier transform of this
% position (columns of frequency, in hertz, and amplitude spectral density,
% in rad/rt Hz).

load EQPtest_27Feb2016.txt   % Input text file "EQPtest_27Feb2016"
t=EQPtest_27Feb2016(:,1);
pos=EQPtest_27Feb2016(:,2);

% FFT frequency stuff
[sizT,z] = size(t);    % determines the number of entries in input file
totT = t(sizT) - t(1); % length of data set
delT = totT/sizT;      % time interval, assumes constant read rate
delF = 1/totT;         % frequency step
sampF = 1/delT;
freqRange = sampF/2;

freqArray = 0:delF:freqRange; % create array of frequency values

pos = 0.000007*pos;           % convert position array to radians
%pos = (pos + 459.67)*(5/9);  % Use for temperature data (in K)

% Want to get the subtracted fit data
n = 1;                        % polynomial order of subtracted fit, set by user
fit = polyfit(t,pos,n);       % n-order polynomial fit to position data
posFit = polyval(fit,t);      % create array of position values for this fit
plot(t,pos,t,posFit)          % plot position data and polynomial fit

posSubFit = pos-posFit;       % remove best fit from data


% Apply a Hann windowing function to drift subtracted position data
w = hann(sizT);
posSubFitH = posSubFit.*w;
```

```
% Calculating the FFT
Y = fft(posSubFitH);
YY = Y.*conj(Y);

phase = angle(Y);               % array of FFT phase information

MyFFT = sqrt(YY/(sampF*sizT)); % normalize FFT (get amplitude spectral density)
[z,sizFreqArray] = size(freqArray);
loglog(freqArray,MyFFT(1:sizFreqArray))  % plot ASD on log-log scale

% Build an array with frequency information
A = zeros(sizFreqArray,2);
for m = 1:sizFreqArray
    A(1,m) = freqArray(m);
    A(2,m) = MyFFT(m);
end

% Build an array with fit subtracted position information
C = zeros(sizT,2);
for n = 1:sizT
    C(n,1) = t(n);
    C(n,2) = posSubFit(n);
end

% Print the frequency and position information
fid = fopen('FFTdata.txt', 'w');
fprintf(fid,'%15.18f %15.18f\r\n',B);
fclose(fid);

fic = fopen('PositionData.txt', 'w');
fprintf(fic,'%15.18f %15.18f %15.18f\r\n',D);
fclose(fic);
```

Appendix C

LabVIEW Interface

Data acquisition is performed using a LabVIEW program developed specifically for this experiment. LabVIEW is a visual programming language which includes extensive support for interfacing with cameras and other devices making it a popular platform for data acquisition and instrument control. The program (called a VI) includes a user interface, called a front panel, and the coding environment, which is called a block diagram. Some of the plots present on the front panel include:

- The image captured by the autocollimator CCD
- The centroid value of this image
- The time derivative of the balance position
- The total number of counts across all 2048 CCD pixels
- The temperatures measured by each of the thermistors set up around the instrument
- The ion pump current, output as a voltage from the ion pump controller

In order to obtain high resolution performance with the autocollimator, the image captured by the CCD camera must be of good quality — that is the peaks of the image must be well resolved and have a relatively high amplitude. The centroid value x_c is used to determine the position of the torsion balance θ. The time derivative of the balance position dx/dt is used while damping the torsional oscillations of the balance. The total number of counts is helpful when aligning the autocollimator and mirrored balance mass by adjusting the gimbal mirror. Various other plots, controls, and indicators are displayed on the front panel as well (Figure C.1).

The major steps performed by the graphical source code on the block diagram are illustrated by a flowchart in Figure C.2. Before starting data collection, a dark current measurement is made by storing an image obtained while the end of the autocollimator tube has been covered by a dark surface. This allows for a dark frame subtraction to be made from every summed image collected during a data run to remove false counts which are intrinsic to each pixel of the CCD. Once the program is started a function generator triggers the autocollimator CCD camera. Individual images are summed to create a frame-summed image. After the removed of the dark current, the locations of fiducial points corresponding to each of the peaks of the autocollimator image are determined use a sub-routine (or a subVI). Another subVI then uses a centroiding algorithm to identify the precise location of each peak, before averaging these peak values to produce a centroid value of the total image x_c. The image centroid is plotted, written to a file, and then used to determine the velocity dx_c/dt and acceleration d^2x_c/dt^2 of the balance motion.

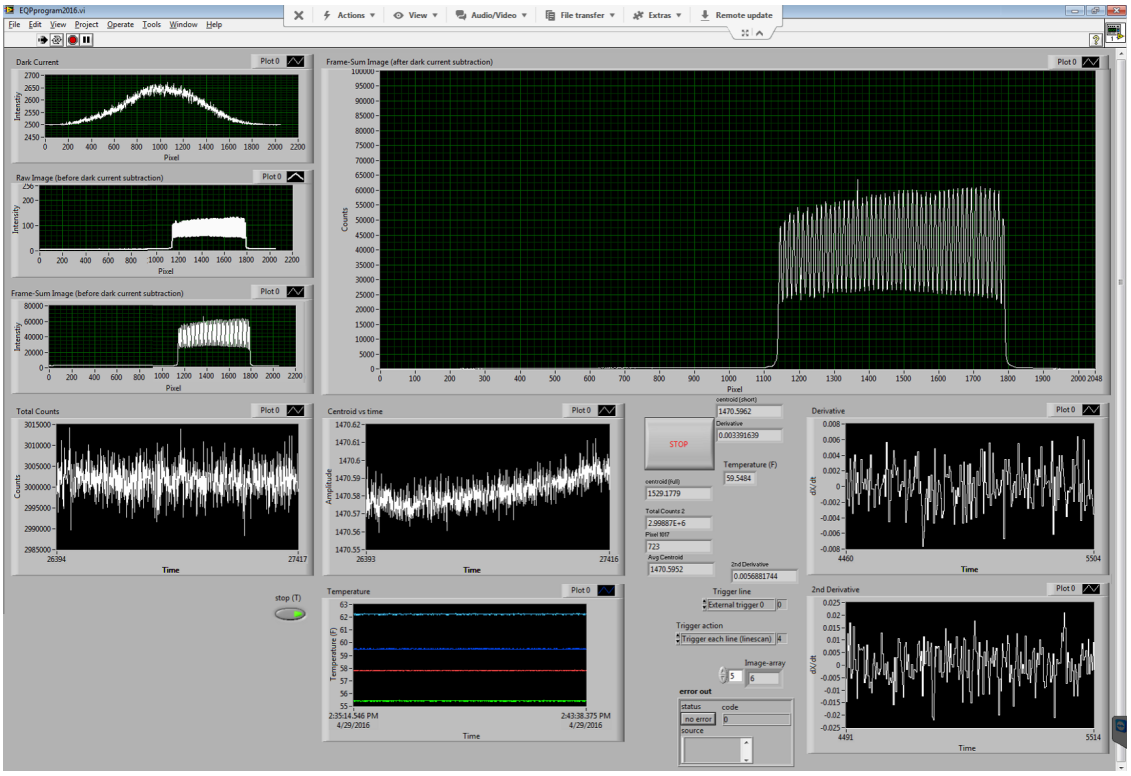

Figure C.1: A screenshot of the LabVIEW program front panel during testing. The large plot in the top right portion of the figure shows the image used to determine the balance position.

Simultaneously, voltages are read out from National Instrument USB-6008 DAQs connected to thermistors monitoring temperature around the experiment and the ion pump controller which is used to determine the vacuum pressure inside the chamber. These voltages are written to an output file. Separate subVIs are used to convert the thermistor voltages to temperature readings which are then plotted on the front panel.

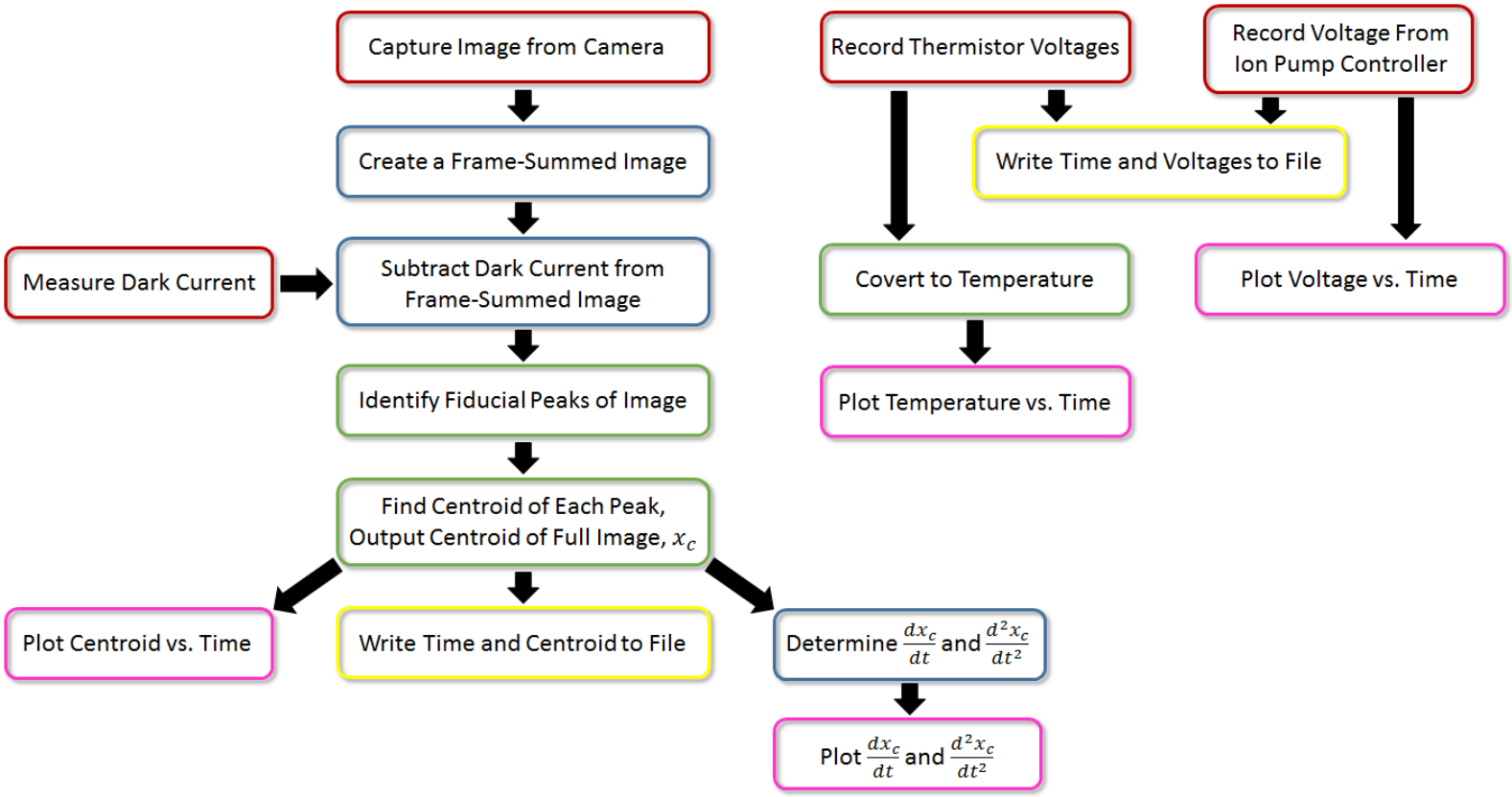

Figure C.2: Flowchart of the data collection, storage, and display through the LabVIEW interface. Blocks outlined in red represent processes that involve making a measurement, block outlined in blue involve some type of simple computation, blocks outlined in green correspond to more complex processes completed by a subVI, blocks outlined in yellow denote the action of writing data to a output file, while the blocks outlined in fuchsia represent plots of a quantity vs. time. This process is continuously triggered by a function generator with the exception that the dark current measurement is made once, before starting data collection.